Chapter 18
Radiation Effects in Metals: Hardening, Embrittlement, and Fracture

18.1 STRUCTURAL METALS FOR FAST REACTORS

The neutron economy of a fast reactor is not so significantly affected by neutron capture in the structural materials in the core as is that of a thermal reactor. First, most neutron-capture cross sections increase with decreasing neutron energy, and the neutron population of the liquid-metal fast breeder reactor (LMFBR) contains a far lower percentage of thermal neutrons than does that of a light-water reactor (LWR). Second, the ratio of the mass of structural metal to the mass of fissile materials is much smaller in a fast reactor than in a thermal reactor. Consequently, metals that in a thermal reactor would severely impair neutron economy are acceptable in a fast reactor, and the selection of core structural materials for the LMFBR can be based primarily on cost and mechanical and chemical properties. The downgrading of neutron-absorption characteristics from the selection criteria for core structural metals means that the costly zirconium alloys used in thermal reactors need not be employed in fast reactors. However, parasitic neutron absorption by nonfuel components is important enough to cause LMFBR core designers to be quite sparing in using certain structural metals. The irradiation properties of high-nickel alloys, for example, are generally superior to those of conventional stainless steel, but nickel has a seriously large cross section for absorption of fast neutrons.

The most important metallic component of a reactor core is the fuel cladding; this member provides structural integrity to the fuel element, prevents fission products from escaping to the primary coolant system, and separates the sodium coolant from the ceramic oxide fuel (with which it reacts). The cladding must be thin-walled tubing that can remain intact in a fast reactor environment for periods of up to 3 years at temperatures to 800°C, diametral strains of 3%, and fluences up to 3×10^{23} neutrons cm^{-2} sec^{-1}. The cladding alloy selected for the LMFBR is the austenitic stainless steel described as type 316. This material has an fcc crystal structure. (Austenite is the fcc modification of

iron. It is the stable form of pure iron between 910 and 1400°C. The addition of nickel stabilizes this structure above room temperature.) It has good high-temperature creep strength and resists corrosion by liquid-sodium and hypostoichiometric mixed-oxide fuels. Moreover, it is cheaper than more exotic metals, available in sufficient quantities for the fast reactor program, and is easy to fabricate. The compositions of two austenitic stainless steels are given in Table 18.1.

The austenitic stainless steels, however, are highly susceptible to swelling owing to void formation and to high-temperature embrittlement by the helium produced in neutron reactions with constituents of the alloy. Commercial nickel alloys (e.g., Inconel and Incaloy) are backup materials for core structural components in the liquid-metal fast breeder reactor. These alloys appear to be less prone to void swelling, but their neutron-absorption cross section is higher than that of steel. Vanadium-based and refractory-metal alloys are long-range candidates for LMFBR fuel-element cladding. These two classes of metals both possess bcc lattice structures and are more resistant to helium embrittlement than are the austenitic stainless steels or nickel alloys. In addition, the refractory metals (e.g., molybdenum) do not form voids under large fast-neutron fluences at the cladding service temperatures of the LMFBR. However, both vanadium alloys and the refractory metals are much more costly than stainless steel, and their use as cladding would significantly increase the capital cost of a fast reactor.

Although the generally favorable high-temperature properties of the austenitic stainless steel are utilized in the fast reactor core compounds (e.g., in cladding and assembly wrappers), the lower flux, lower temperature environment outside the core permits less expensive steels to be used for the reactor pressure vessel. In both LMFBR and LWR systems, ordinary ferritic or alloy steel is used for this component. (Ferrite is a bcc modification of iron.) Typical alloy-steel compositions are shown in Table 18.2. This material does not possess, nor does it need to possess, the high-temperature strength and corrosion resistance of stain-

Table 18.1 Composition of Austenitic Stainless Steels

Element	Type 304, wt. %	Type 316, wt. %	
Fe	70	65	Major
Cr	19	17	constituents
Ni	9	13	
C	0.06	0.06	
Mn	0.8	1.8	
P	0.02	0.02	Interstitial
S	0.02	0.02	impurities
Si	0.5	0.3	
B	0.0005	0.0005	
N		0.03	
Mo	0.2	2.2	Substitutional
Co		0.3	impurities

Table 18.2 Composition of Pressure-Vessel Steels

Element	A302-B, wt. %	A212-B, wt. %	
Fe	97	98	
C	0.2	0.3	
Mn	1.3	0.8	Interstitial
P	0.01	0.01	impurities
Si	0.3	0.3	
S	0.02	0.03	
Cr	0.2	0.2	Substitutional
Ni	0.2	0.2	impurities
Mo	0.5	0.02	

less steel, but it is much cheaper. In common with most bcc metals, ferritic steel exhibits one potentially serious radiation effect. Below a certain temperature known as the ductile—brittle transition temperature (DBTT), or nil-ductility temperature (NDT), the metal is susceptible to brittle fracture. As long as the lowest operating temperature is greater than the nil-ductility temperature, the metal is ductile. However, the nil-ductility temperature increases dramatically with neutron exposure, and, toward the end of a 30-year lifetime, a pressure vessel can be subject to brittle failure. Such catastrophic failures have occasionally occurred in bridges, large storage tanks, and ships. Usually the entire structure breaks apart when brittle fracture occurs.

Four broad categories of mechanical behavior are pertinent to reactor performance:

1. Radiation hardening.
2. Embrittlement and fracture.
3. Swelling.
4. Irradiation creep.

This chapter deals with the first two of these features. Swelling and irradiation creep are considered in the following chapter.

Radiation hardening usually means the increase in the yield stress and the ultimate tensile stress as a function of fast-neutron fluence and temperature. The yield strength and ultimate strength are measured in tests in which

deformation occurs at high stresses and rather quickly. However, the strength of fuel-element cladding is most accurately represented by the resistance of the metal to slow deformation by creep, since the internal loading on the cladding never reaches the yield stress. The creep strength of a metal is usually determined by the time required for failure under a fixed applied stress (i.e., a stress rupture test).

Embrittlement of a metal is measured by the amount of plastic or creep deformation that occurs before fracture. Fast-neutron irradiation invariably renders a metal less ductile than the unirradiated material. Fracture can be of the brittle type in which a small crack swiftly propagates across an entire piece, or it can occur only after long times at stress and after appreciable deformation. Failure by stress rupture takes place by linkup of small intergranular cracks or cavities that have developed throughout the interior of the metal.

18.2 EVOLUTION OF THE MICROSTRUCTURE OF STEEL DURING NEUTRON IRRADIATION

The radiation-produced entities responsible for changes in the mechanical properties of neutron-bombarded metals can be identified, counted, and sized with the aid of the electron microscope. When an electron beam of several-hundred kiloelectron volts energy passes through a thin metal specimen, some of the electrons are transmitted through the foil, and others are diffracted in much the same way that X rays are diffracted by parallel atomic planes near the surface of a crystal. The foil is sufficiently thin (1000 to 5000 Å) and the incident electron beam sufficiently well collimated (spot size of several micrometers) that only a part of a single grain is probed. Within this single-crystal region of the material, some atomic planes are properly oriented to diffract the incident electron beam. The angle of the diffracted beam relative to the incident electron beam is determined by the Bragg condition based on the de Broglie wavelength of the incident electrons and the spacing of the atomic planes of the solid. The intensity of the transmitted beam is reduced to the extent that the intervening solid satisfies the Bragg condition and produces strong diffraction. Figure 18.1 is a sketch of the setup for bright-field transmission-electron microscopy. The transmitted electrons are brought into focus at an aperture by means of an electrostatic lens. The position of the aperture is adjusted so that only transmitted electrons are permitted to pass; the diffracted beams are stopped. Any defect that locally destroys the perfection of the crystal lattice also alters the diffraction conditions at this point. When the orientation and/or spacing of the atomic planes around the defect more closely satisfy the Bragg condition than do the planes in the perfect crystal, the diffraction phenomenon is stronger for the planes around the defect than for those in the perfect crystal. With reference to Fig. 18.1, if $I'_D > I_D$, then the transmitted beam from the vicinity of the defect is weaker than that from the perfect crystal. The defect appears on the photographic plate behind the aperture as a dark image on a bright background. The contrast of the image is proportional to $I_T - I'_T$. Such photographs repre-
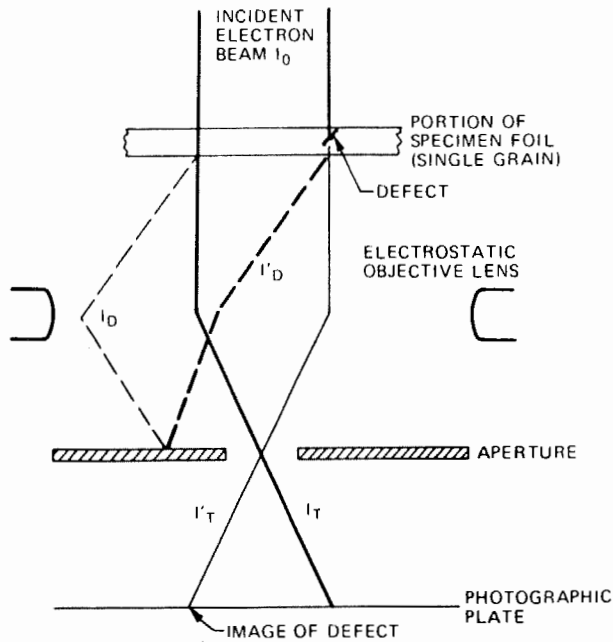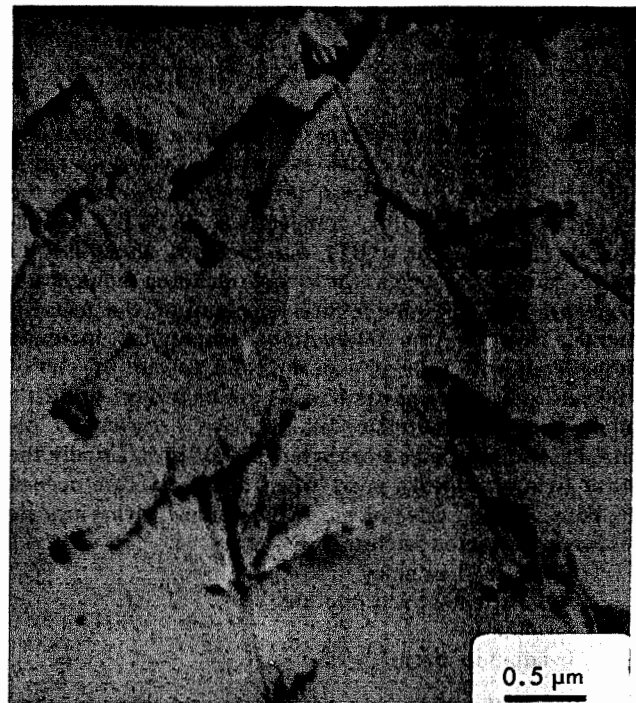
Fig. 18.1 Illustration of image formation in bright-field electron microscopy. The values I_T and I_D denote the intensities of the transmitted and diffracted beams for incident electrons passing through a region of perfect crystal. The primed quantities denote the analogous intensities from the region of the defect.

sent the projected image of the three-dimensional crystal defect. Atomic planes that are out of register (as those near a grain boundary or a stacking fault) or zones of the crystal that are distorted by a strain field (as around dislocations) produce interference patterns and can therefore be imaged.

Gas-filled bubbles at equilibrium (i.e., gas pressure balanced by surface tension) do not strain the surrounding solid, which therefore behaves as undistorted crystal. Even when the cavity contains no gas (a void), the strain field in the vicinity of the defect is negligible. Bubbles and voids are detectable by virtue of the smaller absorption of the electron beam passing through the cavity compared with the electrons that pass through a section of the foil consisting entirely of solid.

Figure 18.2 shows the microstructure of a typical unirradiated austenitic stainless steel used for fast reactor fuel-element cladding. Figure 18.2(a) shows an ordinary photomicrograph of a polished specimen. The grains are clearly visible and average 25 μm in size. The transmission-electron micrograph of Fig. 18.2(b) contains only segments of the dislocation network of the as-fabricated metal.

18.2.1 Black-Dot Structure

Figure 18.3 shows the microstructure of a specimen irradiated at $\sim100^\circ$C by a fast-neutron fluence of $\sim10^{21}$ neutrons/cm^2. The defects produced at these conditions appear as black dots in the electron micrograph. The defects are too small to permit their structure to be revealed by the electron microscope, but they are believed

(a)

(b)

Fig. 18.2 Microstructure of unirradiated type 304 stainless steel (a) Photomicrograph showing grain structure. (b) Electron micrograph showing dislocation structure. (From E. E. Bloom, An Investigation of Fast Neutron Radiation Damage in An Austenitic Stainless Steel, USAEC Report ORNL-4580, Oak Ridge National Laboratory, 1970.)
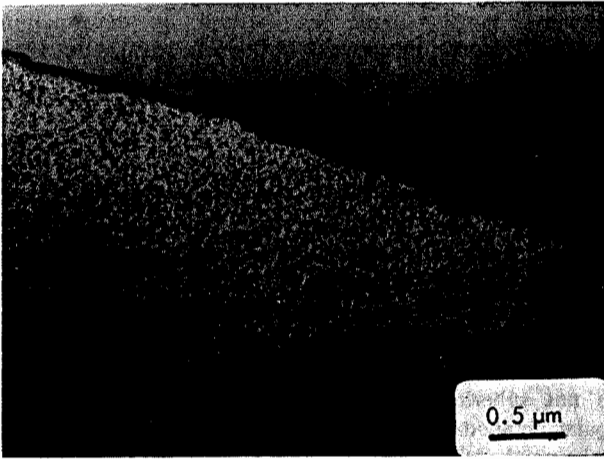
Fig. 18.3 Type 304 stainless steel irradiated at 93°C. [From E. E. Bloom, W. R. Martin, J. O. Stiegler, and J. R. Weir, *J. Nucl. Mater.*, 22: 68 (1967).]

to represent the depleted zones or vacancy clusters predicted by radiation-damage theory (Figs. 17.25 and 17.30). As long as the irradiation temperature is below ~350°C, increasing fluence simply increases the density of the black-dot damage.

When irradiation is carried out at temperatures greater than ~350°C, the nature of the microstructure is entirely different from the black-dot pattern characteristic of low-temperature irradiation. In stainless steel irradiated above 350°C, the point defects created by the collision cascades are sufficiently mobile to move about in the solid and agglomerate into larger defect clusters. The damage structure consists of dislocation loops and voids.

18.2.2 Loops

The defect agglomeration commonly called a loop is formed by condensation of radiation-produced vacancies or interstitials into roughly circular disks followed by collapse of the atomic planes adjacent to the platelet. Vacancy-loop formation is shown in Figs. 18.4(a) and 18.4(b), and the corresponding process for interstitials is depicted in Figs. 18.4(c) and 18.4(d). The end result of the condensation/collapse process is a region delineated by a circular edge dislocation. In the fcc structure, loops invariably form on {111} planes. When a (111) plane is added to or removed from the lattice by agglomeration of a disk of interstitials or vacancies, the stacking sequence of the perfect close-packed structure (Sec. 3.6) is disturbed. The circular edge dislocation thus encloses a *stacking fault*.

The dislocation loops shown in Figs. 18.4(b) and 18.4(d) are called *Frank sessile* dislocations or simply Frank loops. The term sessile means immobile. Because the dislocation encloses a stacking fault, Frank loops are also called *faulted loops*. The Burgers vector of a Frank dislocation is perpendicular to the plane of the loop, and its magnitude is equal to the separation of the (111) planes. This Burgers vector is denoted symbolically by

$$b = \pm \frac{a_o}{3} [111] \qquad (18.1)$$

The direction is indicated by the Miller indices in the brackets. The sign depends on whether the loop was formed from vacancies or interstitials. The length of the Burgers vector is given by the square root of the sum of the squares of the Miller indices times the coefficient $a_o/3$, or $(a_o/3)3^{1/2} = a_o/3^{1/2}$.

Edge dislocations can slip only in the direction of their Burgers vector. The cylinder normal to the loop on which the dislocation can move is not a $\langle 110 \rangle$ glide direction for fcc slip [Fig. 8.2(a)]. Therefore, the Frank dislocation loop cannot move in the direction of its Burgers vector and hence is immobile, or sessile. The loop can change diameter by absorbing or emitting point defects (i.e., by climb). Net addition of the same type of point defect causes the loop to grow, whereas absorption of the opposite type of point defect causes shrinkage. The stacking fault can be eliminated by moving the crystal above the loop relative to the solid below it. This shearing action is accomplished by passage of another type of dislocation, called a Shockley dislocation, across the faulted area. The Shockley dislocation and the Frank dislocation react to form a dislocation loop at the same position as the original Frank loop but with the interior of the loop now in perfect stacking registry with the neighboring (111) planes. The loop unfaulting process occurs spontaneously in stainless steel at about 600°C. The Burgers vector of the unfaulted loop is

$$b = \pm \frac{a_o}{2} [110] \qquad (18.2)$$

This Burgers vector is properly oriented for glide in the fcc lattice [Fig. 8.2(a)], and the loop is therefore mobile. As it moves by slip, it sweeps out a cylindrical surface tilted at an
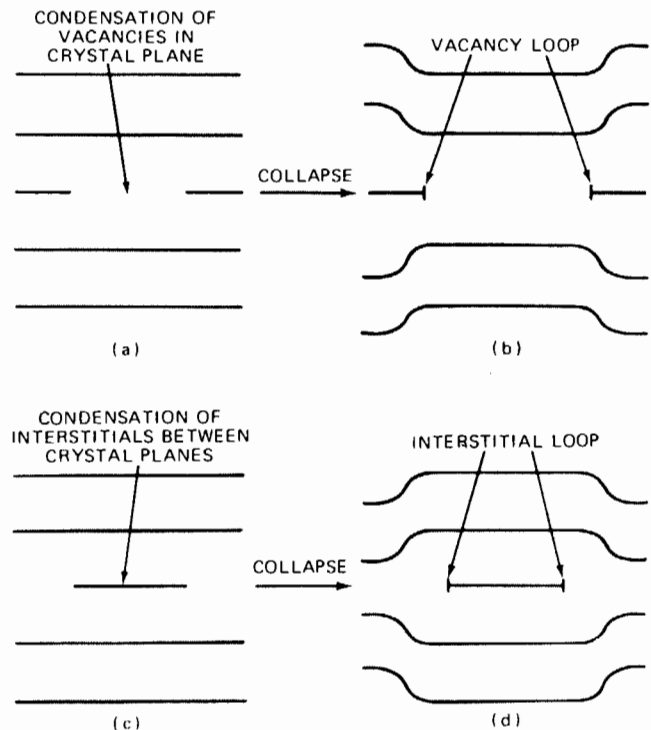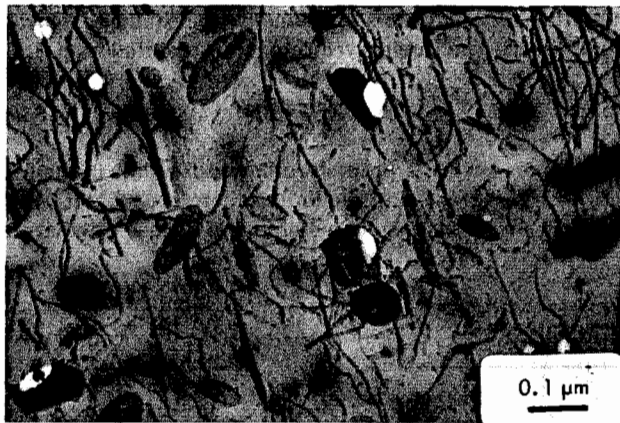

Fig. 18.4 Formation of vacancy loops and interstitial loops.

angle to the (111) plane. Because of the shape of slip pattern, the unfaulted loop is often called a *prismatic* loop. It is distinguished from the shear loop shown in Fig. 8.6 by the direction of the Burgers vector with respect to the plane of the loop. The Burgers vector of a shear loop lies in the plane of the loop, whereas the Burgers vector of a prismatic loop lies outside the plane of the loop. The dislocation of the unfaulted loop given by Eq. 18.2 is perfect in the sense that movement along the slip plane leaves the atoms in positions equivalent to those previously occupied. The dislocation characterizing the Frank sessile loop (Eq. 18.1) does not satisfy this criterion, and the Frank loop is said to be imperfect.

Faulted and unfaulted dislocation loops are shown in Figs. 18.5(a) and 18.5(b), respectively. Because of the stacking fault they enclose, the faulted loops in Fig. 18.5(a) appear in the electron microscope as opaque circles. Removal of the faulted region renders the interior of the loop identical to the rest of the solid, and only the outline of the loop remains [Fig. 18.5(b)]. Since the unfaulted dislocation loops are mobile, they easily lose their distinctive circular shape by gliding under an applied stress and becoming tangled with the natural or deformation-produced dislocation network of the solid. Loops disappear from the irradiated solid at about 600 to 650°C.

18.2.3 Voids

Under some conditions the embryo collection of vacancies of Fig. 18.4(a) can begin to grow in a three-dimensional manner rather than collapse into a dislocation loop. This route leads to the formation of voids in metals and consequent swelling of the structure (Chap. 19). Voids produced in stainless steel by high-fluence fast-neutron bombardment at 525°C are shown in Fig. 18.6. The voids are not spherical. Rather, they assume the shape of a regular octahedron with {111} planes as surfaces. The ends of the octahedron, however, are truncated by {100} planes. Voids are annealed out of the microstructure at about 750°C.

18.2.4 Carbide Precipitates

In pure metals, only voids and dislocation loops are produced by intermediate-temperature irradiation. In a material as complex as stainless steel, however, neutron irradiation also causes different solid phases to precipitate. Carbon is added to steel in the molten state, where the solubility of carbon is high. Carbon solubility, whether in the solid or in the liquid forms of steel, decreases rapidly as the temperature is reduced. However, when the steel is rapidly quenched from the melt, the kinetics of carbon precipitation are too slow to keep up with the rapid decrease in the mobility of the atomic species in the solid. Consequently, the 0.06 wt.% carbon in steel (Table 18.1) is maintained in atomic form as a supersaturated solution. When the steel is heated to temperatures at which supersaturation persists but atomic mobility is appreciable, the carbon can be expelled from solution and form a second phase in the metal. When steel is aged (i.e., heated for long periods of time at elevated temperatures), dissolved carbon reacts with the matrix elements iron and chromium to form a compound $M_{23}C_6$ (M = Cr and Fe) which is insoluble in the austenite or gamma phase. These carbides are formed by the reaction

$$23M(\gamma) + 6C(\gamma) = M_{23}C_6 \text{ (mixed carbide)}$$
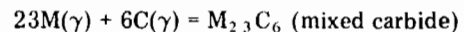
where γ denotes the austenitic phase. The carbide formed is a mixture of $Fe_{23}C_6$ and $Cr_{23}C_6$. Since chromium is a strong carbide-former, the mixed carbide consists primarily of $Cr_{23}C_6$. The nickel constituent of stainless steel does not form stable carbides.

Neutron irradiation accelerates the diffusional processes that control the mobilities of the atomic species in the lattice and hence the kinetics of the preceding precipitation reaction. Carbide precipitation occurs at much lower temperatures and shorter times than those required for aging in the absence of irradiation. Radiation accelerates the rates of precipitation reactions when such processes are thermodynamically favorable. If the irradiation temperature is above that at which the solubility limit of carbon is equal to the carbon content of the steel, irradiation cannot cause precipitation. For type 316 stainless steel containing 0.06%
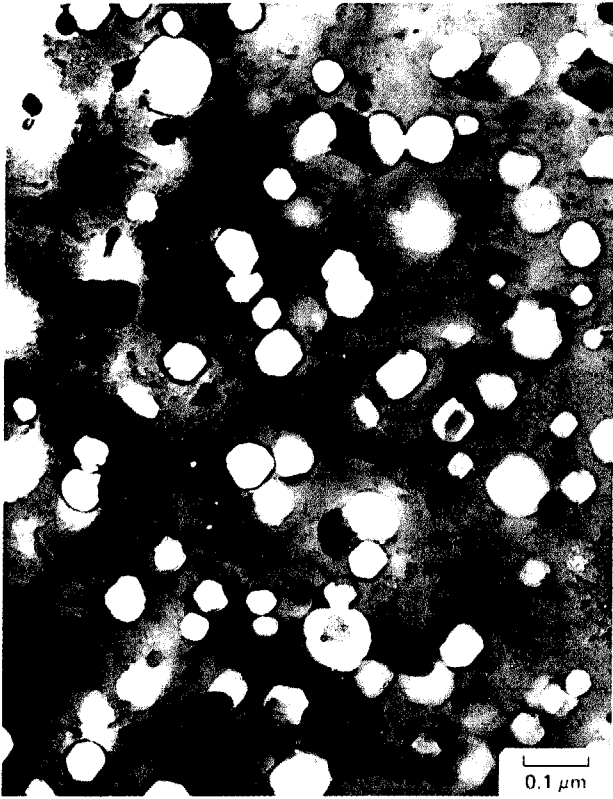

0.1 µm

0.1 µm

(b)

Fig. 18.5 Dislocation loops in type 304 stainless steel. (a) Faulted. (b) Unfaulted. (From E. E. Bloom and J. O. Stiegler, in ASTM Special Technical Publication 484, p. 451, American Society for Testing and Materials, Philadelphia, 1970.)

Fig. 18.6 Type 316 stainless-steel specimen irradiated at 525°C to 7.1 × 10^{22} neutrons/cm^2 (E > 0.1 MeV). Mean void diameter, 640 Å; void number density, 4.4 × 10^{14} voids/cm^3. [From W. K. Appleby et al., in *Radiation-Induced Voids in Metals*, Albany, N. Y., James W. Corbett and Louis C. Ianniello (Eds.), USAEC Symposium Series, CONF-710601, p. 166, 1971.]

carbon, for example, carbide precipitation is thermodynamically unfavorable at temperatures greater than ~900°C. At temperatures lower than ~400°C, diffusional processes are too slow (even when enhanced by irradiation) to cause observable precipitation in reasonable irradiation times. Between 400 and 900°C, however, exposure of austenitic stainless steel to fast-neutron fluences between 10^{21} and 10^{22} neutrons/cm^2 produces carbide precipitation. Figure 18.7 shows an electron micrograph of carbide precipitation in type 316 stainless steel. Carbide particles are found both within the grains of the γ phase (austenite) and on the grain boundaries. The presence of precipitates on the grain boundaries affects the creep strength of the alloy.

18.2.5 Helium Bubbles

At temperatures above ~800°C, dislocation loops and voids are not found in irradiated steel. In addition to grain boundaries, dislocations (augmented by the unfaulted loops that have joined the original dislocation network), and carbide precipitates, the microstructure contains small helium-filled bubbles. Helium is generated by (n,α) reactions with the boron impurity in the steel and

with the major constituents, principally nickel. At temperatures below ~650°C, the helium atoms produced by stopping the alpha particles in the material are not mobile enough to migrate and nucleate bubbles. Consequently, helium remains in solution and is invisible to the electron microscope. At high temperatures helium bubbles form in the metal in the same way that fission-gas bubbles form in ceramic oxide fuel material (Chap. 13). The helium bubbles in the metal are nearly spherical, which suggests that the internal gas pressure is very nearly balanced by surface-tension forces. Figure 18.8 shows the helium bubbles in stainless steel at 800°C. In this instance, the helium was injected into the specimen by a cyclotron. The bubbles on the grain boundaries are larger than those in the matrix. The intergranular helium plays an important role in the high-temperature embrittlement of stainless steel. Short of melting, helium bubbles cannot be removed from the metal by annealing.

18.3 MECHANICAL-PROPERTIES TESTS

Much of the mechanical testing designed to elucidate the effects of neutron irradiation on structural metals is performed after irradiation with conventional metallurgical testing machines. Usually the specimens are irradiated in a neutron flux of known energy spectrum for a fixed period of time and then removed for testing. The effects of large neutron fluences (i.e., very long irradiations) can be

Fig. 18.7 Nearly continuous $M_{23}C_6$ precipitation along grain boundary of solution-treated type 316 irradiated at 850°C to 5.1 × 10^{22} neutrons/cm^2. [From H. R. Brager and J. L. Straalsund, *J. Nucl. Mater.*, 46: 134 (1973).]
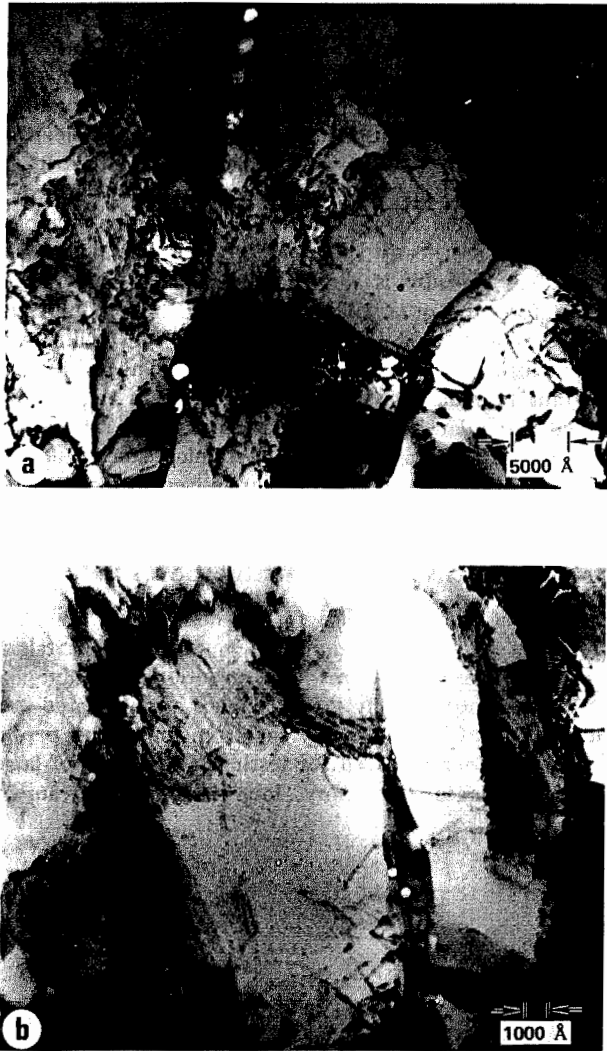
Fig. 18.8 Transmission electron micrographs of stainless steel injected with 5×10^{-5} atom fraction helium, tested at 800°C. Large helium bubbles are seen in (a) the grain boundary and (b) in the grain boundary, with smaller bubbles in the matrix. (From D. Kramer et al., in ASTM Special Technical Publication 484, p. 509, American Society for Testing and Materials, Philadelphia, 1970.)

determined by the simple expedient of removing core components of a reactor and fabricating test samples from them. Aside from the problems associated with handling and shielding radioactive samples, post-irradiation testing is a routine operation, and a large amount of mechanical-properties data can be accumulated quickly and inexpensively.

The mechanical properties of irradiated structural steels depend on the irradiation temperature. When testing is done after removal from the reactor, the testing temperature is unavoidably introduced as an additional parameter. This additional degree of flexibility is often valuable; tensile tests over a range of test temperatures on specimens

irradiated at a fixed temperature provide information on the thermal stability of defects that are responsible for the change in strength brought about by irradiation. For some properties, however, out-of-pile testing, even at a test temperature equal to the irradiation temperature, does not adequately represent the behavior of the metal in the reactor environment. This complication can be eliminated by performing mechanical tests during irradiation; such experiments, however, are difficult and costly. In-pile testing is usually restricted to measurement of mechanical properties that depend critically on the neutron flux as well as on the neutron fluence (e.g., irradiation creep).

This section reviews some of the conventional mechanical-property tests that are applied to irradiated structural steels.

18.3.1 Tensile Test

The tensile test provides a means of uniaxially loading a rod or bar-shaped specimen and of measuring the elongation for various applied loads (Fig. 18.9). When a specimen of initial length l_0 and cross sectional area A_0 is subjected to an applied load in tension P, the length increases to l, and the cross-sectional area is reduced to A. The *engineering stress* in the test is defined as the ratio of the load to the initial cross sectional area, or P/A_0. The *true tensile stress*, however, is based on the actual specimen area, or

$$\sigma = \frac{P}{A} \qquad (18.3)$$

The *engineering strain* is the elongation divided by the initial specimen length, or $(l - l_0)/l_0$. The *true strain*, on the other hand, is the integral of the increments of strain over the specimen length:

$$\epsilon = \int_{l_0}^{l} \frac{dl}{l} = \ln\left(\frac{l}{l_0}\right) \qquad (18.4)$$

The true strain is always somewhat larger than the engineering strain. The true strain defined by Eq. 18.4 is
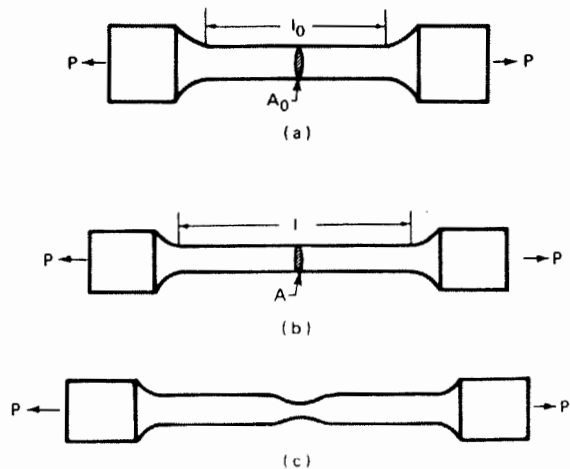

Fig. 18.9 The tensile test. (a) Test specimen. (b) Uniform elongation. (c) Necking.

not equivalent to the strain components commonly employed in elasticity theory (i.e., Eq. A.10 of the Appendix). The relation between the infinitesimal strain components and displacement is determined by Taylor series expansions, which neglect products of strain components. The strain of Eq. 18.4 is applicable to finite deformations encountered in tensile tests far into the plastic region. It is also called the logarithmic strain.

In the elastic stress region, the true stress—strain curve obeys Hooke's law, which for the uniaxial tensile test is $\sigma = E\epsilon$. However, tensile tests are generally intended to investigate the behavior of the metal at much larger stresses than those for which Hooke's law is followed. The large, irreversible plastic strains in most tensile tests take place at essentially constant volume because deformation occurs primarily by shear. With the specimen volume constant, area reduction is related to elongation by

$$Al = A_0 l_0$$

or

$$\frac{dl}{l} = -\frac{dA}{A} \qquad (18.5)$$

Thus, the true strain can also be expressed by

$$\epsilon = \int_{A_0}^{A}\left(-\frac{dA}{A}\right) = \ln\left(\frac{A_0}{A}\right) \qquad (18.6)$$

The preceding equations apply without qualification to the portion of the deformation in which the cross-sectional area of the specimen is reduced by the same amount over the entire length of the specimen. This mode of deformation is called *uniform elongation* [Fig. 18.9(b)]. At a certain load the cross-sectional area of a localized section of the specimen begins to decrease more rapidly than the remainder of the bar [Fig. 18.9(c)]. This phenomenon is called *necking*, and the stress or strain at which it begins is the point of *plastic instability*.

The stress—strain curves for a typical (unirradiated) low-alloy steel are shown in Fig. 18.10. The general shapes of these curves are characteristic of most metals that crystallize in the bcc lattice structure. The solid line depicts the engineering stress—strain curve, which is a plot of P/A_0 vs. $(l - l_0)/l_0$. The material deforms elastically according to Hooke's law up to the point U, where the specimen appears to give way or to *yield*. The load then drops with increasing elongation to the point L. The points U and L are called the upper and lower yield points, respectively. The reported yield strength of a material is usually the stress at the lower yield point. For a short strain interval following point L, plastic deformation proceeds with no increase in load. This interval is called the Lüders strain. The stress level characterizing the Lüders strain region is essentially the same as the lower yield point, although it is sometimes called the *flow stress* of the material.

Following the Lüders strain is a region where the stress required to produce further strain increases. This portion of the stress—strain curve is called the *strain-hardening* or *work-hardening* region because the material becomes
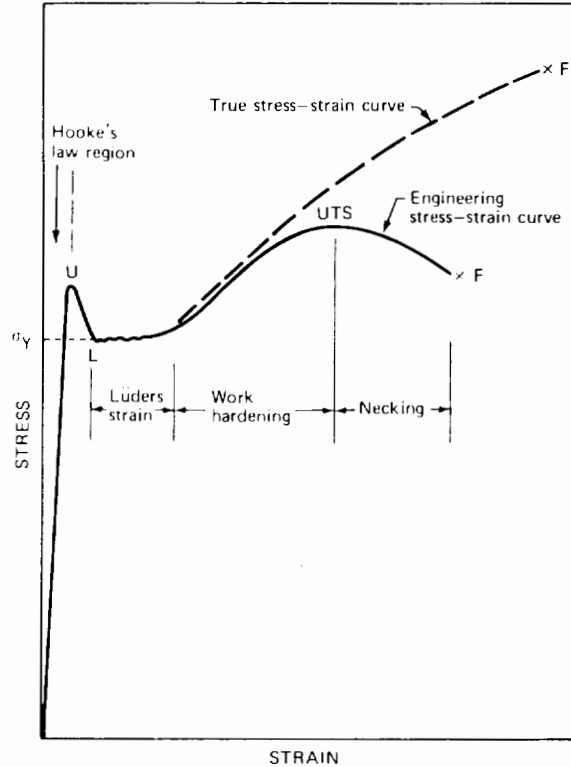

Fig. 18.10 Stress—strain curve for ferritic steel.

stronger as a result of the deformation process. Plastic instability terminates the work-hardening portion of the stress—strain curve at the point labeled UTS, which stands for *ultimate tensile stress*. This point represents the maximum load-bearing capacity of the specimen. At all times during deformation, the load is equal to the product of the actual cross-sectional area and the true stress, or $P = \sigma A$. At the UTS, $dP = 0$, or

$$\frac{d\sigma}{\sigma} = -\frac{dA}{A}$$

According to Eq. 18.6, $-dA/A = d\epsilon$; so the onset of necking, which occurs at the UTS, is located on the true stress—strain curve at the point at which

$$\frac{d\sigma}{d\epsilon} = \sigma \qquad (18.7)$$

Up to plastic instability, the true stress—strain curve (the dashed curve in Fig. 18.10) can be constructed using Eqs. 18.3 and 18.4. During necking, Eq. 18.4 does not apply if the gauge length l is interpreted as the total specimen length. However, nowhere has it been specified that l must be the entire specimen length; it could very well have been chosen as a very short segment right in the necking region. Over this small segment, elongation is uniform. It is experimentally difficult to measure length changes in a very tiny gauge length. However, Eq. 18.6 applies to the necked region provided that the area A is the cross-sectional area at the most severely necked part of the specimen. Therefore, application of Eqs. 18.3 and 18.6

with the necked area taken for A permits the true stress—strain curve to be extended from the UTS to fracture (point F). The true strain and stress at fracture are always larger than those based on the engineering stress—strain curve. At small strains, however, the difference between the two stress—strain curves is negligible. The yield stress, for example, can be represented by either curve with no appreciable error.

Figure 18.11 shows the tensile behavior of a typical austenitic steel. The primary difference between the stress—strain curves in Figs. 18.10 and 18.11 is the absence of a well-defined yield point in Fig. 18.11. For most metals with an fcc structure, the stress—strain curve continuously
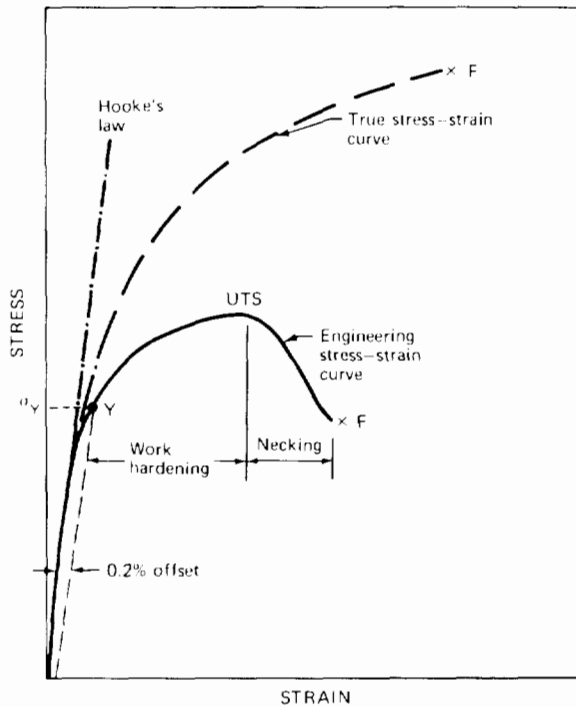

Fig. 18.11   Stress—strain curve for austenitic steel.

deviates from Hooke's law as the stress is increased, and it is impossible to assign a definite stress at which plastic deformation begins. That is, the metal does not yield in an unequivocal manner. Hence, yielding (or the onset of plastic flow) in such metals is arbitrarily considered to occur when the permanent strain in the tensile test is 0.2%. This stress, denoted by σ_Y in Fig. 18.11, is called the *0.2% offset yield strength* of the metal.

Ductility is measured either by the amount of strain between the true fracture stress and the yield stress $(\epsilon_F - \epsilon_Y)$ or more commonly by the total uniform elongation up to necking. *Embrittlement* means a reduction in either of these two measures of ductility. A brittle material fails when yield occurs or, in the case of a material having no sharp yield point, when failure occurs before 0.2% offset strain.

The rate at which deformation is imposed in the tensile test, or the strain rate, affects the stress—strain curves of

Figs. 18.10 and 18.11. The yield stress is reduced at low strain rates because the slow motion of dislocations at low stress levels becomes sufficient to become manifest as plastic deformation. In unirradiated steels, ductility is not significantly affected by strain rate.

Strain rates of 0.01 min^{-1} are characteristic of conventional tensile tests. This figure is also approximately equal to the strain rates induced in cladding by typical reactor power transients (shutdown, startup, and power cycling). When the strain rate in the test is reduced to 10^{-4} min^{-1} and the temperature is high, the test is called a creep-rupture test. This strain rate is typical of that imposed on cladding by fuel swelling in the reactor.

18.3.2   Tube-Burst Tests—Biaxial Stress State

The tensile test described above is an experimentally convenient way of measuring the mechanical properties of a metal. In addition, theoretical interpretation of the stress—strain curves is simplified by the fact that there is only one nonzero component of the stress tensor, namely, the normal stress in the direction of the applied load. However, the stress state of fuel-element cladding loaded internally by fission-gas pressure and fuel swelling more closely resembles that in a long thin-walled cylindrical tube closed at both ends and pressurized by a gas. Since cladding fails by creep rupture after long periods of being subjected to stresses well below the yield stress, considerable creep-rupture testing of unirradiated and irradiated steel tubing has been performed by pressurizing closed tubing with an inert gas. These tests are called tube-burst tests.

According to elasticity theory, the normal stresses in closed tubes loaded by an internal gas pressure p are given by (see problem 18.6)

$$\sigma_\theta = \frac{pD}{2t} \tag{18.8a}$$

$$\sigma_z = \frac{pD}{4t} \tag{18.8b}$$

$$\sigma_r \simeq 0 \tag{18.8c}$$

where D is the tube diameter and t is the wall thickness $(t \ll D)$. The infinitesimal radial and tangential strains appropriate to conventional elasticity theory are $(t - t_0)/t_0$ and $(D - D_0)/D_0$, respectively. The logarithmic strains should be used when appreciable deformation occurs. The true (logarithmic) strains are

$$\epsilon_r = \ln\left(\frac{t}{t_0}\right) \tag{18.9a}$$

$$\epsilon_\theta = \ln\left(\frac{D}{D_0}\right) \tag{18.9b}$$

$$\epsilon_z = 0 \tag{18.9c}$$

where D_0 and t_0 are the initial tube diameter and wall thickness, respectively. By varying the gas pressure, p, plastic deformation of the tube can be induced. Because the tube wall is subject to two stress components of com-

parable magnitude, the stress state is *biaxial.* To interpret the results of tube-burst tests, one needs to know the correspondence between the states of plastic stress and plastic strain for the uniaxial and biaxial situations. For example, if yield occurs in the tensile test at a true stress of σ_Y, at what gas pressure should the tube yield?

More generally, the criterion for yielding in multiaxial stress states is needed. In the tensile and tube-burst tests, no shear stresses are involved. In these cases the coordinates (x,y,z) and (r,θ,z) are called the principal axes, and the normal stresses acting on planes perpendicular to these axes are the principal stresses. In situations where the shear strains are not zero, it is always possible to rotate the conventional coordinate system (cartesian, cylindrical, and spherical) into another set of coordinates, called 1, 2, and 3, for which the shear stresses vanish. The normal stresses acting along these axes, σ_1, σ_2, and σ_3, are the principal stresses of the system. Although no coordinate rotation is necessary in the tensile and tube-burst tests, the multiaxial yield criterion will be developed in terms of the principal stresses, σ_1, σ_2, and σ_3, and then specialized to the two cases of interest.

In the absence of a shear stress, the elastic strain energy density of a deformed solid is given by Eq. A.26 of the Appendix as

$$E_{el} = \frac{1}{2E}(\sigma_1^2 + \sigma_2^2 + \sigma_3^2) - \frac{\nu}{E}(\sigma_1\sigma_2 + \sigma_1\sigma_3 + \sigma_2\sigma_3) \quad (18.10)$$

A general yielding criterion could be based on the hypothesis that yielding occurs when the strain energy, E_{el}, reaches a critical value. However, this criterion is not enough, because it is well known that large amounts of strain energy can be stored by the action of purely hydrostatic stresses without causing the material to deform permanently. Von Mises proposed that the appropriate strain energy is the difference between the total energy density of Eq. 18.10 and the energy density that the solid would acquire had it been subject to the mean of the three principal stresses. The mean normal stress is

$$\sigma_h = \frac{1}{3}(\sigma_1 + \sigma_2 + \sigma_3) \quad (18.11)$$

and the elastic-energy density arising from the hydrostatic stress is obtained by substituting σ_h for σ_1, σ_2, and σ_3 in Eq. 18.10,

$$(E_{el})_h = \frac{3}{2}\left(\frac{1 - 2\nu}{E}\right)\sigma_h^2$$

$$= \frac{1 - 2\nu}{6}(\sigma_1 + \sigma_2 + \sigma_3)^2 \quad (18.12)$$

According to von Mises, yielding occurs when the distortion energy, $E_{el} - (E_{el})_h$, exceeds a critical value. This energy density is obtained from Eqs. 18.10 and 18.12 as

$$(E_{el})_d = E_{el} - (E_{el})_h$$

$$= \left(\frac{1 + \nu}{6E}\right)[(\sigma_1 - \sigma_2)^2$$

$$+ (\sigma_1 - \sigma_3)^2 + (\sigma_2 - \sigma_3)^2] \quad (18.13)$$

In the uniaxial tensile test, $\sigma_1 = \sigma_x$, $\sigma_2 = \sigma_y = 0$, and $\sigma_3 = \sigma_z = 0$. Equation 18.13 reduces to

$$(E_{el})_d = 2\left(\frac{1 + \nu}{6E}\right)\sigma_x^2 \quad (18.14)$$

When the right-hand sides of Eqs. 18.13 and 18.14 are equated, the stress σ_x is interpreted as the true stress in a uniaxial tensile test, which is equivalent to the multiaxial stress state characterized by the principal stresses, σ_1, σ_2, and σ_3. The *equivalent stress* is then

$$\sigma_x = \sigma^* = \frac{1}{2^{1/2}}[(\sigma_1 - \sigma_2)^2$$

$$+ (\sigma_1 - \sigma_3)^2 + (\sigma_2 - \sigma_3)^2]^{1/2} \quad (18.15)$$

To emphasize the concept of equivalent stress, we replace the uniaxial stress σ_x with the notation σ^*. This quantity is also called the stress deviator because it pertains only to that portion of the stress system which leads to distortion in specimen shape but does not include the stresses that contribute to volume dilatation.

For the tube-burst test, $\sigma_1 = \sigma_\theta$, $\sigma_2 = \sigma_z = \sigma_\theta/2$, and $\sigma_3 = \sigma_r = 0$. Substituting these stresses into the right-hand side of Eq. 18.15 gives

$$\sigma^* = \frac{3^{1/2}}{2}\sigma_\theta \quad (18.16)$$

Equations 18.15 and 18.16 apply from the yield point to fracture. To determine the internal gas pressure that should cause yielding of a closed tube, we set σ^* equal to σ_Y, the measured yield stress in a tensile test; σ_θ is given by Eq. 18.8a. Equation 18.16 then gives the pressure to cause yielding of the tube

$$p(\text{yielding}) = \frac{4}{3^{1/2}}\frac{t}{D}\sigma_Y$$

The strain deviator analogous to the stress deviator of Eq. 18.15 is defined as

$$\epsilon^* = \frac{2^{1/2}}{3}[(\epsilon_1 - \epsilon_2)^2 + (\epsilon_1 - \epsilon_3)^2 + (\epsilon_2 - \epsilon_3)^2]^{1/2} \quad (18.17)$$

The strain deviator, ϵ^*, is also called the equivalent strain. The coefficient $(2/3)^{1/2}$ arises because we want ϵ^* to reduce to $\epsilon_1 = \epsilon_x$ in a tensile test. Although the stress is uniaxial in the tensile test, the plastic strains are not. The transverse strains are equal to each other, but, because the material is incompressible in plastic flow, we have

$$\epsilon_1 + \epsilon_2 + \epsilon_3 = 0 \quad (18.18)$$

or, with $\epsilon_2 = \epsilon_3$

$$\epsilon_2 = \epsilon_3 = -\frac{1}{2}\epsilon_1$$

and Eq. 18.17 shows that $\epsilon^* = \epsilon_1 = \epsilon_x$, as desired.

For a pressurized tube, $\epsilon_r = -\epsilon_\theta$ (since $\epsilon_z = 0$), and the equivalent strain is given by

$$\epsilon^* = \frac{2(2)^{1/2}}{3}\epsilon_\theta \quad (18.19)$$

where ϵ_0 is given by Eq. 18.9b. The radial strain is difficult to measure during plastic deformation of a tube, but ϵ_0, which is called the *diametral strain*, is more accessible.

Although pressurized-tube-deformation measurements can be used to generate stress—strain curves, tensile tests are much more suitable for this purpose. The principal use of the tube pressurization experiments is to measure the time required to burst the tube under a fixed gas pressure. Since these rupture times are generally rather long (ranging from ~1 to 10,000 hr), the phenomenon is called *creep rupture*. The diametral strain can also be measured at rupture. This quantity is a qualitative indication of the ductility of the specimen. Similarly, the time derivative of the diametral strain is a measure of the creep rate. If steady-state creep (Fig. 8.22) prevails for most of the test, the *rupture time*, t_R, is given by

$$ t_R = \frac{\epsilon_F}{\dot{\epsilon}} \tag{18.20} $$

where ϵ_F is the diametral strain at failure and $\dot{\epsilon}$ is the creep rate, which is assumed to be constant for $0 < t < t_R$.

Figure 18.12 shows typical stress-rupture curves for type 316 stainless steel at various temperatures. The stress

of the two testing methods are indeed collapsed into single curves when plotted according to Eq. 18.21.

18.3.3 Impact Testing and Transition Temperatures

One of the major differences between the mechanical behavior of austenitic and ferritic steels is that ferritic steels tend to become brittle at low temperatures, whereas austenitic steels remain ductile to as low temperatures as it is possible to reach in tensile tests. The degree of ductility or brittleness is related to the strain at fracture (the point F in Fig. 18.10). As the temperature at which a tensile test is conducted is reduced, the fracture stress becomes smaller and eventually coincides with the onset of yielding. Another measure of the ability of a metal to deform plastically before fracture is the energy per unit volume required for fracture. This quantity, which is called *toughness*, is the area under the stress—strain curve up to point F in Fig. 18.10. Determining the energy of fracture by measuring and then integrating a complete stress—strain curve is tedious, and quicker methods, known as impact tests, have been devised. These tests are not intended to
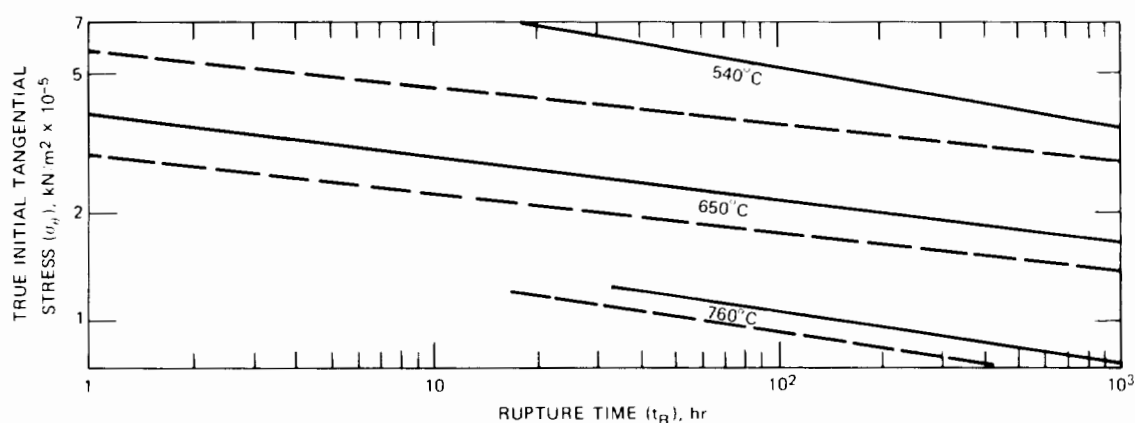

Fig. 18.12 Rupture life of unirradiated type 316 stainless steel.——, uniaxial.- - -, biaxial. (After A. J. Lovell and R. W. Barker, in ASTM Special Technical Publication 484, p. 468, American Society for Testing and Materials, Philadelphia, 1970.)

dependence of the rupture time can be obtained by substituting Eq. 8.46 for $\dot{\epsilon}$ into Eq. 18.20. If the diametral rupture strain is considered constant for tests at different stresses and temperatures, we obtain

$$ \sigma_0 \propto \left[t_R \exp\left(-\frac{E}{kT}\right) \right]^{-1/m} \tag{18.21} $$

In this equation, E is the activation energy for steady-state creep.

For dislocation climb creep (Sec. 16.7), the exponent m is ~4, so the slope of the creep-rupture line on a log—log plot should be 0.2—0.3. Figure 18.12 confirms this expectation. Equation 18.21 also suggests that the temperature dependence of the stress—rupture plot can be removed by plotting the stress as a function of the product $t_R \exp(-E/kT)$ rather than simply t_R. The compound variable is called the Dorn theta parameter. The curves in Fig. 18.12 for each

provide an accurate measure of the true energy of fracture; rather they can quickly and reproducibly indicate the effect of such variables as temperature and radiation on the change in the brittle characteristics of ferritic steels. Impact tests are generally referred to as comparative tests as opposed to tensile and tube-burst tests, which are designed to measure one or more well-defined mechanical properties of the metal.

The most commonly used impact test for mild steels is the Charpy V-notch test illustrated in Fig. 18.13(a). A notched specimen of standard size and shape (1 by 1 by 6 cm^3) is end-mounted in a holder (shown as the solid triangles in the drawing). A hammer attached to the end of a pendulum is raised to an initial height h_1 above the specimen which corresponds to an energy of 325 J at the moment of contact with the specimen. The difference between the initial and final heights of the hammer
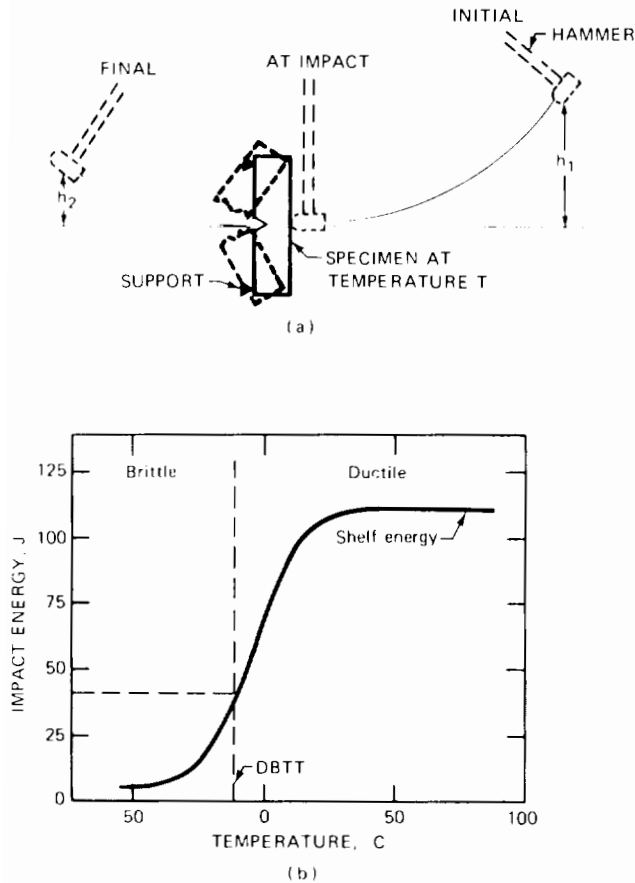
Fig. 18.13 The Charpy V-notch test. (a) Test setup. (b) Variation of absorbed energy with temperature.

$(h_1 - h_2)$ gives the energy absorbed by the specimen in the fracture process. When Charpy tests are performed on specimens at different temperatures, the absorbed energy (called the impact energy) varies as shown in Fig. 18.13(b). The impact energy increases from < 15 J at low temperatures to a high-temperature plateau known as the shelf energy, which is typically 100 to 150 J. The transition occurs over a rather narrow temperature range, and the temperature at which the impact energy is 40.7 J is arbitrarily used to separate the ductile and brittle regimes. This temperature is called the *ductile—brittle transition temperature* (DBTT). For unirradiated mild steels, the DBTT is between −50 and 20°C.

The drop weight test illustrated in Fig. 18.14 is perhaps the simplest of the impact class of tests designed to assess the susceptibility of a metal to brittle fracture. In this test a bead of weld material is deposited on the bottom of a test plate (9 by 35 by 2.5 cm^3), and a small crack or notch is made in the weld. The test consists of dropping a weight from a fixed height on top of the plate directly over the bead. The height of the end supports for the plate is fixed so that the maximum deformation of the specimen corresponds to 5° of bend. At low temperatures the specimen fractures in the test. As the test temperature is increased, a temperature is reached at which the fracture does not extend through the entire thickness of the plate. This

temperature is called the *nil ductility temperature* (NDT). At temperatures above the NDT, the specimen bends under impact but does not break. The NDT is approximately equal to the DBTT obtained from the Charpy test. Because the small size of the Charpy test specimens make them easier to load into capsules for irradiation, most irradiation embrittlement studies are made with the Charpy test. However, the NDT correlates well with the DBTT, and the two terms are used interchangeably.
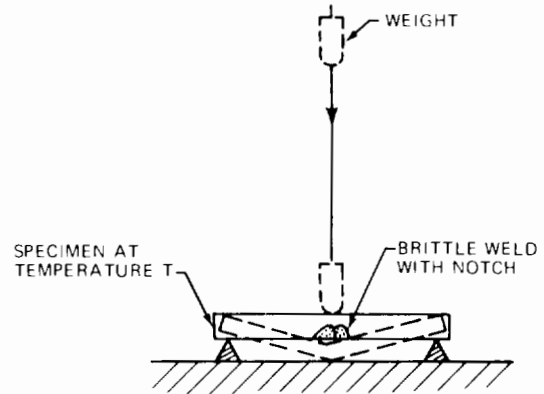

Fig. 18.14 The drop-weight impact test.

Because of the empirical nature of the impact tests, neither transition temperature has a well-defined theoretical significance. However, changes in the DBTT or the NDT due to neutron irradiation can be related to fracture theory.

18.4 THEORIES OF RADIATION HARDENING

Over 20 years of intensive experimental effort has established that exposure of all metals to fast-neutron irradiation results in an increase in the yield strength. In ferritic steels this radiation hardening appears as an increase in the lower yield point. Irradiation causes an increase in the 0.2% offset yield strength of austenitic steels and may even result in the development of a stress—strain curve that exhibits a definite yield point (i.e., the curve resembles that shown in Fig. 18.10 rather than that of Fig. 18.11).

Typical engineering stress—strain curves for the two types of steels are shown in Fig. 18.15. In addition to increasing yield strength with irradiation, the ductility (as measured either by total elongation or by uniform elongation) is reduced. The curves shown for the two types of steels apply only when the testing temperature is low [less than one-half or two-thirds the melting point (°K), depending on the neutron fluence]. Austenitic steels irradiated and tested at high temperatures show no increase in either yield or ultimate strength; only the ductility reduction persists [bottom curve of Fig. 18.15(a)]. When bcc metals are irradiated and tested at high temperatures, the stress—strain curve of the unirradiated material is completely recovered. Whatever radiation-produced defects are responsible for strengthening and the loss of ductility are removed by annealing processes at high temperatures.
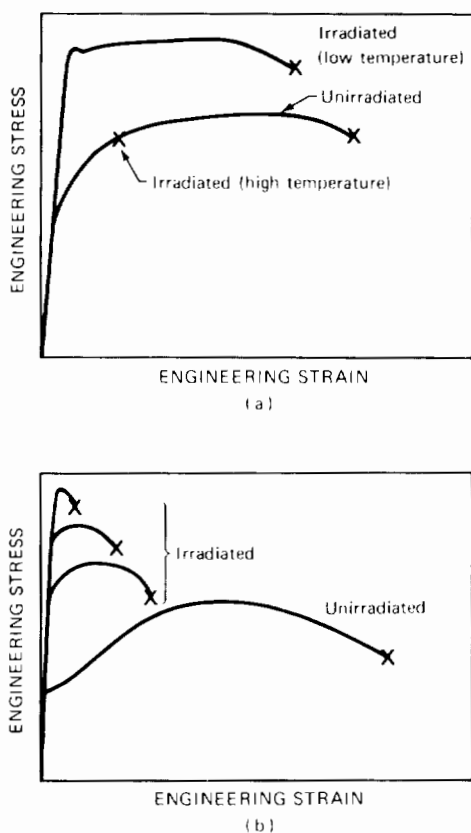
Fig. 18.15 Effect of fast-neutron irradiation on the tensile properties of reactor steels. (a) Face-centered cubic structure. (b) Body-centered cubic structure.

For both the austenitic and ferritic steels, irradiation increases the yield strength much more than it does the ultimate tensile strength. The approach of the yield strength to the UTS as a result of irradiation is responsible for the ductility loss. The upper curve in Fig. 18.15(b) shows a case in which the yield and ultimate strengths coincide. When this occurs, there is no uniform elongation, and necking begins as soon as the specimen departs from the line representing elastic straining. In the bcc metals, when the testing temperature is low enough and the irradiation exposure large enough, there may not even be a region of necking deformation; the specimen can fracture while still on the elastic line. Such specimens are totally brittle.

Radiation hardening in both fcc and bcc metals is attributed to the production by radiation of various defects within the grains. Defects produced by neutron irradiation of metals include

1. Point defects (vacancies and interstitials).

2. Impurity atoms (atomically dispersed transmutation products).

3. Small vacancy clusters (depleted zones).

4. Dislocation loops (faulted or unfaulted, vacancy or interstitial type).

5. Dislocation lines (unfaulted loops that have joined the dislocation network of the original microstructure).

6. Cavities (voids and helium bubbles).

7. Precipitates (in the case of stainless steel, $M_{23}C_6$ carbides or intermetallic phases).

In this section theories that predict the increase in strength due to defects 3 through 7 in the list are presented. Point defects and impurity atoms are believed to contribute negligibly to hardening compared to the effect of the larger defect clusters.

Radiation strengthens a metal in two different ways: (1) It can increase the stress required to start a dislocation moving on its glide plane. Resistance to dislocation startup is called *source hardening*. The applied stress required to release a dislocation into its slip plane is called the *unpinning* or *unlocking* stress. (2) Once moving, dislocation can be impeded by natural or radiation-produced obstacles close to or lying in the slip plane. This is called *friction hardening*.

18.4.1 Source Hardening

In unirradiated fcc metals, the stress required to initiate dislocation motion can be identified with the unpinning stress of the Frank–Read sources in the metal (Eq. 8.16), which is inversely proportional to the distance between pinning points.[1] The gradual onset of yielding characteristic of this class of metals can be explained by the distribution of stresses required to operate the sources. At low applied stress, the sources easiest to operate (i.e., those with large separation between pinning points) generate dislocations. Plastic strain ceases when pileups produce a back stress on the sources which stops their operation. As the stress is increased, more dislocation sources operate and the strain increases. The multiplication of dislocations in the crystal causes tangling of the moving dislocations, and additional applied stress is necessary for parallel dislocations to move past each other or for nonparallel dislocations to cut through each other. This process of work hardening causes the smooth increase in stress as a function of strain illustrated in Fig. 18.11.

Although source hardening is not found in unirradiated fcc metals and alloys, this phenomenon is common in bcc metals in the unirradiated state. Source hardening is manifest by upper and lower yield points in the stress–strain curve. Unirradiated ferritic steels show this effect quite clearly [Figs. 18.10 and 18.15(b)]. In fcc metals the yield drop that indicates the presence of source hardening is observed only after irradiation [Fig. 18.15(a)]. The development of source hardening in irradiated fcc metals is probably due to the irradiation-produced defect clusters in the vicinity of Frank–Read sources. These obstacles raise the stress required to expand the loops and to permit multiplication to continue, which is tantamount to increasing the stress required to operate the source. Once the stress level is sufficient to release the source, the moving dislocations can destroy the small defect clusters (loops) and thus reduce the stress needed to continue deformation. Therefore, a yield drop similar to that observed in unirradiated ferritic steel is found in irradiated austenitic steel but for a quite different reason. (The origin of source hardening in unirradiated ferritic steels is discussed in Sec. 18.12.)

18.4.2 Friction Hardening

The forces responsible for resisting the motion of a dislocation through the crystal can be characterized as long range or short range. The total applied shear stress necessary to move the dislocation is the sum of the long-range and short-range stresses:

$$\sigma_i = \sigma_{LR} + \sigma_s \qquad (18.22)$$

where σ_i is the friction stress and the subscripts LR and s represent the long-range and short-range contributions, respectively. An increase in σ_i due to irradiation, to work hardening, or to aging is termed friction hardening. The friction stress is roughly equal to the true stress at any point in the plastic deformation region of the stress—strain plot.

Long-Range Stresses

The long-range forces[2] arise from the repulsive interaction between the moving dislocation and the components of the dislocation network of the solid. Although the dislocation network of a metal does not resemble a regular array, it is often represented as a series of cubes the edges of which are formed of dislocation lines. Figure 18.16 shows such an idealized dislocation network with a loop on a glide plane parallel to the top and bottom faces of the cube. The long-range forces are due to the interaction of the stress fields of the dislocation forming the loop and of the network dislocations that make up the edges of the top and bottom planes of the cube, which are parallel to the loop. For simplicity, assume that the interaction forces between the loop and the network dislocations parallel to it can be approximated by the force between parallel edge dislocations (Eq. 8.24). Setting $f_x(\theta)$ equal to its maximum value of $1/4$, taking $1 - \nu \simeq 1/2$, and approximating the distance between the loop and the nearest parallel network dislocation as one-half the cube side ($y \simeq 1/2$), we obtain the long-range force on the moving dislocation,

$$F_{LR} \simeq \frac{Gb^2/4}{(2\pi)(\tfrac{1}{2})(1/2)} = \frac{Gb^2}{2\pi l}$$

The stress needed to overcome this force is F_{LR}/b; thus,

$$\sigma_{LR} = \frac{Gb}{2\pi l} \qquad (18.23)$$

The dislocation network depicted in Fig. 18.16 is the same as that employed in the BUBL swelling code (Sec. 13.12). From Eq. 13.280, the length l is related to the dislocation density ρ_d by

$$l = \left(\frac{3^{\frac{1}{2}}}{\rho_d}\right) \qquad (18.24)$$

Any process that increases the dislocation density of the material (e.g., cold working, unfaulting of radiation-produced prismatic loops, or work hardening) decreases l and increases the long-range stress on mobile dislocations.

In addition to dislocations in the network, pileups of dislocations on slip planes parallel to the slip plane of an expanding loop can exert long-range forces capable of resisting and even stopping motion of the mobile dislocation (Fig. 8.18).
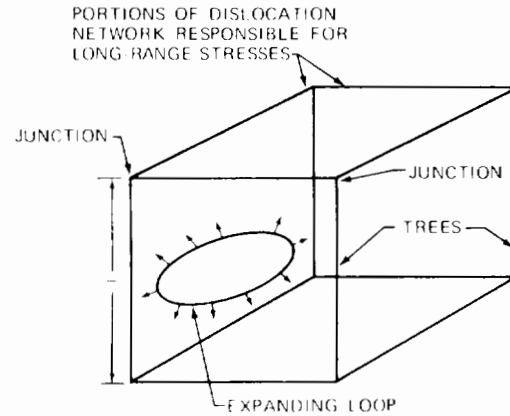

Fig. 18.16 Model of the dislocation network in a solid.

Short-Range Stresses

Short-range forces are due to obstacles that lie in the slip plane of the moving dislocation (these represent what are called *planar barriers*). The short-range forces are active only when the moving dislocation comes very close to or contacts the obstacle. Such obstacles exert a force on the moving dislocation only at the point of contact. Short-range forces can be further subdivided into athermal and thermally activated components. An athermal stress component is one whose magnitude is independent of temperature. Athermal mechanisms normally involve bowing of a dislocation around an impenetrable obstacle. In a thermally activated process, overcoming the obstacle usually requires that the moving dislocation cut through or climb over the barrier in its path. Inasmuch as passage of a dislocation line through or over an obstacle requires energy that can be partly supplied by thermal fluctuations, the thermally activated component of the short-range stresses decreases with increasing temperature.

The friction stress due to a dispersion of barriers depends on the average separation between the obstacles in the slip plane of the moving dislocation (not the average separation between obstacles in three dimensions). Figure 18.17 shows a unit area of a slip plane that is intersected by portions of spherical objects of radius r which are randomly
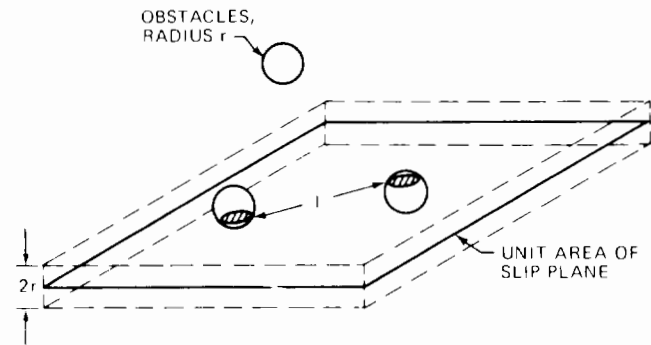

Fig. 18.17 The intersection of spherical obstacles with a slip plane to form an array of planar barriers.

distributed throughout the solid at a concentration N cm^{-3}. Any sphere that has its center within the slab of volume $2r$ centered on the slip plane intersects the slip plane. The number of obstacles in this volume element is $2rN$, which is also the number of intersections per unit area on the slip plane. Since the inverse square of the average obstacle spacing along the slip plane (l^{-2}) is equal to the density of intersections on the plane, we have

$$l = \frac{1}{(2rN)^{1/2}} \qquad (18.25)$$

18.5 HARDENING BY DEPLETED ZONES

At low temperatures and low fluences, the main microstructural effect of the neutron irradiation of steel is the production of depleted zones. The irradiation conditions that result in depleted-zone damage exclusively are most likely to be found in the region of the reactor pressure vessel. Core components are subject to high-temperature and high-fluence conditions that produce the larger defects listed at the beginning of Sec. 18.4. However, hardening due to depleted zones has been observed in both austenitic and ferritic steels at low temperature and low fast-neutron fluence. The effect of the depleted zones on mechanical properties can be classified as friction hardening of the short-range thermally activated type. A theory proposed by Seeger[3] for the radiation strengthening of metals due to the formation of depleted zones is reviewed in this section.

A dislocation line wending its way through a metal containing a uniform distribution of depleted zones is pressed against a number of these obstacles at all times. The plane of the drawing in Fig. 18.18(a) represents the slip plane of the dislocation, which is shown as the solid line pressed against the obstacles A, B, and C under the influence of the applied shear stress. According to Eq. 18.22, the net stress available for moving the dislocation through the metal is the difference between the applied stress (σ_i) and the stress necessary to move the dislocation against the long-range forces of the dislocation network naturally present in the solid (σ_{LR}). Thus, the dislocation segments between obstacles A, B, and C are acted on by a shear stress $\sigma_s = \sigma_i - \sigma_{LR}$. Because of this applied stress, dislocations move through the field of obstacles and thereby produce a macroscopic strain rate $\dot{\epsilon}$ in the solid. However, the motion of each dislocation line is jerky rather than smooth, and the entire dislocation line does not move at the same time. The line progresses from the left to the right in Fig. 18.18(a) as points on the dislocation line cut through obstacles one at a time. Thus, the line is held up at points A, B, and C; but, with the help of thermal fluctuations, enough energy can be supplied for the line to penetrate the obstacle at B. When this event occurs, the line quickly moves to the position shown by the dashed line, where it is pressed against obstacles A, D, and C. The area of the slip plane sheared by this elementary step is shown as the dotted zone.

In general, the distance l_0 between pinning points is greater than the average separation of obstacles in the slip plane (l given by Eq. 18.25). The distance that the dislocation advances when the obstacle B is cut is denoted
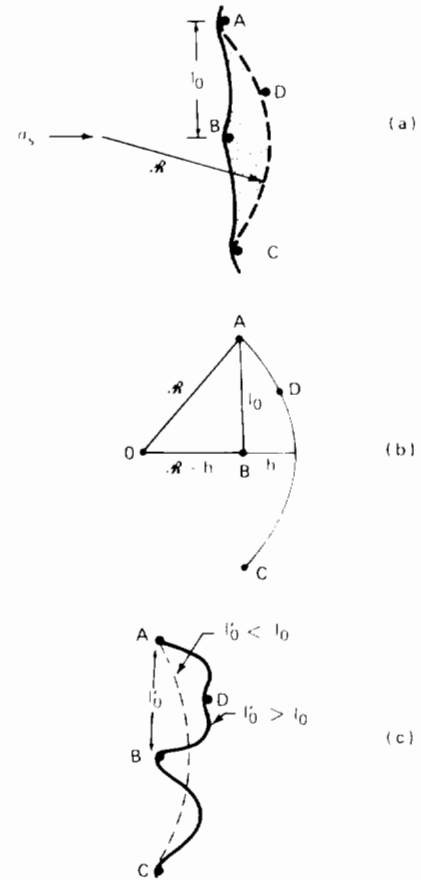

Fig. 18.18 A dislocation line pressed against depleted zones in its slip plane. A, B, C, and D are pinning points.

by h in Fig. 18.18(b). In any array of points on a plane, the larger l_0 is, the smaller h is. In fact, the distances l, l_0, and h are related by (see problem 18.3):

$$l^2 = hl_0 \qquad (18.26)$$

The value of l_0 is determined by the requirement that the curvature of each segment of the dislocation line between pinning points is at all times fixed by the balance between line tension of the dislocation and the net applied stress. Equation 8.15 shows that the radius of curvature of the line under applied shear stress $\sigma_{xy} = \sigma_s$ is

$$\mathcal{R} = \frac{Gb}{\sigma_s}$$

The geometry of Fig. 18.18(b) shows that

$$\mathcal{R}^2 = l_0^2 + (\mathcal{R} - h)^2$$

Combining the preceding three equations and assuming $h/2\mathcal{R} \ll 1$, we obtain

$$l_0 = \left(\frac{2Gbl^2}{\sigma_s}\right)^{1/3} \qquad (18.27)$$

According to this formula, the dislocation line adjusts its orientation in the slip plane according to the applied stress;

it selects positions where the separation between pinning points satisfies Eq. 18.27. The means by which this spacing is attained is illustrated in Fig. 18.18(c), which shows the shapes assumed by the line when the actual pinning point spacing l_0' does not satisfy Eq. 18.27.

When $l_0' < l_0$, the equilibrium bowing of the line after it cuts the obstacle B is shown as the dashed line in Fig. 18.18(c). In this case, the next obstacle, D, is not reached. Because the line remains between the points B and D, the value of l_0' effectively has been doubled, a change that is in the proper direction for rectifying the inequality $l_0' < l_0$.

When $l_0' > l_0$, the dislocation line bows out and touches obstacle D before cutting obstacle B. Therefore, ADBC, not ABC, is the stable configuration of the line before any obstacle is cut. In the solid curve shown in the figure, l_0' is approximately equal to the distances AD or BD, both of which are smaller than the original $l_0' = AB$. Again, the line rearranges its position in a manner that tends to drive the interobstacle distance toward the value expressed by Eq. 18.27.

There is a stress above which Eq. 18.27 is no longer valid. When σ_s is large enough for $l_0 = l$, Eq. 18.27 shows that $\sigma_s = 2Gb/l$. We shall see later that this stress is the critical stress at which a dislocation line can move through an array of obstacles solely by bowing around them. Cutting through the obstacle is no longer a prerequisite to motion.

We next compute the shear strain rate due to the type of dislocation motion described above. The strain rate is given by Eq. 8.21:

$$\dot{\epsilon} = \rho b v_d \qquad (18.28)$$

where ρ is the density of mobile dislocations (total dislocation density less the density of dislocations comprising the immobile network) and v_d is the velocity of the moving dislocations. This velocity is

$$v_d = h\Gamma \simeq l\Gamma \qquad (18.29)$$

where Γ is the probability per unit time that one segment cuts through an obstacle against which it is pressed. For the purpose of computing the dislocation velocity, the distinction between l and l_0 has been neglected. If $l \simeq l_0$, Eq. 18.26 shows that $h \simeq l$.

The cutting frequency Γ is calculated by analogy to the jump frequency of an atom jumping from one equilibrium site to another over the saddle-point energy barrier. To penetrate an obstacle, the segment of the dislocation line in contact with the obstacle must acquire an activation energy U^*, which is supplied by thermal fluctuations. The dislocation line at the obstacle can be imagined to be vibrating with a frequency ν, striking the obstacle at each vibration. The fraction of the vibrations sufficiently strong to penetrate the obstacle is, by analogy to the atomic jump-frequency formula (Eq. 7.41), given by

$$\Gamma = \nu \exp\left(-\frac{U^*}{kT}\right) \qquad (18.30)$$

Substituting Eqs. 18.29 and 18.30 into Eq. 18.28 gives the strain rate:

$$\dot{\epsilon} = \rho l b \nu \exp\left(-\frac{U^*}{kT}\right) \qquad (18.31)$$

The depleted zones are modeled as spheres each of radius r (equal to ~10 Å). The energy U^* is the energy required for the dislocation to cut through the approximately circular region on the slip plane which is intersected by the spherical depleted zone. The shaded circles in Fig. 18.17 depict these intersections. In the absence of applied stress, the variation of the energy with the distance of penetration of the line through the zone resembles the sketch shown in Fig. 18.19(a). The energy rises by an amount U_0 from the point of contact of the line and the zone to the point at which cutting is complete. The average radius of the circle of intersection of the depleted zone and the slip plane is smaller than the radius of the spherical zone proper because the slip plane in general does not pass through the center of the depleted zone (Fig. 18.17). The average radius of the circle of intersection of the zone and the slip plane is (see problem 10.5)

$$r' = \left(\frac{2^{1/2}}{3}\right)r \qquad (18.32)$$

At any point $-r' < x < r'$, the force resisting dislocation motion is $-dU/dx$.

When an applied stress acts on the slip plane, the energy profile is altered as shown in Fig. 18.19(b). The shear stress exerts a force of magnitude $\sigma_s b$ per unit length of dislocation line in the +x-direction. Since the obstacles are
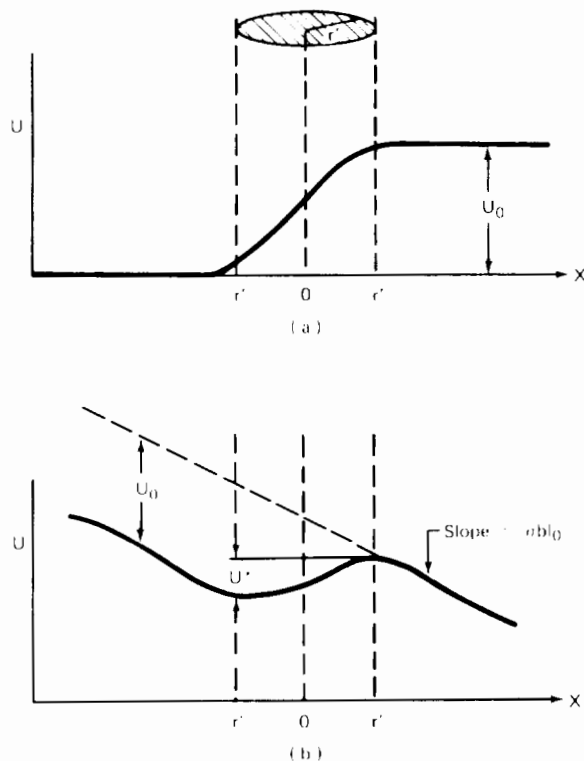

Fig. 18.19 Energy profiles of a dislocation line cutting through a depleted zone. (a) No stress. (b) Shear stress in the x-direction. (From Ref. 3.)

separated by a distance l_0, the force exerted by the applied stress on each obstacle is $\sigma_s b l_0$. Let $U(x,\sigma_s)$ be the shape of the energy profile in Fig. 18.19(b) and $U(x,0)$ be the shape in the absence of applied stress. When a stress is applied, the force at every point during penetration is given by

$$-\frac{d}{dx} U(x,\sigma_s) = -\frac{d}{dx} U(x,0) + \sigma_s b l_0$$

That is, the force in the absence of the stress (the first term on the right-hand side) is reduced by the contribution of the applied stress (the last term). Integrating this equation gives

$$U(x,\sigma_s) = U(x,0) - \sigma_s b l_0 x + \text{constant} \qquad (18.33)$$

Inspection of Fig. 18.19(b) shows that the energy barrier to penetration with an applied stress is reduced from U_0 to

$$U^* = U(r',\sigma_s) - U(-r',\sigma_s) \qquad (18.34)$$

To calculate U^*, we must know the energy profile of Fig. 18.19(a). Seeger assumes it to be of the form

$$U(x,0) = U_0 \left[1 - \frac{1}{1 + \exp(x/r')} \right] \qquad (18.35)$$

The exact functional form of $U(x,0)$ is not important; it simply must have the approximate shape of the curve shown in Fig. 18.19(a), which Eq. 18.35 has. Substituting Eq. 18.35 into 18.33 and forming the difference on the right of Eq. 18.34 yields the following expression for U^* (see problem 18.3 for details):

$$U^* = U_0 \left(1 - \frac{4\sigma_s b l_0 r'}{U_0} \right) \qquad (18.36)$$

When σ_s is large enough to render the right-hand term in the parentheses of this formula larger than unity, the dislocation can cut through the depleted zone without any assistance from thermal fluctuations. The stress σ_s^0 at which the term on the right in the parentheses is equal to unity reduces the barrier height U^* to zero. Thus, σ_s^0 represents the stress required to move dislocations through the obstacles at $0°K$. Using Eq. 18.27 for l_0, Eq. 18.32 for r', and Eq. 18.25 for l, we find

$$\sigma_s^0 = \left[\frac{U_0}{4 \left(\frac{2}{3} \right)^{\frac{1}{2}}} \right]^{\frac{1}{2}} \frac{1}{b^2 G^{\frac{1}{2}}} \frac{N^{\frac{1}{2}}}{r} \qquad (18.37)$$

where σ_s^0 is the maximum frictional hardening due to depleted zones of radius r present in the solid at a volumetric concentration N.

The effect of temperature on depleted-zone hardening can be obtained by solving Eq. 18.31 for U^* and equating the result to the right-hand side of Eq. 18.36. Eliminating l_0, r', and l as before, we obtain

$$\sigma_s = \sigma_s^0 \left[1 - \left(\frac{T}{T_c} \right)^{\frac{2}{3}} \right]^{\frac{1}{2}} \qquad (18.38)$$

where σ_s^0 is given by Eq. 18.37 and T_c is a characteristic temperature given by

$$T_c = \frac{U_0}{k \ln \left[\rho b \nu / \dot{\epsilon} (2rN)^{\frac{1}{2}} \right]} \qquad (18.39)$$

and is not truly constant because it depends on the strain rate $\dot{\epsilon}$ at which the metal is deforming and on the concentration of depleted zones, N, which increases with irradiation time. However, these quantities appear in a logarithmic term, and the effect of their variation on T_c is small enough to be neglected.

The stress σ_s of Eqs. 18.37 to 18.39 represents the radiation hardening due to depleted zones. At temperatures below ~350°C in steel, σ_s is manifest experimentally as the increase in the yield point due to irradiation on the stress—strain curves shown in Fig. 18.15. The hardening effect given by Eq. 18.38 decreases with increasing temperature and disappears entirely for $T > T_c$. At temperatures around 350°C in steel, depleted-zone hardening decreases even more rapidly with increasing temperature than the prediction of Eq. 18.38. In the postirradiation tensile tests that are usually used to measure hardening, high testing temperatures cause annealing (i.e., destruction) of the depleted zones, which results in a decrease in N with increasing temperature.

Seeger's theory has been verified experimentally.[4] Figure 18.20 shows the frictional hardening effect of low-fluence low-temperature neutron irradiation on copper and nickel. Both sets of data are plotted on coordinates suggested by Eq. 18.38. The predicted linear relationship between $(\sigma_s)^{\frac{2}{3}}$ and $T^{\frac{2}{3}}$ is exhibited with high precision by copper. The curve for nickel, however, shows two distinct
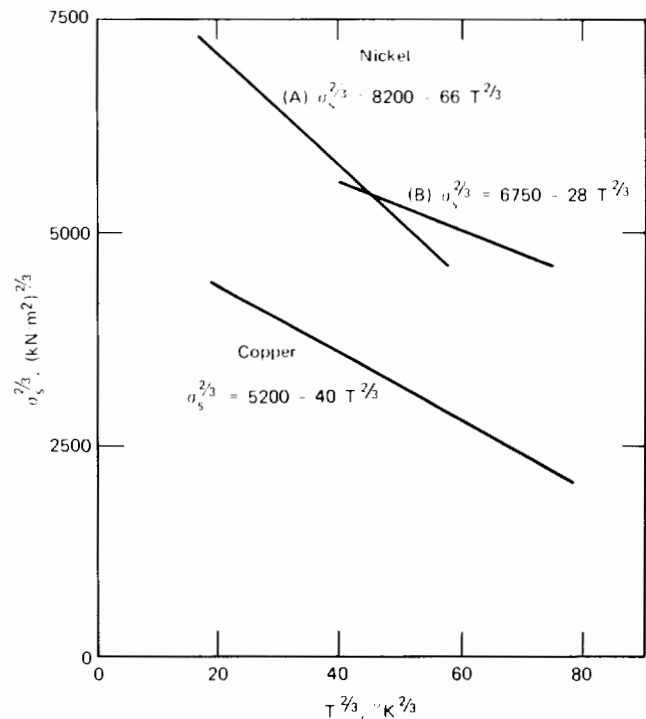

Fig. 18.20 Irradiation hardening of copper and nickel plotted according to Seeger's theory. Fluence, 7×10^{19} neutrons/cm^2; irradiation temperature, 100°C; test temperatures, −200 to 200°C. (From Ref. 4.)

linear segments, which suggests that two types of depleted zones are created by irradiation. The type that predominates at low temperature (type A) apparently has a lower U_0, and hence lower T_c, than does type B (see Eq. 18.39). To a first approximation, U_0 can be considered to be proportional to the area of the circle of intersection of the depleted zone with the slip plane, or $U_0 \propto r^2$. However, type A zones must be created more frequently by neutron collisions with the metal lattice than type B zones, since the hardening at 0°K is greater for type A than type B. In general, a spectrum of zones with continuous distributions of size r and energy barrier U_0 is probably formed by irradiation.

Additional support for Seeger's theory has been obtained by comparing hardening due to neutrons and 4-MeV electrons.[5] The irradiation temperature and the range of tensile-test temperatures were identical for both types of radiation, and the doses were adjusted to produce the same number of Frenkel pairs as calculated by simple cascade theory (Chap. 17). The hardening due to electrons was found to be very small compared to that from neutrons. Using the two-body kinematics appropriate to relativistic electrons, we can show that each 4-MeV electron can transfer a maximum of 66 eV to a copper knock-on. According to the Kinchin—Pease model, this energy transfer produces a cascade consisting of only two or three members. Thus displacement spikes (or depleted zones) cannot be formed by electron irradiation, and the damage consists of isolated vacancies and interstitials. These defects anneal out at very low temperatures (interstitials are mobile at a few tens of °K). By way of contrast, the depleted zones are thermally stable up to $\sim350^\circ$K. In addition, isolated point defects are not as efficient strengtheners as is a vacancy cluster. The virtual absence of radiation hardening due to electron irradiation supports the hypothesis that the depleted zones are real and are responsible for strengthening of metals at low temperatures.

18.5.1 Saturation of Radiation Hardening

According to Eq. 18.37, σ_s should increase as $(N)^{1/2}$. In the absence of mechanisms of destruction of the depleted zones, N is proportional to the total neutron fluence, and the theory at this stage predicts that

$$\sigma_s \propto (\Phi t)^{1/2} \qquad (18.40)$$

Two models have been proposed to explain the observation that hardening does not follow this formula at high fluence. Both of these theories introduce processes that remove depleted zones and thereby permit a steady-state value of N to be attained at large fluence.

18.5.2 Makin's Theory

Makin and Minter[4] postulate the existence of a volume v around each depleted zone within which no new zone can be formed. This notion appears to be contrary to the computer experiments simulating radiation damage, which showed that cascade overlap causes the zone to grow (Fig. 17.30). However, a single large zone created by, say, n

displacement spikes in a localized region can be a less effective hardener than n smaller, isolated zones.

To predict the increase of the depleted-zone concentration with fluence, the rate of production of zones must be estimated. There are $\Sigma_s\Phi$ neutron collisions cm^{-3} sec^{-1} with lattice atoms, where Σ_s is the macroscopic scattering cross section and Φ is the total fast flux. If the average fast-neutron energy is 0.5 MeV (typical of FBR spectra) and A = 56 (iron), Eq. 17.114 shows that the average energy of the knock-ons is ~20 keV. The depleted zone responsible for radiation hardening is believed to be restricted to clusters containing 10 or more vacancies. The distribution of vacancy-cluster sizes resulting from knock-ons of 20 keV is shown in Fig. 17.29(b). The number of point defects included in the cluster distribution shown in this figure is ~200, of which $\sim5\%$, or ~10 vacancies, are contained in a cluster of ~10 members. Therefore, one cluster containing more than 10 vacancies is formed by the average fast-neutron collision in iron. The time rate of change of the density of clusters of this size is given by

$$\frac{dN}{dt} = \alpha\Sigma_s\Phi \,(1 - vN)$$

where α is the number of clusters (zones) created per neutron collision. It is approximately unity. The term in parentheses represents the fraction of the solid volume which, according to Makin's theory, is available for the creation of new depleted zones. The fraction vN of the volume is inactivated by the presence of the depleted zones. Integration of the preceding differential equation yields

$$N = \frac{1}{v} \,[1 - \exp(-\alpha v\Sigma_s\Phi t)] \qquad (18.41)$$

which, when used in Eq. 18.37, predicts

$$\sigma_s \propto [1 - \exp(-\alpha v\Sigma_s\Phi t)]^{1/2} \qquad (18.42)$$

The capture volume v has been estimated from radiation-hardening data to be between 50 and 80 Å equivalent spherical diameter.[6] This size can be compared with the estimated 20-Å diameter of the depleted zone proper, which occupies the center of the capture volume.

18.5.3 Thermal Annealing of Depleted Zones

We have mentioned that thermal annealing is a potential mechanism for destroying depleted zones. Dollins[7] has presented an analysis of depleted-zone dynamics which includes thermal annealing. The object is to predict the concentration of depleted zones as a function of neutron fluence and temperature. It is assumed that one depleted zone of radius R_0 is formed per neutron collision with a lattice atom. Once formed, the zone serves as a sink for free vacancies and interstitial atoms that are created along with the depleted zones in the collision cascade. Because the zone can absorb point defects that reach it by diffusion, there will be a size distribution of zones, N(R,t), at any time t during irradiation. The conservation of depleted zones can be formulated in a manner similar to that applied to determine the size distribution of fission-gas bubbles in the fuel, which grow by absorption of atomically dispersed xenon and krypton (Sec. 13.9). This type of conservation

statement, which focuses on a fixed particle-size interval and equates the difference in fluxes across the boundaries of the interval to the time derivative of the particle concentration, is appropriately termed *Eulerian*. In many cases an equally acceptable conservation principle can be formulated in a *Lagrangian* manner by following a small group of particles from the time they are created up to current time. The size of the particle as it ages is determined by a growth law, dR/dt, which is appropriate to the particular system. For example, the growth law for a cavity in a solid supersaturated with point defects is given by Eq. 13.171. This growth law can be applied to the depleted zones:*

$$\dot{R} = \frac{dR}{dt} = -\frac{\Omega}{R}[D_iC_i - D_v(C_v - C_{vR})]$$

The very low equilibrium interstitial concentration permits C_{iR} to be neglected. The vacancy concentration at the surface is obtained by treating the zone as a small void, for which the C_{vR} is obtained from Eq. 13.176 with the internal-gas-pressure term neglected:†

$$C_{vR} = C_v^{eq}\exp\left(\frac{2\gamma\Omega}{RkT}\right)$$

Combining these equations yields

$$\dot{R} = -\frac{\Omega}{R}\left\{D_iC_i - D_v\left[C_v - C_v^{eq}\exp\left(\frac{2\gamma}{R}\frac{\Omega}{RT}\right)\right]\right\} \quad (18.43)$$

The steady-state point-defect balances that serve to fix C_v and C_i are similar to Eqs. 13.186 and 13.187. For this calculation the defect production rates are determined in the following manner. Because some of the vacancies produced in the collision cascade initiated by a fast neutron are contained in the depleted zone formed at the same time as the free point defects, the yield Y_{vi} is replaced by ν_i interstitials and ν_v free vacancies per primary knock-on atom (PKA). These quantities are related to the size of the nascent depleted zone (only one is assumed formed per neutron collision) by

$$\nu_i = \nu_v + \frac{4\pi R_0^3/3}{\Omega} \quad (18.44)$$

---

*In the growth law used by Dollins,[7] the second term in the brackets appears multiplied by R/a_0, where a_0 is the lattice constant. This difference arises from the assumption of reaction-rate-controlled vacancy capture by the depleted zone instead of the diffusion-limited capture assumed in this equation. Comparison of Eqs. 13.70 and 13.95 shows that these two limiting rates differ by a factor of R/a_0. The interstitial capture rate by the zone (the first term in the growth law), on the other hand, is taken by Dollins to be diffusion controlled. For consistency, we will assume diffusion-limited kinetics for both types of point-defect capture by the depleted zones. The mixed control formula, Eq. 13.96, is probably most appropriate because of the small zone radii but, for simplicity, will not be employed.

†The argument of the exponential term of C_{vR} in Dollins' analysis[7] is the difference between the vacancy-formation energy and the binding energy of a vacancy to the depleted zone. If the zone is large enough to be treated as a macroscopic cavity, the capillarity formulation used above is applicable.

where ν_i is computed from isolated cascade theory (e.g., the Kinchin—Pease model) and reduced by the vacancy—interstitial annihilation that takes place during cascade formation. In Dollins' analysis ν_i is estimated to be 10% of the Kinchin—Pease value.

The PKA production rate on the left in Eqs. 13.186 and 13.187 (i.e., what has been termed $\dot{F}$ when the bombarding particles are fission fragments) is written as $\Sigma_s\Phi$, the fast-neutron collision density.

The numbers Z_i and Z_v in Eqs. 13.186 and 13.187 are given by the last terms of Eqs. 13.182 and 13.183. Neglecting the first terms on the right-hand sides of these formulas is equivalent to assuming that point-defect absorption by dislocations is purely diffusion controlled. The dislocation-core radius is assumed to be the same for vacancies and interstitials (i.e., $Z_i = Z_v = Z$).

The interstitial supersaturation is assumed large enough to neglect C_i^{eq} compared to C_i.

Finally, Eqs. 13.186 and 13.187 are supplemented by additional terms representing the absorption of point defects by the depleted zones, and the point-defect balances become

$$\nu_i\Sigma_s\Phi = Z\rho_dD_iC_i + k_{iv}C_iC_v$$
$$+ \int_0^{R_0}4\pi D_iRC_i\,N(R,t)\,dR \quad (18.45a)$$

$$\nu_v\Sigma_s\Phi = Z\rho_dD_v(C_v - C_v^{eq}) + k_{iv}C_iC_v + \int_0^{R_0}4\pi D_vR$$

$$\times\left[C_v - C_v^{eq}\exp\left(\frac{2\gamma}{R}\frac{\Omega}{RT}\right)\right]N(R,t)\,dR \quad (18.45b)$$

The integrals are terminated at $R = R_0$ because the zones shrink rather than grow; so the newly created zones are the largest in the distribution.

The size distribution of depleted zones can be determined as follows. The zones in the size range R to $R + dR$ at time t are those which were created (at size R_0) in a previous time interval $d\tau$ at τ, or

$$N(R,t)\,dR = \Sigma_s\Phi\,d\tau \quad (18.46)$$

This conservation statement is equivalent to conserving depleted zones in a fixed size range (e.g., by adapting Eq. 13.196 to depleted zones). Using the preceding reaction, we obtain the distribution function:

$$N(R,t) = \Sigma_s\Phi\left|\frac{\partial\tau}{\partial R}\right|_t$$

The shrinkage law is employed to determine the ratio of the intervals $d\tau$ and dR (i.e., the Jacobian of the transformation between R and τ). The value R, which is the radius at time t of a zone created at time τ, can be obtained by integrating Eq. 18.43 provided that only the steady-state situation is considered. In this case C_i and C_v are constants and $\dot{R}$ is a function of R alone. Integration yields

$$\int_{R_0}^{R}\frac{dR'}{\dot{R}} = \int_{\tau}^{t}dt' = t - \tau \quad (18.47)$$

Differentiating with respect to R yields

$$\left|\frac{\partial \tau}{\partial R}\right|_t = -\frac{1}{\dot{R}}$$

and the distribution function of zones at steady state is

$$N(R) = -\frac{\Sigma_s \Phi}{\dot{R}}$$

$$= \frac{\Sigma_s \Phi}{\Omega} \frac{R}{D_i C_i - D_v \left[C_v - C_v^{eq} \exp\left(\frac{2\gamma}{R}\frac{\Omega}{RT}\right)\right]} \quad (18.48)$$

Note that analytic integration of the shrinkage law cannot be performed in the unsteady state when C_i and C_v are time dependent.

Subtracting Eq. 18.45b from Eq. 18.45a and using Eq. 18.44 yields

$$\left(\frac{4}{3}\pi R_0^3\right)\frac{\Sigma_s \Phi}{\Omega} = Z\rho_d \mid D_i C_i - D_v (C_v - C_v^{eq}) \mid$$

$$+ 4\pi \int_0^{R_0} \left\{ D_i C_i - D_v \left[C_v \right. \right.$$

$$\left. \left. - C_v^{eq} \exp\left(\frac{2\gamma}{R}\frac{\Omega}{kT}\right)\right] \right\} RN(R) \, dR$$

Substituting Eq. 18.48 into this equation, we find that the left-hand side is identical to the second term on the right, which leads to the following relation between C_i and C_v:

$$D_i C_i - D_v (C_v - C_v^{eq}) = 0 \quad (18.49)$$

and Eq. 18.48, after the exponential term is expanded in a two-term Taylor series, simplifies to

$$N(R) = -\frac{\Sigma_s \Phi R^2}{D_v C_v^{eq} \Omega^2 (2\gamma/kT)} \quad (18.50)$$

The total density of depleted zones at steady state is obtained by integrating the distribution $N(R)$,

$$N = \int_0^{R_0} N(R) \, dR = -\frac{\Sigma_s \Phi R_0^3}{3 D_v C_v^{eq} \Omega^2 (2\gamma/kT)} \quad (18.51)$$

If desired, the concentrations C_i and C_v can be determined by inserting Eqs. 18.49 and 18.50 into either of the point-defect balances (Eq. 18.45a or Eq. 18.45b) and solving for one of the point-defect concentrations. Equation 18.49 then determines the other.

Dollins[7] treated the unsteady-state case of depleted-zone formation and annealing, of which the preceding analysis represents the limit as t → ∞(saturation). The variation of the depleted-zone concentration according to Dollins' thermal-annealing model is compared with Makin's capture-volume mechanism (Eq. 18.41 with a capture volume equivalent to a 75-Å diameter sphere) in Fig. 18.21. The agreement between the saturation-zone densities predicted by the two methods is somewhat fortuitous, inasmuch as the $N(\infty)$ predicted by Makin's theory is inversely proportional to the cube of the capture-volume radius. Even with v taken to give approximately equal saturation concentrations from the two models, the
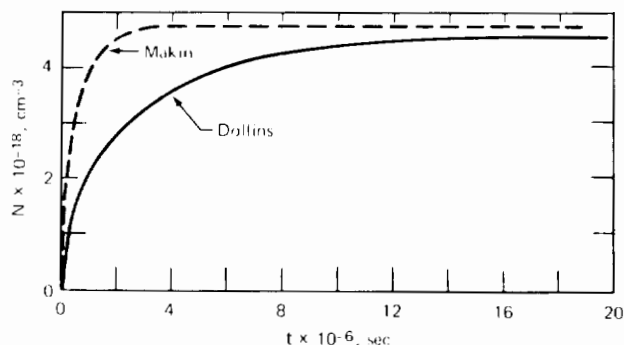

Fig. 18.21 Approach to saturation of the concentration of depleted zones in an irradiated metal. For Makin's model the capture volume has been assumed to be 75 Å in diameter. The following parameters were used in Dollins' computation: $D_v = 0.38 \exp(-117,000/RT) \text{ cm}^2/\text{sec}$; $D_i = 7.5 \times 10^{-4} \exp(-29,000/RT) \text{ cm}^2/\text{sec}$; $r_d = 3.23 \text{ Å}$; $\Omega = 24 \text{ Å}^3$; $\Sigma_s = 0.16 \text{ cm}^{-1}$; $C_v^{eq} = \exp(-117,000/RT)/\Omega$ cm^{-3}; $R_0 = 7.95 \text{ Å}$; $\Phi = 10^{14}$ neutrons $\text{cm}^{-2} \text{sec}^{-1}$; $T = 573°K$; $\rho_d = 5 \times 10^{10} \text{ cm}^{-2}$; $\gamma = 250 \text{ dynes/cm}$; and $\nu_i = 90$. Activation energies in J/mole.

thermal-annealing analysis predicts a much slower approach to saturation than does Makin's simpler model. The reason for this is the built-in time lag in the annealing calculation due to the necessity of diffusing point defects to the zones to make the zones shrink. Makin's capture-volume calculation, on the other hand, provides a mechanism for instantaneous reduction in the rate of zone formation.

The thermal-annealing computation is extremely sensitive to the value of R_0 selected. The $N(\infty)$ is temperature insensitive in Makin's analysis but is very sensitive to temperature if thermal annealing is responsible for depleted-zone destruction. A drastic drop in the steady-state concentration of zones is calculated to occur between 300 and 450°C, although this result is also highly dependent on input parameters in the annealing analysis.

18.6 HARDENING BY IMPENETRABLE OBSTACLES—PRECIPITATES AND VOIDS

Often the barriers that lie in the glide plane of a moving dislocation cannot be cut by the dislocation as could the depleted zones. A dislocation line moves through a field of impenetrable obstacles by bowing around them. The increased strength produced by obstacles of this sort is often exploited in the metal treatment called precipitation hardening. Neutron irradiation can precipitate $M_{23}C_6$ carbides or hard intermetallic phases consisting of the major components of steel (e.g., the sigma phase).

There is usually a misfit between the precipitate particle and the matrix in which the particle is lodged. If the precipitate volume is larger than the metal it replaced, the particle acts as a point center of compression and creates a stress field in the surrounding solid. A dislocation "feels" the presence of such a particle (which is called a *coherent*

precipitate) via the stress field before actual contact is made. On the other hand, if the precipitate occupies a smaller volume than the material that has been replaced, there are no internal stresses in the solid around the foreign particle. For these *incoherent* precipitates, the dislocation must physically contact the particle before the interaction force is appreciable.

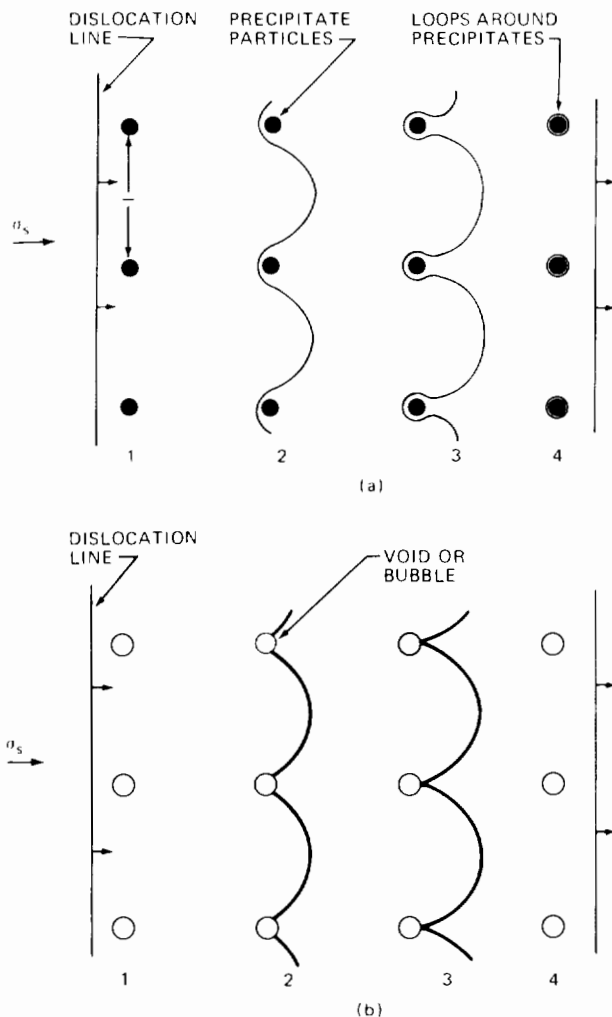Figure 18.22(a) illustrates a mechanism by which a moving dislocation line (or a portion of an expanding

Fig. 18.22 Passage of a dislocation through an array of barriers intersecting the glide plane of the dislocation. (a) Precipitate particles. (b) Cavities (voids or helium bubbles).

dislocation loop) negotiates an array of precipitate particles in its glide plane. Four stages of the process are shown in the drawing. Having been stopped by the particles (1), the line bows out between contact points because of the effective stress, which is the applied shear stress less the internal stresses due to long-range forces (2). When the applied stress is high enough to result in a radius of curvature of the bowed segments which is equal to one-half the interparticle spacing, the semicircular sections on either side of a particle meet (3) and pinch off, in much the same

manner as a Frank—Read dislocation source operates (Fig. 8.13). The final state (4) is a free dislocation line and precipitate particles surrounded by small dislocation rings left as debris of the interaction.

At the pinch-off point, R in Eq. 8.15 is $1/2$, and the stress needed to force passage of a dislocation line through the obstacle array is:

$$\sigma_s = \frac{2Gb}{l} \qquad (18.52)$$

The factor of 2 arises because the line tension of the dislocation has been taken as Gb^2. Had the line tension been given by $Gb^2/2$, the factor of 2 would not appear. The particle-separation distance on the glide plane, l, is given by Eq. 18.25, in which N is the volumetric concentration of precipitate particles and r is their radius.

Equation 18.52, which is called the Orowan stress, is the largest possible resistance to dislocation motion for an array of barriers of planar spacing l. It has been derived assuming a regular pattern of obstacle intersections with the glide plane. If the array were random (as it actually is), the Orowan stress would be reduced by ~20%. This reduction, however, is less than the factor of 2 uncertainty in the numerical coefficient of Eq. 18.52.

Passage of a mobile dislocation line through solid containing cavities (voids or helium bubbles) that intersect the glide plane is shown in Fig. 18.22(b). The only difference between the precipitate particles and the cavities as obstacles is that the bowed arcs of the dislocation line meet the surface of the cavity at right angles. The critical stress required to move the dislocation is identical to that derived for the coherent precipitate. Unlike the precipitate, no dislocation rings decorate the cavity after the process is complete. A more detailed account of void hardening is given by Coulomb.[8]

In addition to bowing and pinching off, a dislocation may be able to cut through a cavity as it does through a depleted zone.[9] If the dislocation is capable of cutting through the cavity, the structure of the dislocation and the void are the same after the event as before. Therefore, the interaction energy between these two objects as a function of their separation is symmetric about the overlapping position, instead of having the shape shown in Fig. 18.19(a) for dislocations cutting through depleted zones. Aside from this distinction, the stress required to force a dislocation through a void can be obtained by the method applied in Sec. 18.5 to analyze cutting of a depleted zone (see problem 18.3). If the maximum interaction energy between the dislocation and the void is U_0, the stress to cut through is

$$\sigma_s = \frac{U_0}{blR}$$

where R is the radius of the cavity. The interaction energy U_0 can be approximated as the elastic strain energy contained in the volume of solid equal to the cavity volume and centered on the line. This strain energy is released when the cavity attaches to the line and must be supplied to separate the two. The elastic-energy density around a screw dislocation is given by Eq. 8.8. Instead of integrating this expression over the volume of a sphere centered on the

dislocation, we replace the sphere with a cylinder of radius R and length 2R. The total elastic energy contained in this volume (which is the void–dislocation interaction energy) is

$$U_0 = 2R \int_{r_d}^{R} 2\pi r E_{el} \, dr = \frac{RGb^2}{2\pi} \ln\left(\frac{R}{r_d}\right)$$

Combining the preceding two formulas gives the stress required for a dislocation to cut through a void or bubble:

$$\sigma_s = \frac{Gb \ln(R/r_d)}{1 \quad 2\pi} \qquad (18.53)$$

which differs from the Orowan stress (Eq. 18.52) by a factor of $\ln(R/r_d)/4\pi$. It appears that it should be easier for dislocations to cut rather than bypass small cavities, but the stress requirements for the two mechanisms are so close and the analyses so approximate that use of the Orowan stress is the more prudent approach.

18.7 LOOP HARDENING

The dislocation loops formed by condensation of irradiation-produced interstitial atoms are either of the pure-edge type if the loop is faulted or of mixed-edge and screw character if the loop is unfaulted. If the glide plane of a mobile dislocation passes close to or intersects a loop, dislocations on the plane will experience a resistance to motion. To exert a significant retarding force on the mobile dislocation, the center of the loop must lie close to the glide plane (say within a loop diameter). Since the loop diameter is generally much less than the distance between loops on the slip plane, each loop is viewed as exerting a force on the dislocation line only at the point at which contact is made. The applied shear stress needed to overcome the loop resistance corresponds to the maximum force, F_{max}, between the loop and the dislocation line. If the spacing of the loops on the glide plane is l, the retarding force per unit length experienced by the line is F_{max}/l. The oppositely directed force on the line due to the applied shear stress is $\sigma_s b_e$, where b_e is the Burgers vector of the mobile dislocation. If all loops exerted the same maximum force on the mobile dislocations in the solid, a sharp yield point would be expected when $\sigma_s b_e$ equalled or exceeded F_{max}/l. More precisely, the increase in the yield stress of the metal due to the presence of the loops (loop hardening) is given by

$$\sigma_s = \frac{F_{max}}{b_e l} \qquad (18.54)$$

The calculation of σ_s can be performed in two steps:

1. Calculation of F_{max}, which characterizes the interaction of a single loop and the dislocation line.

2. Calculation of the distance l between loop intersections with the glide plane.

Calculation of F_{max} is of necessity approximate owing to the large number of orientations of a circular loop with respect to a particular glide plane and the different possible Burgers vectors of both the loop and the mobile dislocation. Since the loop is a circular dislocation, classical elasticity theory is often used to describe the loop–dislocation-line interaction. This procedure, however, is of dubious validity when the line actually cuts the loop. Calculation of the purely elastic interaction between a straight, rigid dislocation line that passes near to, but does not intersect, an immobile circular loop is presented in this section as an example of the type of analysis needed to provide F_{max}. The results for intersecting loops and lines are of the same general form as those obtained from long-range elastic interactions.

Figure 18.23 shows a long, straight edge dislocation whose slip plane lies a distance y from the plane of a circular loop of pure-edge character. We wish to compute the force F_x between the two entities as a function of the distance x. To do so, we first calculate the work required to grow the loop from zero size to radius R_1. We then differentiate this work with respect to x to obtain F_x. Calculations of this sort have been performed for a variety of loop/line combinations.[10]
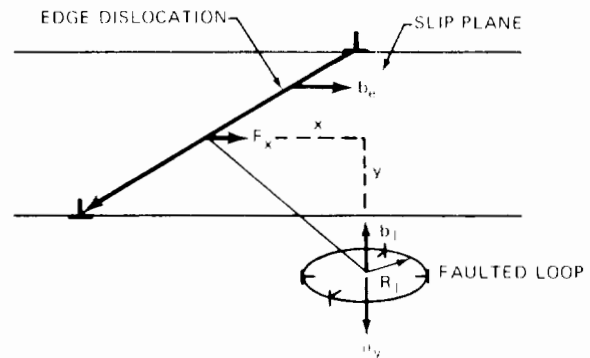

Fig. 18.23 Straight-edge dislocation passing by a faulted dislocation loop. The slip plane of the dislocation is parallel to the plane containing the stacking fault of the loop.

The stress field in the solid adjacent to a straight edge dislocation consists of a shear component and normal components σ_x, σ_y, and σ_z. The shear component acts in the plane of the loop shown in Fig. 18.23 but in a direction perpendicular to the Burgers vector b_1 of the loop. Hence, this stress component exerts no force on the loop (i.e., the b component in the first term of Eq. 8.13 is zero). Similarly, the normal stress components σ_x and σ_z do not exert forces on the loop which act to retard its growth. The normal stress σ_y, on the other hand, tends to pull apart or push together the stacking fault, which is surrounded by the loop. Therefore, this stress component exerts a radial force on the loop. Figure 8.10(b) is equivalent to the situation depicted in Fig. 18.23. The total force on the loop due to the stress component σ_y is $(2\pi R_1)\sigma_y b_1$. The work done as the loop expands from R_1 to $R_1 + dR_1$ is

$$dW = (2\pi R_1)\sigma_y b_1 \, dR_1$$

or the total work for the loop to expand against the stress from the nearby straight edge dislocation is

$$W = \pi R_1^2 \sigma_y b_1 \qquad (18.55)$$

The stress σ_y is

$$\sigma_y = \frac{Gb_e}{2\pi(1-\nu)} \frac{y(x^2-y^2)}{(x^2+y^2)^2} \qquad (18.56)$$

Equation 18.56 was obtained from the stress components in cylindrical components shown in Fig. 8.8 in the manner indicated at the beginning of Sec. 8.6 for obtaining other components in Cartesian coordinates. Inserting Eq. 18.56 into Eq. 18.55 and taking the derivative of W with respect to x yields

$$F_x = -\frac{\partial W}{\partial x} = -\frac{Gb_e b_l R_l^2}{1-\nu} \frac{xy(3y^2-x^2)}{(x^2+y^2)^3} \qquad (18.57)$$

In deriving Eq. 18.55, we have assumed that the stress σ_y does not vary appreciably over the area of the loop. This simplification is acceptable only when the line is far from the loop (i.e., $x^2 + y^2 \gg R_l^2$). For close approach of the line to the loop, the variation of σ_y over the loop area must be taken into account, and the F_x formula is considerably more complicated than Eq. 18.57. The results of the complete calculation for $y = R_l$ and $y = 0.1R_l$ are shown in Fig. 18.24. The maximum force occurs at $x \simeq R_l$ and increases as y decreases. For $y > R_l$ the approximate treatment discussed above gives the maximum force as

$$(F_x)_{max} = F_{max} = \frac{\alpha Gb_e b_l}{2(1-\nu)}\left(\frac{R_l}{y}\right)^2 \qquad (18.58)$$

where the numerical coefficient α (which is of order unity) depends on the relative orientations and the Burgers vector of the loop and the dislocation line. Averaging over all orientations and Burgers vector combinations, Kroupa and Hirsch[11] find that the average of the maximum forces due
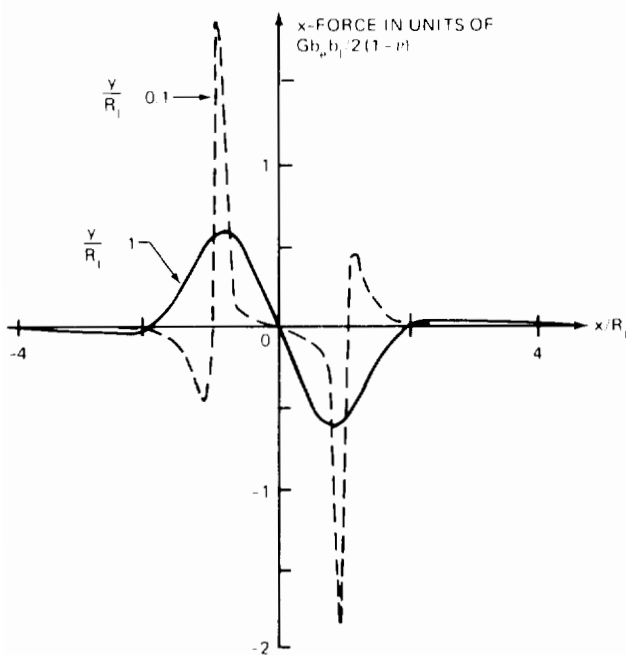
to loops distributed uniformly in a slab of thickness $2R_l$ about the slip plane is

$$F_{max} \simeq \frac{1}{8} Gb_e b_l \qquad (18.59)$$

Interaction forces due to loops outside of this slab are negligible because of the y^{-2} dependence of F_{max} (Eq. 18.58). Using Eq. 18.59 in 18.54 shows that the hardening effect of the loops is

$$\sigma_s = \frac{Gb_l}{8l} \qquad (18.60)$$

Foreman[12] has performed computer calculations of loop hardening in which the elastic interaction forces of the model presented above are neglected. Instead, the critical stress for tearing the line away from the loop is based on the stability of the junctions formed when the loop and the line intersect. In the calculations a shear stress drives a dislocation line into a solid containing an array of loops of specified size and spacing. At stresses below the value needed to move the line entirely through the array of loops, the dislocation reaches an equilibrium position. As the stress is increased in small steps, the line moves forward to new equilibrium positions. Figure 18.25 shows the equilibrium configurations of a dislocation line (initially of pure screw character) in a cloud of loops whose diameter is $\frac{1}{10}$

Fig. 18.24 The x-force on the dislocation line for the orientation of Fig. 18.23. (From Ref. 11.)
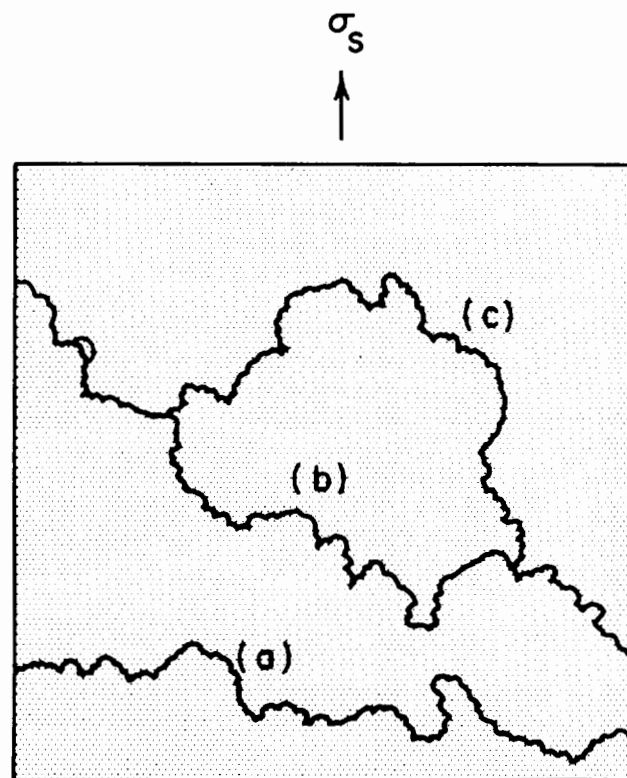

Fig. 18.25 Three stages of the movement of a dislocation (initially screw) upward through an array of loops. The applied stresses corresponding to each position are (a) 0.544 Gb/l. (b) 0.550 Gb/l; and (c) 0.556 Gb/l. (From Ref. 12.)

of the loop spacing in the glide plane. Each dot on the drawing corresponds to a loop cutting the glide plane of the dislocation. The three positions of the line correspond to three different values of the applied shear stress, which acts upward in the diagram. When the applied stress exceeds the value corresponding to the equilibrium position (c), the array of loops can no longer prevent motion of the dislocation. That is, the array of loops exhibits a well-defined yield point at a certain critical stress. When averaged over all dislocation and loop orientations, Foreman's computer simulation gives a critical stress of

$$\sigma_s = \frac{Gb}{4l} \qquad (18.61)$$

Foreman's results differ from those of Kroupa and Hirsch (Eq. 18.60) not only in the numerical factor in the denominator but in the interpretation of the spacing l as well. In Foreman's analysis l is given by Eq. 18.25. In Kroupa and Hirsch's analysis, l is larger than this value because of zigzagging of the dislocation through the array of loops. This difference further increases the discrepancy between Eqs. 18.60 and 18.61. The bulk of experimental evidence on loop hardening favors relations of the type of Eq. 18.61 with l given by Eq. 18.25:

$$\sigma_s = \frac{Gb(2R_l N_l)^{1/2}}{\beta} \qquad (18.62)$$

where N_l is the concentration of loops in the solid and β is a numerical factor between 2 and 4. With either of these constants, the increased strength due to loops is only ~20% of the full Orowan stress (Eq. 18.53) which results from an array of impenetrable obstacles.

18.8 TENSILE PROPERTIES OF IRRADIATED AUSTENITIC STAINLESS STEEL

Two features dominate the effects of fast-neutron irradiation on the austenitic stainless-steels—hardening, or an increase in the stress needed to initiate plastic deformation (the yield stress, the proportional elastic limit, or the flow stress), and embrittlement, or the reduction in specimen elongation prior to fracture.

18.8.1 Radiation Hardening

The strengthening effect of fast-neutron irradiation depends on the fluence and the temperature (both irradiation and test temperatures). High temperatures act to remove damage inflicted by fast-neutron collisions with lattice atoms. During irradiation, creation and thermal annealing of defects proceed simultaneously. During testing at sufficiently high temperatures, only thermal annealing continues, and this process tends to mitigate the hardening effect of the neutron irradiation. Damage effects can be roughly classified by regions of fluence and temperature. The fluence regions above and below ~10^{21} neutrons/cm^2 (fast) correspond approximately to the dosages received by in-core structural components in fast and thermal reactors, respectively.

18.8.2 Low Fluence

In this regime ($\Phi t < 10^{21}$ neutrons/cm^2), the primary form of radiation damage consists of the depleted zones described in Sec. 18.5. Because of the low fluence, sizable quantities of dislocation loops and voids have not formed. Temperature subdivisions in the low-fluence regime are approximately divided by one-half the melting point in degrees Kelvin, which for stainless steel is 550 to 600°C. (The melting point of steel is 1650 to 1700°K.) For $T < T_m/2$, sufficient displacement damage survives annealing during irradiation and testing to cause an increase in the yield strength of the steel. This form of hardening decreases with test temperature according to Eq. 18.38. A typical stress–strain curve following a low-temperature low-fluence irradiation is shown at the top of Fig. 18.15(a). At temperatures greater than $T_m/2$, the depleted zones and embryonic interstitial loops anneal so rapidly during irradiation and/or testing that no hardening is observed in tensile tests. The stress–strain curve coincides with that of the unirradiated material [lower curve of Fig. 18.15(a)].

18.8.3 High Fluence

At high fast-neutron fluences ($\Phi t > 10^{21}$ neutrons/cm^2), dislocation loops and voids grow to large sizes. These large defects require appreciable time to anneal out even in elevated-temperature mechanical tests; so their effect on mechanical properties persists to higher temperatures than does the effect of the depleted zones. Complete recovery of the radiation hardening does not take place until temperatures in excess of 800°C (~$2T_m/3$). Figure 18.26 shows the postirradiation yield stress of type 304 stainless steel as a function of the test temperature. The specimens were irradiated at a temperature equal to one-half the melting point in a fast fluence in excess of 10^{22} neutrons/cm^2. At testing temperatures up to about 400°C, the hardening is due to a combination of depleted zones, dislocation loops, and voids. The displacement damage (i.e., hardening due to the depleted zones) becomes negligible at about 400°C owing both to thermally activated cutting of the zones by mobile dislocations and to removal of depleted zones by thermal annealing during the test. Between 400 and 550°C,
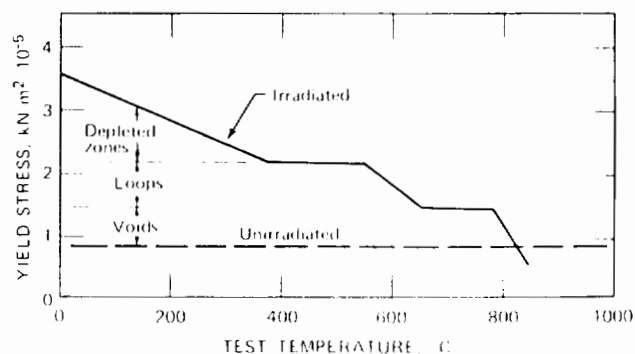

Fig. 18.26 Yield strength of type 304 stainless steel before and after irradiation at $T \sim T_m/2$ to a fluence of 1.7×10^{22} neutrons/cm^2. [After J. J. Holmes et al., *Acta Met.*, 16: 955 (1968).]

the hardening is temperature independent (athermal). At temperatures between 550 and 650°C, the loops are either unfaulted or annealed out during the test. Radiation hardening diminishes until at 650°C only hardening due to voids remains. The voids are not completely eliminated until temperatures above 800°C. The rather distinct regions of radiation hardening determined by tensile testing correspond to electron-microscope evidence of depleted zones (black dots), loops, or voids in the microstructure of the specimens. The measured hardening due to loops and voids shown in Fig. 18.26 is somewhat lower than the values predicted by the theories outlined in the previous section, although the athermal nature of strengthening due to these defects is in agreement with theoretical expectations. The discrepancy in the magnitudes of the experimental and predicted hardening can be due to undercounting the concentration of defects from electron micrographs, which do not reveal defects less than a few tens of angstroms in diameter. With Eq. 18.25 the defect concentration can be used to determine the obstacle spacing on the glide plane. This latter quantity enters the void-hardening expression (Eq. 18.53) and the loop-hardening formulas (Eqs. 18.61 and 18.62).

The only radiation-produced defects that can be seen in the electron microscope for $T > 800°C$ are helium bubbles, and these are not numerous enough to cause appreciable hardening. They do, however, dramatically reduce ductility at temperatures up to the melting point.

18.8.4 Plastic Instability

The sizable increase in the yield strength of austenitic stainless steel resulting from low-temperature irradiation is not matched by a corresponding increase in the ultimate tensile strength of the metal. Figure 18.15 shows that the percentage increase in the yield strength is much larger than the percentage increase in the ultimate tensile strength (which is the stress at the maximum of the engineering stress—strain curve). The radiation-produced defects are more effective in impeding the motion of dislocations than they are in preventing the theoretical fracture stress from being exceeded in the specimen. The former ability is responsible for the large yield strength increase, and the latter function accounts for the modest increase in ultimate strength. Thus, the net effect of radiation is to decrease the difference between the ultimate and yield strengths of the steel, or to decrease the work-hardening rate, $d\sigma/d\epsilon$.

Work hardening of an unirradiated metal arises from the creation of obstacles to dislocation motion as mobile dislocations become tangled with each other and with the preexisting dislocation network of the solid. In an irradiated metal there are already so many radiation-produced obstacles to dislocation motion that the additional hardening effect of dislocation tangling (normal work hardening) is a small increment to the frictional stress.

According to Eq. 18.7, when the work-hardening rate $d\sigma/d\epsilon$ is reduced, the stress at which necking or plastic instability occurs is correspondingly lowered. If the stress for necking is lower, so is the strain at this point. Therefore, the reduction in ductility which occurs in conjunction with hardening (i.e., at low temperatures) is simply a consequence of the early onset of plastic instability.

18.8.5 Dislocation Channeling

In some highly irradiated metals, the onset of necking can coincide with yielding. That is, there may be no uniform elongation at all during a tensile test. An example of the stress—strain curve for a specimen exhibiting this sort of instability is shown as the upper curve in Fig. 18.15(b). This unusual macroscopic behavior during deformation is believed to be associated with the microscopic phenomenon of dislocation channeling.[13] In this process defects impeding dislocation motion in a metal are destroyed as the dislocation moves through them. Succeeding mobile dislocations therefore experience a smaller resistance to motion than their predecessors and thus move along the partially denuded glide plane more easily than the dislocations that first cleared the way. The stress required to move dislocations over slip planes that have been cleared of radiation-produced obstacles is far lower than the stress required to start the first dislocation moving. Thus an avalanche of dislocations can be released along the planar channels that have been cleared of obstacles. The strain due to this type of dislocation motion is highly localized. A group of closely spaced parallel slip planes that have been stripped of defects by moving dislocations is called a dislocation channel. Dislocations continue to be generated in and move along a cleared channel until normal work-hardening processes (intersection of glide dislocations with the dislocation network of the metal) increase the stresses required to maintain dislocation motion. Many channels can become activated during deformation. Evidence of deformation by dislocation channeling is seen in Fig. 18.27. The dark bands, which are called slip traces, represent
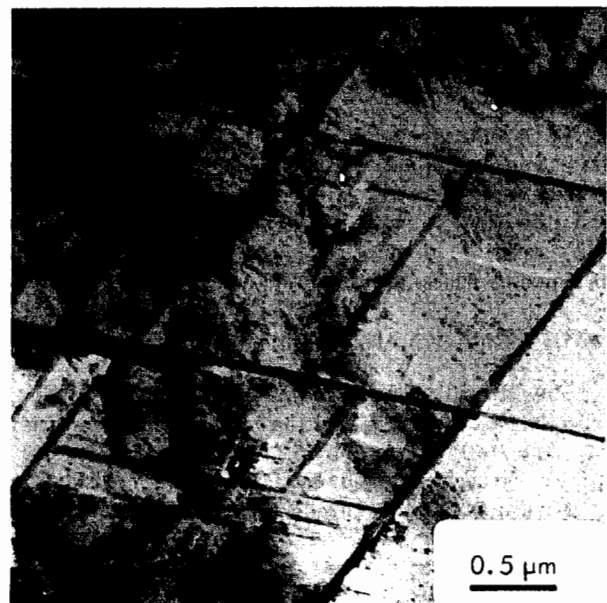

0.5 µm

Fig. 18.27 Type 304 stainless steel deformed 10% after irradiation at 121°C. The slip traces (dark bands) represent the intersection of $\{111\}$ planes with the surface of the specimen. [From E. E. Bloom et al., *J. Nucl. Mater.*, 22: 68 (1967).]
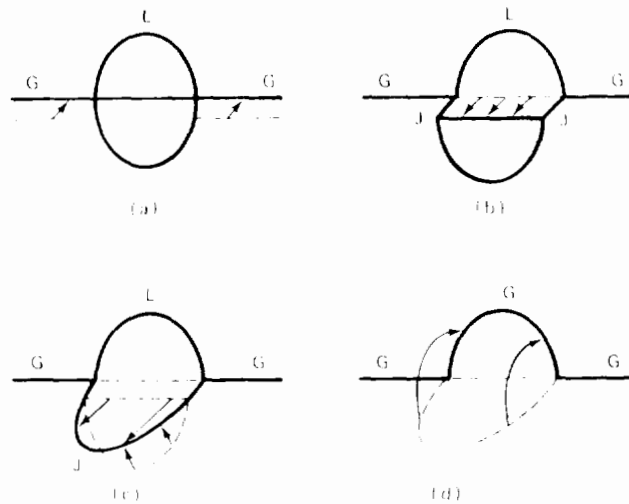
Fig. 18.28 A mechanism of loop destruction by a moving dislocation. The glide dislocation G cuts (a) into the loop L to form stable junctions J at the points of interaction (b). Glide of both parts of the loop causes the junctions to lengthen until they join at J' in (c) to extend around half the loop. The two halves of the loop then glide together (d) along their glide cylinders owing to mutual attraction and coalesce. [After A. J. E. Foreman and J. V. Sharp, *Phil. Mag.*, 19: 931 (1969).]

dislocation channels where large localized deformation has occurred. The material between the slip bands is not deformed. Each of the slip bands in the photograph corresponds to the intersection of a group of (111) planes with the surface. The {111} planes are the preferred glide planes in the fcc structure [Fig. 8.2(a)].

The radiation-produced defect most likely destroyed by moving glide dislocations is the dislocation loop. Figure 18.28 shows how an immobile loop can be transformed into a part of the moving dislocation as a result of the intersection of these two species. After passage of the glide dislocation, the loop completely disappears. Other models of loop destruction by moving dislocations involve chopping the loop into smaller bits, some of which can be incorporated into the moving dislocation.

18.9 CREEP RUPTURE

Creep rupture refers to the failure of a specimen that has been subject to stresses well below the yield stress for long periods of time. Deformation of the metal occurs by creep rather than by the nearly instantaneous plastic deformation characteristic of a tensile test. Creep-rupture tests can be conducted either in equipment similar to that employed for tensile tests or by tube-burst tests, in which a closed tubular specimen is loaded by internal gas pressure. In both types of tests, the time to failure, or the *rupture life*, t_R, and the *elongation at failure*, ϵ_F, are measured. Provided that steady-state creep prevails for the major portion of the test, these two quantities are related to the creep rate by Eq. 18.20. The creep-rupture properties depend on the extent of irradiation, the irradiation and testing temperatures, and on the degree of cold work of the specimens. These variables directly control the creep rate, $\dot{\epsilon}$, and the elongation at fracture, ϵ_F. The rupture life, t_R, is

indirectly affected by the same variables because it is the ratio of ϵ_F to $\dot{\epsilon}$.

Figure 18.29 shows typical results of large fast-neutron fluences on the creep-rupture properties of an austenitic stainless steel. In this particular set of experiments, the specimens were annealed (i.e., not cold worked), and the neutron exposure, testing temperature, and the applied stress were fixed. Only the irradiation temperature was varied. The data indicate that the creep rate, $\dot{\epsilon}$, is lower in the irradiated specimens than in the unirradiated metal. The reduction is greatest at the lowest irradiation temperature. This trend is consistent with the effect of temperature on the tensile strength of irradiated steel (see previous section). The decreased creep rate is attributed to the depleted zones, Frank loops, and voids produced by the fast-neutron bombardment, all of which impede the motion of dislocations through the solid. As the irradiation temperature is raised, these obstacles to dislocation motion are progressively removed from the specimen by annealing, and the creep rate increases. At 780°C the creep rate is practically equal to that of the unirradiated material.

Not all investigations have confirmed the observation of reduced steady-state creep rate in neutron-irradiated steel. The opposite effect, occasionally found, is attributed to the removal of atomically dispersed carbon from the matrix by the formation of large carbide particles ($M_{23}C_6$) by the process of radiation-induced precipitation. The dissolved carbon apparently acts as a stronger barrier to dislocation motion than the larger but more widely spaced carbide particles.

Figure 18.29 also demonstrates that radiation reduces the elongation to fracture. As in the case of the creep rate, the strain at rupture is smallest for the specimen irradiated at the lowest temperature. This reduction in ϵ_F is most probably due to the loss of work hardenability accompany-
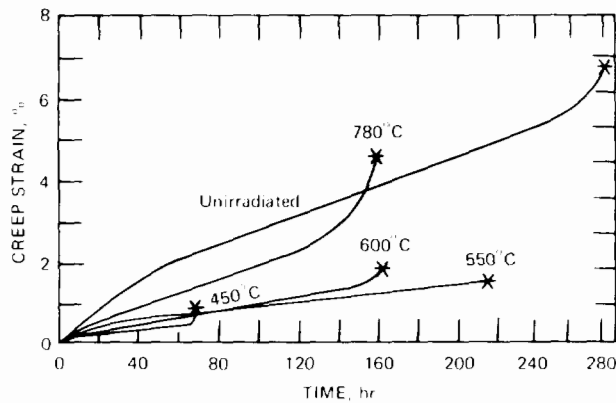
Fig. 18.29 Effect of irradiation temperature on the creep rupture of annealed type 304 stainless steel irradiated to 1.9×10^{22} neutrons/cm² (> 0.1 MeV) and tested at 550°C under a stress of 3×10^5 kN/m². [After E. E. Bloom and J. R. Weir, Jr., *Nucl. Technol.*, 16: 45 (1972).]

ing the radiation strengthening of the metal and leads to premature plastic instability (see Sec. 18.9). As the irradiation temperature is increased, the elongation to fracture begins to return to the value characteristic of the unirradiated material. Work hardenability is recovered as the radiation-induced increase in yield strength is removed by thermal annealing. However, even at 780°C, where radiation strengthening should have completely annealed out, the creep test shows a significant loss in ductility. In fact, as the irradiation temperature is increased to values greater than those shown on Fig. 18.29, the elongation to fracture again decreases. This high-temperature loss of ductility is associated with the helium produced by (n,α) reactions in the metal (see following section).

The effect of fast-neutron fluence on the elongation to fracture with all other variables held fixed is shown in Fig. 18.30. The ductility (strain at fracture) is reduced from a value of ~20% for the unirradiated material to ~0.1% at fluences expected in LMFBR service. For this particular set of conditions, radiation causes a 200% reduction in the ductility of the specimen.

The combined effects of fluence and temperature on the creep-rupture properties can also be demonstrated by rupture life graphs of the type shown in Fig. 18.12, which illustrated that, for unirradiated steel, increasing the test temperature markedly reduced the rupture life. This effect is a manifestation of the rapid increase in the steady-state creep rate, $\dot{\epsilon}$, with test temperature (i.e., in an Arrhenius fashion, Eq. 8.46). Figure 18.31 shows that at fixed stress and fixed test temperature radiation reduces the rupture life, often by as much as an order of magnitude. Reduction of t_R is due predominantly to the severe loss in ductility induced by radiation. The effect of test temperature (which should not be confused with the influence of the irradiation temperature indicated by Fig. 18.29) is similar to that found in unirradiated specimens (Fig. 18.12).

The effect of neutron fluence on t_R is exhibited in Fig. 18.32. The rupture life decreases drastically with increased fluence primarily because of the loss in ductility illustrated by Fig. 18.30.
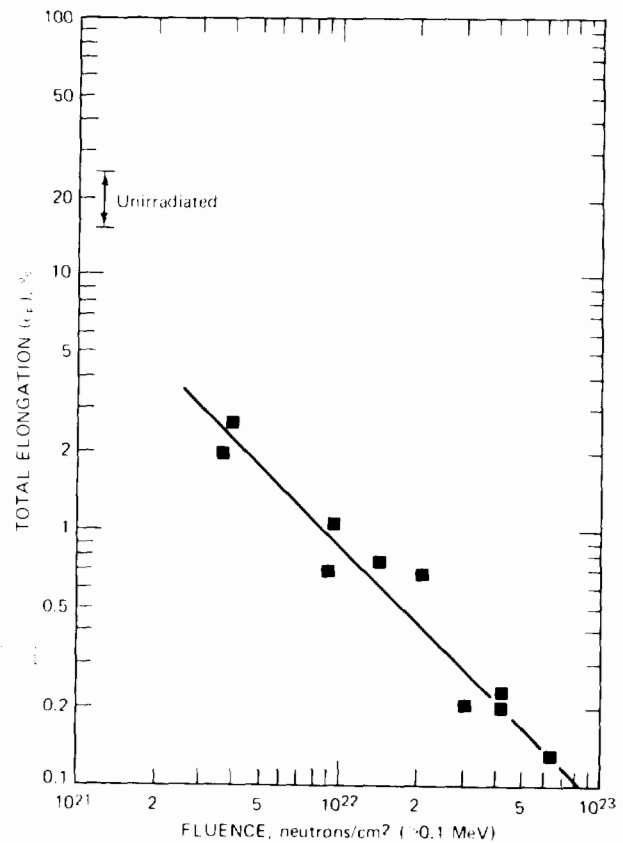

Fig. 18.30 Postirradiation ductility of type 304 stainless steel irradiated at various temperatures between 370 and 470°C and tested at 600°C and 1.9×10^5 kN/m². (After E. E. Bloom and J. O. Stiegler, in ASTM Special Technical Publication 484, p. 451, American Society for Testing and Materials, Philadelphia, 1970.)
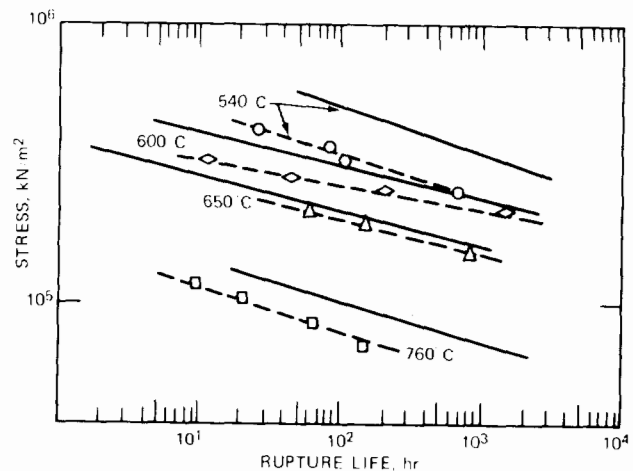

Fig. 18.31 Rupture life of type 316 stainless steel irradiated to a total neutron fluence of 1.2×10^{22} neutrons/cm² at an irradiation temperature of 440°C. Tested at various temperatures in uniaxial tension. ——, unirradiated.- - -, irradiated. (After A. J. Lovell and R. W. Barker, in ASTM Special Technical Publication 484, p. 468, American Society for Testing and Materials, Philadelphia, 1970.)
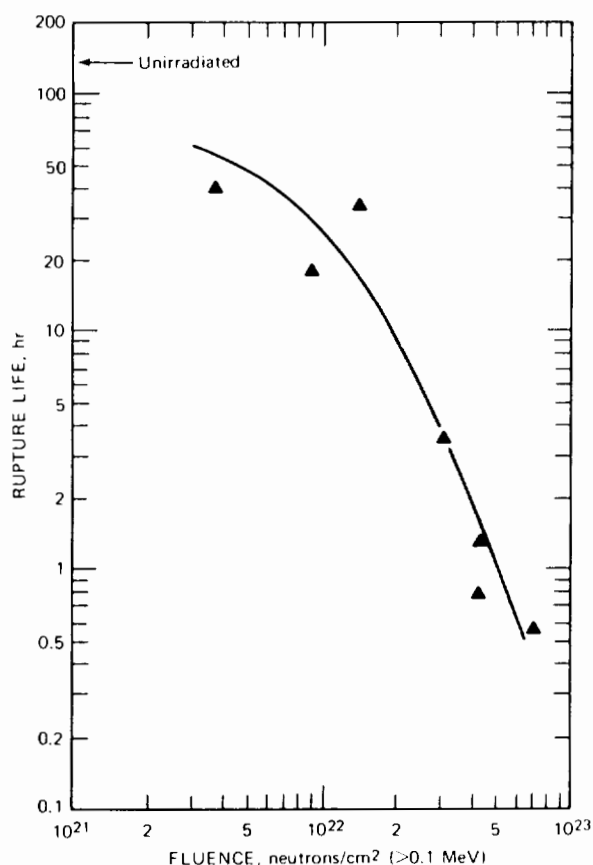
Fig. 18.32 Effect of neutron fluence on the postirradiation rupture life of type 304 stainless steel. The irradiation temperatures were between 370 and 430°C. The tests were performed at 600°C at a stress of 1.9×10^5 kN/m². (After E. E. Bloom and J. O. Steigler, ASTM Special Technical Publication 484, p. 451, American Society for Testing and Materials, Philadelphia, 1970.)

The degree of cold work of the tubing used in the fuel elements is a controllable fabrication variable that can be used to optimize the in-pile performance of the cladding. Cold working is measured by the percentage reduction in cross-sectional area resulting from drawing the tubing at room temperature. Microstructurally, the degree of cold work appears as a higher dislocation density than in the annealed metal. Cold working increases the strength of the metal by mechanisms similar to those responsible for radiation hardening, but, in common with this phenomenon, the effects of cold work diminish greatly at elevated temperatures owing to the removal of the mechanically produced dislocation tangles by thermal processes (recovery). The effect of cold work on the stress rupture properties of stainless steel is shown in Fig. 18.33. Moderate cold working (10 to 30%) enhances the short-term stress rupture strength, but the long-term strength eventually becomes poorer than that of the fully annealed material. If a long rupture life at low stress was the sole criterion for choosing a cladding material, the fully annealed metal would be superior to all grades of cold-worked metal. However, the principal value of cold working of the

cladding is that void formation and swelling are suppressed (see Chap. 19). Consequently, a 10% cold-worked material appears to represent the best compromise between improvement of swelling resistance at the expense of some degradation of the creep rupture properties.

18.9.1 High-Temperature Fracture

The nature of the fractures that terminate the high-temperature creep process is quite different from the mode of fracture exhibited by metals and alloys following tensile tests at low temperatures. At low temperatures fracture tends to result from shearing through grains of the metal (i.e., the transgranular mode) and often occurs only after appreciable deformation. The fracture mode that terminates the third stage of high-temperature creep or the deformation in a high-temperature tensile test is usually of the intergranular type. In addition, high-temperature fracture is often accompanied by the observation of minute cracks or cavities in the metal adjacent to the fracture surface.

The nature of the metal after fracture in a relatively high-stress tensile test is shown in Fig. 18.34. In the unirradiated specimen [Fig. 18.34(a)], the metal in the vicinity of the fracture is full of wedge-shaped cracks. The actual fracture surface probably followed grain boundaries along a path that had a high density of such cracks. The grains are deformed in the direction of the applied stress. In the irradiated specimen [Fig. 18.34(b)], the small internal
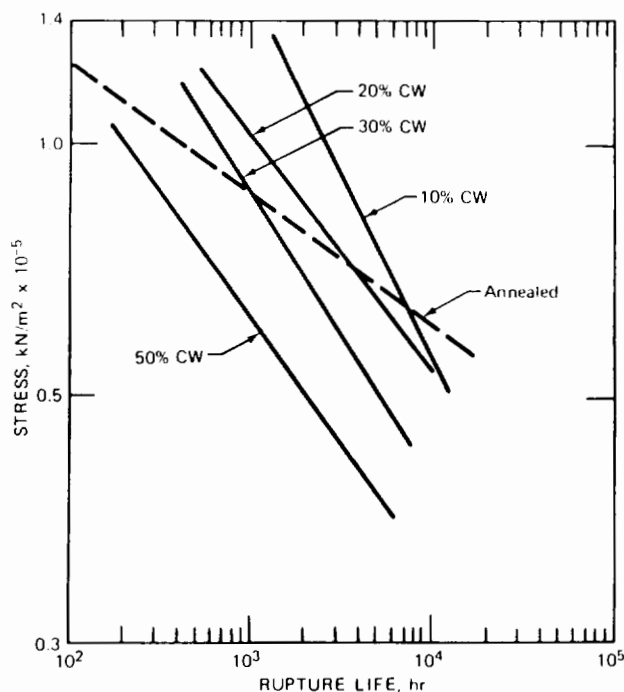

Fig. 18.33 The effect of cold working on the rupture life of type 316 stainless steel. Tested at 700°C. (From T. Lauritzen, Stress-Rupture Behavior of Austenitic Steel Tubing. Influence of Cold Work and Effect of Surface Defects, USAEC Report GEAP-13897, General Electric Company, 1972.)
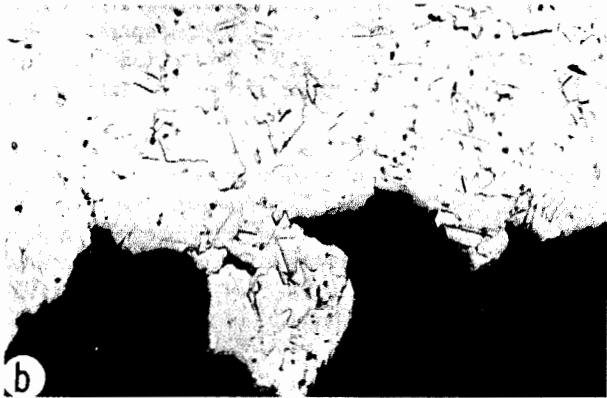
Fig. 18.34 Fractures of type 347 stainless steel after a tensile test at 600°C. (a) Unirradiated, $\epsilon_F = 18\%$. (b) Irradiated to a fast fluence of 2×10^{22} neutrons/cm^2, $\epsilon_F = 3\%$. (From M. Kangilaski et al., ASTM Special Technical Publication 457, p. 67, American Society for Testing and Materials, Philadelphia, 1969.)

are created, fracture of the unirradiated metal is a result of the slow growth of cracks or cavities by grain-boundary sliding diffusional processes.

18.9.2 Wedge Cracks

The high-temperature fracture process can be divided into nucleation and growth regimes. Small wedge cracks are spontaneously formed at grain-boundary triple points when

(a)

(b)

Fig. 18.35 Fractures of type 347 stainless steel after a stress-rupture test at 650°C. (a) Unirradiated; stress = 2.4×10^5 kN/m^2; t_R = 32 hr; ϵ_F = 23%. (b) Irradiated to a fluence of 2×10^{22} neutrons/cm^2; stress = 2×10^5 kN/m^2; t_R = 21 hr; ϵ_F = 0.2%. [From M. Kangilaski et al., Trans. Amer. Nucl. Soc., 12: 574 (1969).]
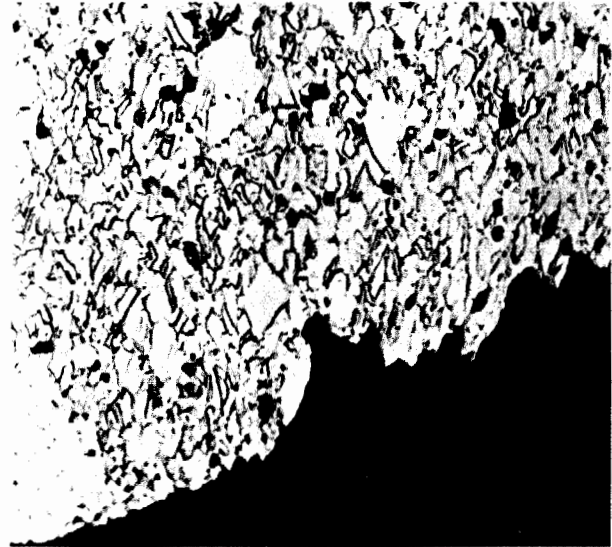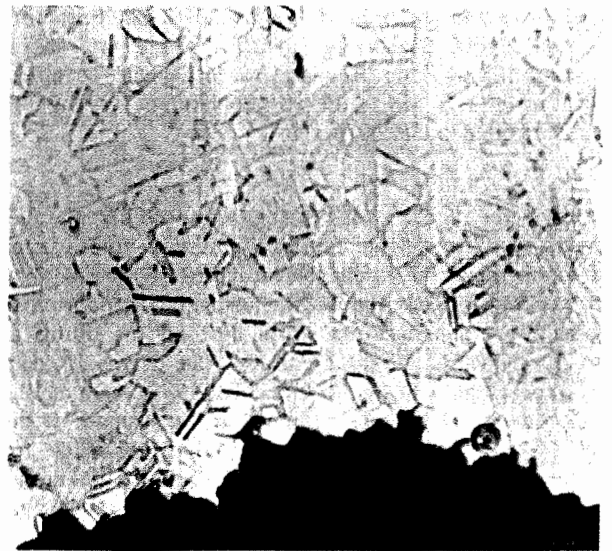
cracks are absent, and the grains do not appear to have been deformed.

Figure 18.35 shows similar photomicrographs of the fracture surface produced in a creep-rupture test. The metal near the fracture in the unirradiated specimen contains many small cavities on the grain boundaries rather than the wedge-shaped cracks that appeared in the high-stress tensile fracture [Fig. 18.34(a)]. Grain deformation perpendicular to the fracture surface is evident in the failed unirradiated specimen. The general appearance of the fracture surface following the creep-rupture test of neutron-irradiated steel [Fig. 18.35(b)] is practically indistinguishable from that observed after a tensile test [Fig. 18.34(b)]. In both cases, intergranular cracking apparently occurred rapidly as soon as a few grain-boundary cracks or cavities were formed. The absence of internal cracks or cavities near the crack surface and the lack of grain deformation are both due to the radiation hardening of the matrix of the grains, which forces failure in a nearly brittle manner along grain boundaries. In contrast to the rapid failure of irradiated specimens as soon as a small number of cracks or cavities

the applied stress exceeds a critical value. Stroh[14] calculated the critical stress for the nucleation of wedge cracks on the assumption that dislocation pileups in a slip band provided the necessary stress concentration. Figure 18.36 shows a grain containing a dislocation source that has emitted dislocations into a slip plane under the action of the applied shear stress σ_{xy}. The dislocations are stopped by a grain boundary, and a pileup ensues. As noted in Sec. 8.6, the pileup develops a tensile stress σ that tends to open up a crack at the head of the slip band. The tensile
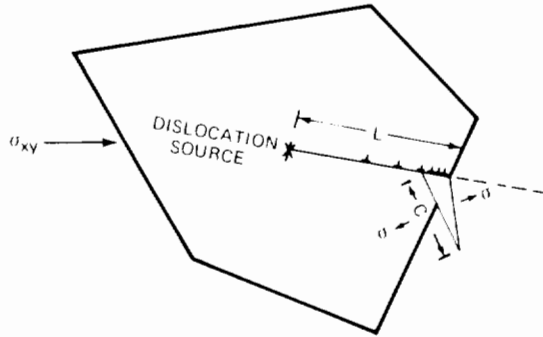

Fig. 18.36 Crack nucleation by the pileup of dislocations against a grain boundary. (From Stroh, Ref. 14.)

stress is greatest at an angle of $70°$ to the slip plane containing the pileup; so the crack develops in the orientation shown in the drawing. The stress concentration is given by Eq. 8.41 in which the distance from the tip to the pileup is taken as the crack length, or

$$\sigma^2 C = L\sigma_{xy}^2 \qquad (18.63)$$

where C is the length of the crack and L is the length of the pileup. The stability of the crack is determined by the Griffith energy criterion, which balances the loss of elastic energy of the solid with the gain of surface energy of the crack. When the exact stress distribution in the vicinity of the crack is employed to compute the elastic-energy term, the work required to form the crack is

$$W = E_{tot} - E_{el}^{\circ} = -\frac{\pi(1 - \nu)C^2\sigma^2}{8G} + 2C\gamma \quad (18.64)$$

where E_{el}° is the elastic energy of the perfect solid and γ is the energy required to produce a unit area of crack surface.
Setting $dW/dC = 0$ yields

$$C\sigma^2 = \frac{8\gamma G}{\pi(1 - \nu)} < \frac{12\gamma G}{\pi} \qquad (18.65)$$

When the relationship between the elastic constants $[E = 2G(1 + \nu]$ is employed and the crack length is denoted by 2C instead of C, Eq. 18.65 is seen to be the fracture stress criterion of Griffith (Eq. 16.5). Cracks spontaneously nucleate when the applied shear stress σ_{xy} attains a value that renders the right-hand sides of Eqs. 18.63 and 18.65 equal, or

$$\sigma_{nucl} = \left(\frac{12\gamma G}{\pi L}\right)^{1/2} \qquad (18.66)$$

A method of estimating L and of accommodating Stroh's analysis to the observation that the wedge-shaped cracks almost always occur at grain corners (i.e., triple points, see Fig. 16.18) has been proposed by McLean.[15] He argues that the slip planes within the grains on which the pileups occur in Stroh's theory can be replaced by sliding grain boundaries. The cracks formed by this process are shown in Fig. 18.37. In applying Eq. 18.66 to the triple-point crack, we assume that L is the length of the sliding interface, which is approximately equal to the grain size.

When precipitates (e.g., helium bubbles or $M_{23}C_6$ particles) have collected on the grain boundary, sliding is impeded. Consequently, Weaver[16] suggests that the length L should be taken as the average distance between particles on the grain boundary.

If no plastic deformation occurs around the tip of the crack, γ in Eq. 18.66 is best approximated by the difference between the energy of two free surfaces which were formed and the one grain boundary which was eliminated at the time the crack appeared:

$$\gamma = \gamma_s - \frac{1}{2}\gamma_{gb} \qquad (18.67)$$

Modifiers of stainless steel (e.g., titanium) affect the creep-rupture properties by increasing the effective surface energy either by segregating on grain boundaries or by removing impurities such as oxygen and nitrogen from the grain boundaries.[17] In either case, one or the other of the terms on the right of Eq. 18.67 is altered.

When the grains of the metal are capable of deforming plastically, the stress concentration at the tip of the crack can be partially relieved by plastic flow. The net effect of grain deformation is to increase the energy required to form
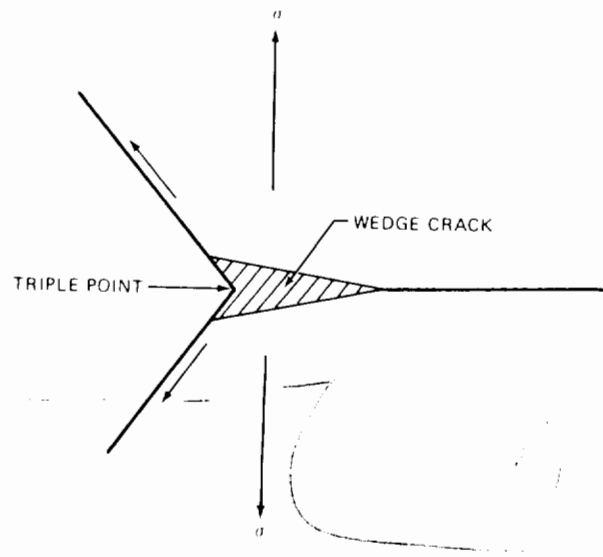

Fig. 18.37 A wedge crack forming on a grain-boundary triple point as a result of an applied stress normal to one of the boundaries.

a unit area of fresh crack surface, or to increase γ above the value predicted by Eq. 18.67. In fairly soft metals, crack nucleation occurs only at stresses that correspond to $\gamma \sim 100\gamma_s$. Thus, any process that strengthens the grains and prevents their deformation decreases the stress required to nucleate cracks and thus makes the metal less ductile. Matrix strengthening by irradiation-produced defects is probably one mechanism of the loss of ductility in neutron-bombarded steel.

The nucleation condition given by Eq. 18.66 is applicable only to small cracks. As the crack grows, contributions to the energy balance which depend on the crack width become important. Inclusion of these terms leads to a new critical stress for unstable crack growth and, for stresses below the critical value, to an equilibrium crack size. The width of the crack is assumed to be equal to the product of the number of dislocations in the pileup, n, and the width of each dislocation, which is approximately equal to the magnitude of the Burgers vector, b. That is, the crack is visualized as a condensation of n single dislocations into a superdislocation of Burgers vector nb.

The work per unit length required to form the crack is given by

$$W = -\frac{\pi(1-\nu)C^2\sigma^2}{8G} + 2C\gamma$$

$$+ \frac{G(nb)^2}{4\pi(1-\nu)}\ln\left(\frac{4\mathscr{R}}{C}\right) - \sigma V_c \quad (18.68)$$

The first two terms are contained in the energy balance for small cracks. They represent the elastic energy of the crack in the applied stress field and the surface energy of the crack. The third term is the elastic energy per unit length (i.e., the line tension) of the superdislocation. This quantity has been calculated for a single dislocation in Sec. 8.3. Equation 8.9 gives the energy per unit length of a screw dislocation of Burgers vector b, and the corresponding result for a single-edge dislocation is obtained by division by $1 - \nu$. With the crack modeled as an edge superdislocation, the Burgers vector is nb, and the core radius is replaced by $C/4$. The cutoff radius of the stress field of the superdislocation, $\mathscr{R}$, need not be known, because only the derivative of W with respect to C is needed.

The last term in Eq. 18.68 represents the work done by the applied stress in opening the crack to a finite volume V_c. The crack has the shape of a triangle of base nb and height C; so

$$V_c = \frac{1}{2}(nb)C \quad (18.69)$$

Equation 18.69 is substituted into Eq. 18.68, and dW/dC is set equal to zero, thereby yielding the following quadratic equation for the stable values of the crack length:

$$C^2 - B\left[1 - 2\left(\frac{A}{B}\right)^{\frac{1}{2}}\right]C + AB = 0 \quad (18.70)$$

where

$$A = \frac{G(nb)^2}{8\pi\gamma(1-\nu)} \quad (18.71)$$

$$B = \frac{8\gamma G}{\pi(1-\nu)\sigma^2} \quad (18.72)$$

Inspection of Eq. 18.70 shows that the roots C are real if $B > 16A$ and imaginary if $B < 16A$. If $B > 16A$, the smaller of the two roots represents the stable crack length, and, if $B < 16A$, the cracks are unstable and fracture occurs. The condition of neutral stability is given by $B = 16A$, or

$$\sigma(nb) = 2\gamma \quad (18.73)$$

The crack width nb in this formula is obtained from the theory of the dislocation pileup discussed in Sec. 8.6. In applying Eq. 8.39 to determine nb, we assume that the pileup length (i.e., the distance from the dislocation source to the crack) is approximately equal to one-half the grain size d. The crack growth criterion on which the preceding analysis was based assumed that the metal was subject to a tensile stress σ normal to the grain boundary in which cracks appeared. The dislocation pileup responsible for development of the crack, however, is produced by a shear stress along the slip band (or grain boundary in this case). The dislocations that move along the grain boundary and condense into the crack are impeded by the frictional stress σ_i due to obstacles in the matrix (Sec. 18.5). In estimating nb, the shear stress in Eq. 8.39 is reduced by this amount, and we have

$$nb = \frac{\pi(1-\nu)L(\sigma_{xy} - \sigma_i)}{G} \simeq (\sigma_{xy} - \sigma_i)\frac{d}{G} \quad (18.74)$$

where the length of the pileup has been taken as one-half the grain size.

Substituting Eq. 18.74 into 18.73 yields the critical tensile stress:

$$\sigma_{crit}(\sigma_{xy} - \sigma_i) = \frac{2G\gamma}{d} \quad (18.75)$$

In Fig. 18.37 the component of the applied stress that produces shear along the grain boundary σ_{xy} is approximately equal to $\sigma/2$. If, in addition, σ_i is small, the critical tensile stress for unstable triple-point crack growth given by Eq. 18.75 is very nearly equal to the critical shear stress for crack nucleation in Stroh's theory (Eq. 18.66). Because the internal stress σ_i is generally appreciable, σ_{crit} given by Eq. 18.75 is larger than the value given by Eq. 18.66, which means that fracture is controlled by crack growth rather than by crack nucleation. Thus, σ_{crit} of Eq. 18.75 represents the ultimate strength of a metal when failure occurs by the formation and extension of grain-boundary cracks.

The foregoing analysis of crack stability can be applied to estimate the elongation at fracture when failure is due to grain-boundary triple-point cracks. Elongation (or creep strain) of a grain occurs because n dislocations have traversed the grain and coalesced into a crack. Each of the n dislocations causes a displacement b; so the displacement due to a crack of width nb is equal to nb. The elongation, or fractional displacement, of the grain is nb/d. Equation 18.73 can be regarded as the condition giving the critical crack width (at which fracture occurs) for a specified applied stress. At the point of fracture, nb is the

product of the grain diameter and the elongation at fracture; elongation can be found from Eq. 18.73:

$$\epsilon_F = \frac{2\gamma}{\sigma d} \qquad (18.76)$$

Equation 18.76, which was first proposed by Williams,[18] has been applied to the embrittlement of neutron-irradiated Inconel (a nickel-based alloy).[19]

The prediction that grain refinement (i.e., reduction in d) reduces embrittlement is borne out by experiment. Equation 18.76 also predicts that ductility is improved by increasing the surface energy γ. This parameter is the energy required to form a unit area of fresh surface at the crack tip. If the metal is hard and brittle, γ approaches its minimum value given by Eq. 18.67. On the other hand, soft metals permit plastic flow at the crack tip, thereby requiring more energy to create fresh surface than just the surface energy. In this case, γ can be very much larger than γ_s. By hardening the matrix, irradiation acts to reduce the extent of plastic flow around the crack tip during creep, thereby decreasing γ. In general, any phenomenon that hardens the matrix of the grains without increasing the strength of the grain boundaries makes the metal more brittle.

The inverse dependence of ϵ_F on the applied stress indicated by Eq. 18.76 does not appear to have been verified experimentally.

18.9.3 Grain-Boundary Voids

Creep in metals at high temperature can be accompanied by the growth of voids (or cavities) lying on grain boundaries that are transverse to the applied tensile stress. These grain-boundary voids can grow at stresses well below the critical stress required for unstable growth of wedge cracks (Eq. 18.75).

The condition of mechanical equilibrium of a gas-free spherical cavity in a solid subject to tensile stress σ is given by Eq. 13.4 (in this relation, however, σ represents a compressive stress). A cavity will tend to grow if its radius is greater than the critical radius given by

$$\sigma = \frac{2\gamma}{R_{crit}} \qquad (18.77)$$

To describe creep rupture by growth of such voids, we must inquire as to the mechanism of the creation of void nuclei with radii large enough to satisfy the above stability criterion and then determine the rate at which these voids grow.

Voids are most easily nucleated on grain boundaries where stress concentrations occur. The triple-point wedge cracks shown in Fig. 18.37 can have equivalent radii large enough for the right-hand side of Eq. 18.77 to be smaller than the applied stress, even though the applied stress does not exceed the critical stress for wedge-crack growth. However, voids in creep specimens are observed all over the grain boundaries and not just at triple points. Defects in the grain boundary that can lead to void nucleation include precipitate particles or small ledges, both of which are effective stress concentrators.

Once nucleated, voids are believed to grow by absorbing vacancies from the bulk until they are large enough to interlink and cause fracture. Vacancies probably flow to the voids via the grain boundary since, at modest temperatures, grain-boundary diffusion is more rapid than lattice diffusion. The description of a quantitative model of the growth of grain-boundary voids under stress, proposed by Hull and Rimmer[20] and laundered by Speight and Harris,[21] follows.

Assume that N_{gb} voids of radius R_0 have been nucleated per unit area of grain boundary transverse to the tensile stress by one or a combination of the mechanisms listed in the preceding paragraph. The R_0 is assumed to be greater than R_{crit} of Eq. 18.77. Figure 18.38 shows such a void at some stage of the growth process when the radius has increased to R. The analysis neglects nucleation of new voids during growth of the batch nucleated at the time the
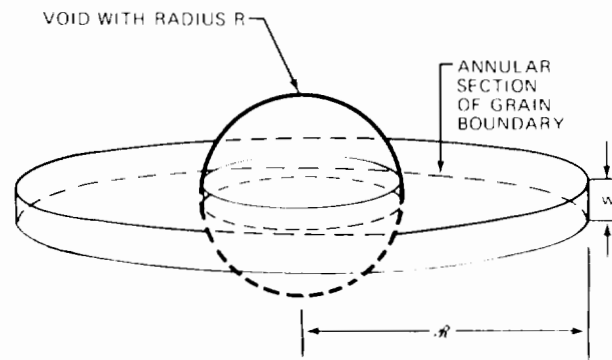

Fig. 18.38 A model for the growth of voids on grain boundaries during creep by diffusion of vacancies in the grain boundary.

tensile stress was applied. By analogy to the treatment of the three-dimensional growth of gas bubbles in the fuel (Chap. 13), the void population is divided into a series of identical unit cells, each with a central void surrounded by the associated grain-boundary area. The extent of grain boundary from which the void draws its vacancies is determined by

$$(\pi \mathscr{R}^2)N_{gb} = 1 \qquad (18.78)$$

Vacancies are assumed to be created at a uniform rate in the annular disk $R < r < \mathscr{R}$ surrounding each void. The thickness of the disk is taken to be the grain-boundary thickness, w. The vacancies created in the annulus diffuse to and are absorbed by the void at the center, causing the latter to grow. Because of the unit cell approximation embodied in Eq. 18.78, the void and its associated grain-boundary area are treated as an isolated entity; so the vacancy flux at $r = \mathscr{R}$ is zero. The vacancy-diffusion equation in the wheel-shaped region surrounding each void is

$$D_{vgb} \frac{1}{r} \frac{d}{dr}\left(r \frac{dC_v}{dr}\right) + G_v = 0 \qquad (18.79)$$

where D_{vgb} is the diffusion coefficient of vacancies in the grain boundary, C_v is the volumetric concentration of

vacancies, and G_v is the uniform volumetric source of vacancies in the diffusion zone. The vacancy concentration at the void surface* $(r = R)$ is given by Eq. 13.176 with $p = 0$:

$$C_v(R) = C_v^{eq} \exp\left(\frac{2\gamma}{R}\frac{\Omega}{kT}\right) \qquad (18.80)$$

which means that because of surface tension the solid in the vicinity of the void surface is placed in traction, thereby increasing the equilibrium vacancy concentration above the value in the stress-free solid. The boundary condition at $r = \mathscr{R}$ is

$$\left(\frac{dC_v}{dR}\right)_{\mathscr{R}} = 0 \qquad (18.81)$$

The solution of Eq. 18.79 with the above boundary conditions is

$$C_v(r) = C_v^{eq} \exp\left(\frac{2\gamma}{R}\frac{\Omega}{kT}\right) + \frac{G_v \mathscr{R}^2}{2D_{vgb}}\left[\ln\left(\frac{r}{\mathscr{R}}\right) - \left(\frac{1}{2}\frac{r^2 - R^2}{\mathscr{R}^2}\right)\right] \qquad (18.82)$$

The vacancy-concentration profile in the grain boundary around the pore depends on the rate of vacancy creation in the grain boundary, G_v. This quantity is not known a priori, and Speight and Harris invoke the arbitrary condition that G_v is just sufficient to render the vacancy concentration midway between voids (i.e., at $r = \mathscr{R}$) equal to the thermodynamic equilibrium value appropriate to the solid under the applied tensile stress (see Chap. 13). Or G_v is determined by applying the auxiliary condition

$$C_v(\mathscr{R}) = C_v^{eq} \exp\left(\frac{\sigma\Omega}{kT}\right) \qquad (18.83)$$

to Eq. 18.82.

Having solved the diffusion problem, we obtain the flux of vacancies to the void by

$$(2\pi Rw)D_{vgb}\left(\frac{dC_v}{dr}\right)_R$$

Assuming that the void remains spherical despite the fact that its vacancy supply is restricted to a belt of width $w \ll R$ at its middle, we find the time rate of change of the volume of the void to be

$$\frac{d}{dt}\left(\frac{4}{3}\pi R^3\right) = (2\pi Rw)D_{vgb}\left(\frac{dC_v}{dr}\right)_R \Omega \qquad (18.84)$$

The gradient at the void surface is obtained using Eq. 18.82, and G_v is eliminated by use of Eq. 18.83. The product $D_{vgb}C_v^{eq}\Omega$ is identified with the grain-boundary self-diffusion coefficient (see Eq. 16.44). Because the arguments of the exponentials in Eqs. 18.80 and 18.83 are small, e^x is approximated by $1 + x$. Equation 18.84 yields

$$\frac{dR}{dt} = \frac{wD_{gb}\Omega}{\mathscr{R}^2 kT}\left(\sigma - \frac{2\gamma}{R}\right)\frac{(\mathscr{R}/R)^2 - 1}{2\ln(\mathscr{R}/R) - 1 + (R/\mathscr{R})^2} \qquad (18.85)$$

This equation shows that the growth rate becomes positive when the void size exceeds the critical value given by Eq. 18.77. Cavities smaller in radius than R_{crit} sinter at a rate given by Eq. 18.85 and eventually disappear. Voids for which $R_0 > R_{crit}$ grow at an ever-increasing rate.

The fraction of the grain-boundary area occupied by voids is

$$f = \left(\frac{R}{\mathscr{R}}\right)^2 \qquad (18.86)$$

Fracture (or creep rupture) is assumed to occur when the voids touch. If the spherical voids are disposed on a regular square array, linkage occurs when the fractional area occupied by the voids is $\pi R_F^2/(2R_F)^2 = \pi/4$, where R_F is the void radius at fracture. Setting $f = \pi/4$ in Eq. 18.86 yields

$$R_F = \left(\frac{\pi}{4}\right)^{1/2}\mathscr{R} \qquad (18.87)$$

The time to rupture is obtained by integration of the growth law from $R = R_0$ to $R = R_F$, or

$$t_R = \int_{R_0}^{R_F}\frac{dR}{(dR/dt)} \qquad (18.88)$$

The elongation (creep strain) at fracture can be estimated as follows. Imagine the solid to be divided into right-square prisms oriented parallel to the applied stress. The height of each prism is the grain size d, and the base of the prism is a square with sides equal to $2R_F$. A void nucleus is located at the center of the top and bottom bases. The volume of solid contained in each prism is $(2R_F)^2 d$. At fracture the top and bottom bases of each prism have been transformed into hemispheres of radius R_F, representing the voids that developed from the nuclei. The centers of the hemispheres at either end of the prism are separated by a distance $d + 2\delta$, where δ is chosen so that the volume of solid in the original and in the final prisms is the same. Thus,

$$(2R_F)^2 d = (2R_F)^2 (d + 2\delta) - \frac{4}{3}\pi R_F^3$$

where the last term on the right represents the volume of the two hemispherical cavities at either end of the prism. The fractional elongation of the grain at fracture is $2\delta/d$, which from the preceding formula is found to be

$$\epsilon_F = \frac{2\delta}{d} = \frac{\pi}{3}\frac{R_F}{d}$$

Substituting Eq. 18.87 for R_F yields

$$\epsilon_F = \frac{\pi^{3/2}}{6}\frac{\mathscr{R}}{d} = \frac{\pi}{6d(N_{gb})^{1/2}} \qquad (18.89)$$

According to this formula, ductility in materials that fail by cavitation is improved by grain refinement and by decreasing the density of void nuclei on grain boundaries.

---

*We assume that the void radius R is much larger than the grain-boundary thickness w. The void surface within the grain boundary is approximated by a cylinder of radius R.

The theory of void nucleation in the grain boundaries (as opposed to the growth theory just presented) is not sufficiently well developed to permit prediction of the void spacing $\mathscr{R}$. However, this quantity can be determined by measuring the void density on grain boundaries from micrographs of the fracture surface and employing Eq. 18.78. Estimates of the time to rupture based on the preceding analysis are in reasonable agreement with the results of creep-rupture tests for many metals. Except for the arbitrariness of the condition of Eq. 18.83, the Hull–Rimmer theory provides a physically acceptable explanation of creep rupture by grain-boundary voids at stresses below that required for wedge-crack propagation. An alternative analysis of the growth process is considered in problem 18.10.

18.10 HELIUM EMBRITTLEMENT

Helium gas produced by transmutation of the components of stainless steel causes embrittlement (loss of ductility), which cannot be eliminated by high-temperature annealing. Like fission gases produced in the fuel, helium is thermodynamically insoluble in metals and tends to precipitate into bubbles if the temperature is high enough for the helium atoms to migrate. If the helium bubbles are formed in the matrix, they can contribute to radiation hardening of the metal in the same manner as voids (i.e., by Eq. 18.53). However, when the temperature is low enough for stable dislocation loops and voids (i.e., $T < 700$ to $800°C$), the increment of strength provided by the helium bubbles is small compared with the contributions of the other radiation-produced defects. At temperatures that result in elimination of voids and dislocations by annealing, the strength of the steel returns to its unirradiated value (see Fig. 18.26). The helium bubbles may have coarsened by coalescence to the point that not enough bubbles are present to cause appreciable hardening.

At elevated temperatures, however, helium causes severe embrittlement of the steel. The elongation to fracture never recovers at high temperatures as does the yield strength. Fracture in the unirradiated metal occurs in a transgranular or combination transgranular–intergranular mode, whereas fracture of irradiated steel occurs invariably along grain boundaries. The extent of helium embrittlement depends on fast-neutron fluence, steel composition, and temperature.

Various mechanisms for explaining helium embrittlement have been suggested. Woodford, Smith, and Moteff[22] proposed that the helium bubbles remain in the matrix where they impede the motion of dislocation lines. The increased strength of the matrix prevents relaxation of stress concentrations at grain-boundary triple points and thereby enhances failure by propagation of wedge cracks. Kramer et al.[23] observed that helium bubbles are nucleated mainly on grain-boundary carbide particles (i.e., $M_{23}C_6$), thereby allowing cracks to form without the necessity of satisfying Stroh's nucleation stress criterion of Eq. 18.66. Reiff[24] has shown that the presence of helium in triple-point cracks permits unstable growth of these cracks at stresses lower than that required for a gas-free crack (Eq. 18.75).

However, the majority of the workers in this field attribute embrittlement to the stress-induced growth of helium bubbles on grain boundaries which eventually link up and cause intergranular failure.[25-27]

18.10.1 Helium Production Rates

Before discussing the embrittlement mechanism in detail, we first determine the amount of helium produced by the neutron flux. The transmutations that produce an alpha particle (which is the nucleus of a helium atom) can be divided into reactions which occur preferentially in a thermal-neutron flux and those which require a fast-neutron flux.

In a thermal flux spectrum, the primary source of helium in steel is due to the reaction

$$B^{10} + n^1 \rightarrow Li^7 + He^4 \qquad (18.90)$$
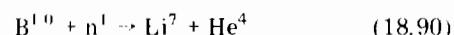
which has an effective cross section in excess of 3000 barns in a Maxwellian (i.e., thermal) flux spectrum. Thus, even the small quantities of boron in stainless steel (Table 18.1) produce substantial quantities of helium. Moreover, the boron in steel is often associated with grain-boundary carbides, which have the generic formula $M_{23}(CB)_6$. Here M denotes iron or chromium, and (CB) means that boron and carbon are interchangeable in the compound. Thus, the helium produced from the boron reaction is strategically available close to grain boundaries, where it can do the most damage.

Natural boron contains only 20% B^{10}, and, in view of the small concentrations of this impurity in most steels, the available B^{10} is burned out of the cladding by reaction 18.90 early in the life of the fuel element. However, the amount of helium found in the cladding continues to increase, partly because of the following two-step reaction involving thermal neutrons and nickel:[28-30]

$$Ni^{58} + n^1 \rightarrow Ni^{59} + \gamma \qquad (18.91a)$$

$$Ni^{59} + n^1 \rightarrow Fe^{56} + He^4 \qquad (18.91b)$$
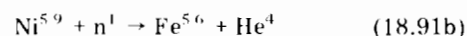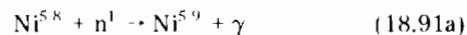
The effective thermal-neutron cross sections for these reactions are 4.4 and 13 barns, respectively. Because the supply of nickel in austenitic stainless steel is inexhaustible (from a nuclear reaction point of view), the helium produced by the two-step reaction of neutrons and nickel continues throughout the life of the fuel element.

In the fast breeder reactors the fast-neutron flux is some four orders of magnitude greater than the thermal-neutron flux. By comparison the fast and thermal components of the neutron flux in the so-called thermal reactors are about equal (see Table 10.1). Thus, although reactions 18.90 and 18.91 produce helium in the cladding of an LMFBR, the fast flux induces (n,α) reactions in all components of the metal. [Fast-neutron irradiation also produces (n,p) reactions on nearly all nuclides. However, the hydrogen produced by these reactions does not cause embrittlement because of rapid diffusion of this element in steel, which leads to escape from the cladding.] Birss[31] has reviewed the reactions that produce helium in reactor materials. The most important helium producers in the steel are the nickel

and iron. The other major constituent of steel (chromium) also produces significant quantities of helium. The impurities nitrogen and boron also release helium as a result of (n,α) reactions induced by fast neutrons. The (n,α) reactions in the metals and the light impurity elements in steel are of the threshold type, which means that the cross section is zero for all energies below a minimum or threshold value. The threshold energy occurs because the reactions are endothermic and hence require the kinetic energy supplied by the neutron to proceed. By contrast, reactions 18.90 and 18.91 are exothermic with cross sections that increase as $E^{-\frac{1}{2}}$. Figure 18.39 shows the energy dependence of the cross sections for a typical (n,α)
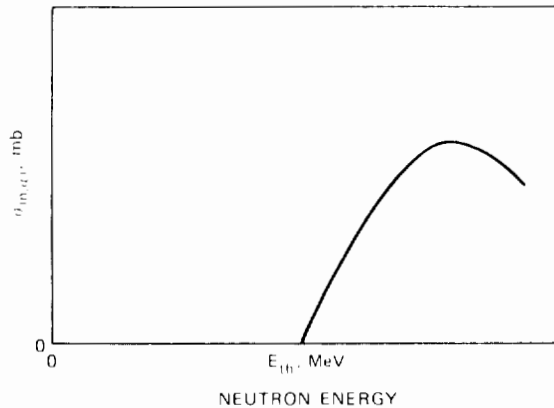

Fig. 18.39 Energy dependence of a typical (n,α) cross section.

reaction. The threshold energy is of the order of 1 to 5 MeV. When multiplied by the energy spectrum of the flux (Fig. 17.18) and by the density of the particular nuclide, the rate of production of helium is given by

$$N \int_{E_{th}}^{\infty} \phi(E)\, \sigma_{(n,\alpha)}(E)\, dE = \text{rate of He production}$$

per unit volume of metal   (18.92)

where N is the density of the nuclide in question and $\phi(E)$ is the flux spectrum. An effective cross section in a particular flux spectrum can be defined by

$$\sigma_{(n,\alpha)eff} = \frac{\int_{E_{th}}^{\infty} \phi(E)\, \sigma_{(n,\alpha)}(E)\, dE}{\int_{0.1}^{\infty} \phi(E)\, dE} \quad (18.93)$$

The denominator of Eq. 18.93 is the total fast-neutron flux (E > 0.1 MeV). The effective (n,α) cross section for the major constituents and two impurities in stainless steel in a fission spectrum are listed in Table 18.3. The cross sections represent the values for each stable isotope of the element in the list weighted with the natural abundance and summed.

Note that the cross sections for the metals are of the order of millibarns, whereas the thermal cross sections of reactions 18.90 and 18.91 are three to four orders of magnitude larger. The nitrogen and boron fast flux (n,α) cross sections are much larger than those of the major constituents of the steel; so these impurity elements are

Table 18.3 Effective (n,α) Cross Sections in a Fission-Neutron Spectrum

Element	$\sigma_{(n,\alpha)eff}$, mb
Cr	0.2
Fe	0.23
Ni	4.2
N	41
B	623

significant contributors of helium in fast reactor fuel-element cladding. The effective (n,α) cross sections in the flux spectrum of a typical LMFBR are about equal to those given for the fission-neutron spectrum in Table 18.3.

Figure 18.40 shows the helium concentrations produced in fast and thermal reactor cladding. The discontinuity in the helium production rate in the thermal reactor is due to burnout of B^{10}. The continued rise in helium concentration is due to threshold (n,α) reactions in the fast component of the neutron flux. The two-step nickel reaction of Eq. 18.91 is not considered in the plot. The helium concentration in the fast reactor cladding becomes larger than that in the thermal reactor after ~100 days. Despite the small cross sections, the fluxes in the fast reactor are larger than in the thermal reactor. After approximately a 2-year irradiation period, the helium concentration in the cladding approaches 100 ppm.

18.10.2 Stress-Induced Growth of Helium Bubbles on Grain Boundaries

The analysis of the rate of growth of helium bubbles lying on grain boundaries perpendicular to the direction of the applied tensile stress is based on the Hull—Rimmer void calculation presented in the previous section. Only two aspects of the void analysis need to be changed: the stability criterion and the vacancy concentration at the bubble surface during growth.

The stability criterion for voids is given by Eq. 18.77. The analogous criterion for gas-filled bubbles in mechanical equilibrium with the solid was deduced by Hyam and
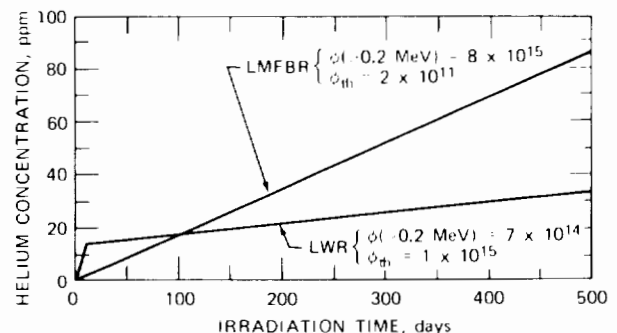

Fig. 18.40 Helium concentration in type 304 stainless steel exposed to LMFBR and LWR flux spectra. [After A. DePino, Jr., Trans. Amer. Nucl. Soc., 9: 386 (1966).]

Sumner.[32] Consider a bubble that contains m helium atoms. In the absence of stress in the surrounding solid, the radius of the bubble is given by Eq. 13.16; we have assumed that the bubble is large enough to permit application of the perfect gas law, a condition which is less restrictive for helium than it is for xenon. Thus,

$$m = \left(\frac{4}{3}\pi R_0^2\right)\left(\frac{2\gamma}{kT}\right) \qquad (18.94)$$

When a tensile stress σ is applied, the new equilibrium radius of the bubble is given by Eq. 13.4:

$$p + \sigma = \frac{2\gamma}{R} \qquad (18.95)$$

and the ideal-gas law:

$$p\left(\frac{4}{3}\pi R^3\right) = mkT \qquad (18.96)$$

Eliminating m and p from Eqs. 18.94 to 18.96 yields the relation

$$\sigma = \frac{2\gamma}{R}\left(1 - \frac{R_0^2}{R^2}\right) \qquad (18.97)$$

Equation 18.97 is plotted in Fig. 18.41 for three values of R_0, which, according to Eq. 18.94, is a measure of the number of helium atoms in the bubble. The function has a maximum when $R = 3^{1/2}R_0$, at which size the stress and the initial radius are related by

$$\sigma = \frac{4}{3(3)^{1/2}}\frac{\gamma}{R_0} = 0.77\frac{\gamma}{R_0} \qquad (18.98)$$

This formula can be interpreted in either of two ways. For a given applied tensile stress, it gives the critical initial bubble radius, $R_{0 crit}$, for stability. If $R_0 < R_{0 crit}$, application of the stress causes the bubble to enlarge to the size that satisfies Eq. 18.97. Alternatively, if the initial bubble radius is specified, the formula gives the critical stress σ_{crit} for stability. If either σ or R_0 is such that the left-hand side
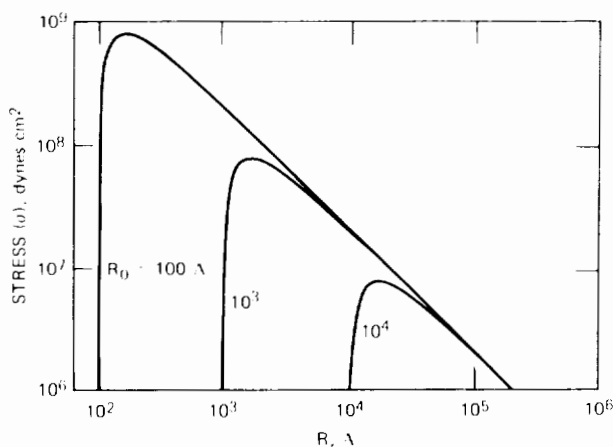

Fig. 18.41 Critical stress for unlimited stress-induced growth of equilibrium bubbles as a function of initial bubble size. (From Ref. 32.)

of Eq. 18.98 is greater than the right-hand side, there is no stable bubble radius, and unlimited growth occurs. Equation 18.98 is the bubble analog of Eq. 18.77 for voids. For a given size of cavity, the critical stress is seen to be a factor of ~3 smaller for equilibrium gas-filled bubbles than it is for voids. This result reflects the fact that the gas pressure, p, in Eq. 18.95 assists the applied stress, σ, in enlarging the bubble.

The growth law for the gas-filled bubble is formulated in a manner similar to that applied by Hull and Rimmer to grain-boundary voids (previous section). The density of grain-boundary bubbles defines the unit cell radius according to Eq. 18.78. If it is assumed that all the helium produced in the matrix is in the form of bubbles and all the bubbles are attached to grain boundaries, an estimate of N_{gb} can be made. Let M be the total concentration of helium in the metal, as determined from Fig. 18.40. If R_0 is the size of the bubbles in the absence of stress, the number of gas atoms per bubble is given by Eq. 18.94. The bubble density (number of bubbles per unit volume) is

$$N = \frac{M}{m} = \frac{M}{(4\pi R_0^2/3)(2\gamma/kT)} \qquad (18.99)$$

If the grain diameter in the specimen is d, there are Nd^3 bubbles per grain. Assuming that the grains are cubical in shape and that the Nd^3 bubbles are uniformly disposed over the six faces of the cube, there are $Nd/6$ bubbles per unit area of grain boundary from one grain. However, each grain boundary is supplied with bubbles from two adjacent grains; so

$$N_{gb} = \frac{Nd}{3} \text{ bubbles/unit grain-boundary area} \qquad (18.100)$$

Unfortunately, Eqs. 18.99 and 18.100 do not uniquely determine N_{gb}. In addition, we must either specify the bubble size, R_0, or the bubble density, N. Knowledge of either of these two quantities depends on the bubble nucleation, migration, and coalescence properties, none of which is well established.

Nevertheless, assuming that the bubble density on the grain boundaries, N_{gb}, can be estimated, the Hull–Rimmer analysis is identical to that presented for voids provided that the boundary condition giving the vacancy concentration at the bubble surface, Eq. 18.80, is modified to account for the effect of the internal gas pressure. To do this, we use Eq. 13.176:

$$C_v(R) = C_v^{eq} \exp\left(\frac{2\gamma}{R} - p\right)\frac{\Omega}{kT} \qquad (18.101)$$

Following the lines of the Hull–Rimmer derivation, the growth law for the helium bubbles is found to be

$$\frac{dR}{dt} = \frac{wD_{gb}\Omega}{\mathcal{R}^2 kT}\left(\sigma - \frac{2\gamma}{R} + p\right)$$
$$\times \frac{(\mathcal{R}/R)^2 - 1}{2\ln(\mathcal{R}/R) - 1 + (R/\mathcal{R})^2} \qquad (18.102)$$

The gas pressure p in this formula is expressed in terms of m and R by Eq. 18.96, and integration according to Eq. 18.88 can be accomplished if m is a constant or a known function of time. Equation 18.102 reduces to the

case for voids (Eq. 18.85) if the cavity contains no gas (i.e., when p = 0).

If the applied stress is less than the critical value given by Eq. 18.98 for the particular initial bubble size R_0, the bubbles enlarge from radius R_0 to a final value that satisfies Eq. 18.97 at a rate given by Eq. 18.102. However, if the applied stress is greater than $0.77\gamma/R_0$, growth proceeds at the rate prescribed by Eq. 18.102 but with no upper limit to R. In this case, growth is terminated when the bubbles touch, which occurs at a radius given by Eq. 18.87. The time to rupture is given by Eq. 18.88, and the elongation at fracture, by Eq. 18.89. Using Eq. 18.100 in Eq. 18.89 gives

$$ \epsilon_F = \left(\frac{\pi^2}{12Nd^3}\right)^{\frac{1}{2}} \qquad (18.103) $$

Equation 18.103 shows that the greater the density of bubbles, the more severe the embrittlement due to helium. Owing to bubble growth by diffusion and coalescence at the expense of nucleation of new bubbles, N increases linearly with neutron fluence and probably decreases with increasing temperature. This phenomenon is commonly called *overaging*.

18.11 SUMMARY OF IRRADIATION EMBRITTLEMENT OF AUSTENITIC STAINLESS STEEL

Mechanical properties are commonly measured in either tensile (high strain rate) or creep-rupture (low strain rate) tests. In these two types of tests, the radiation effects on yield strength, σ_Y, and elongation at fracture, ϵ_F, are most pronounced. As a result of irradiation, σ_Y is increased and ϵ_F is decreased. The radiation-induced loss of ductility is more significant in fuel-element design than is the increase in yield strength; radiation hardening enhances service performance, whereas ductility losses decrease service life. Of these two factors, service life is by far the more important in limiting the design of a reactor fuel element. Embrittlement will probably be the lifetime limiting factor in the first wall of fusion reactors as well.

Embrittlement increases monotonically with neutron fluence in both tensile and creep-rupture tests (Fig. 18.30). The effect of irradiation temperature, however, is quite complex (irradiation temperature should not be confused with testing temperature, the effect of which is shown in Fig. 18.31). Figure 18.42 shows the effect of irradiation temperature on the elongation at fracture in low-temperature postirradiation tensile tests of specimens that have all been irradiated to the same fast-neutron fluence. At low temperatures reduced ductility is due to plastic instability (Secs. 18.3 and 18.9), which in turn is due to the large increase in yield stress without a comparable increase in ultimate strength. As the temperature approaches $500°C$, barriers to dislocation motion (e.g., loops) responsible for hardening begin to be removed, and the metal recovers its work hardenability. As a consequence of this recovery, ductility increases. At approximately the same temperature that point defects in the metal become sufficiently mobile to anneal out the defect clusters that cause hardening, helium atoms in the matrix also become capable of
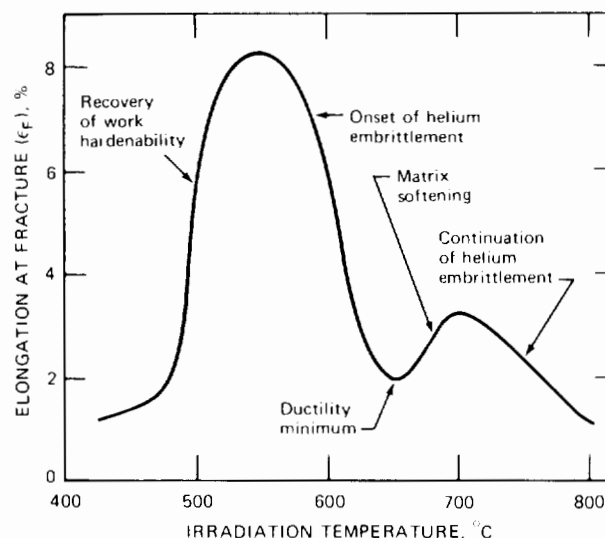

Fig. 18.42 Effect of irradiation temperature on the ductility of irradiated stainless steel. Tensile tests at $50°C$; fast-neutron fluence $>10^{22}$ neutrons cm^{-2} sec^{-1}. [After R. L. Fish and J. J. Holmes, *J. Nucl. Mater.*, 46: (1973).]

migrating and precipitating into bubbles that segregate at the grain boundaries. Consequently, ductility falls because of helium embrittlement. As the temperature reaches $\sim 650°C$, removal of voids becomes appreciable, and the matrix softens some more. The softer matrix permits plastic flow in the neighborhood of wedge cracks and thereby tends to counteract the embrittlement due to helium. The resulting ductility minimum has often been observed in tensile testing of irradiated steels. Eventually, however, helium embrittlement overwhelms all other effects, and the ductility drops to very low values at high temperatures.

Design of fuel elements is usually based on one or more creep-rupture properties of the irradiated metal. For example, if cladding is to operate in a reactor for a specified irradiation time t_{irr}, the allowable stress to which it may be subjected by internal pressure from released fission gases and/or fuel—cladding mechanical interaction can be required to be the smaller of the following two values: (1) 67% of the stress for rupture in time t_{irr} or (2) 100% of the stress to produce 1% total strain (elastic, plastic, and creep) in time t_{irr}.

For irradiated metal the allowable stresses under condition (1) can be obtained from out-of-pile test results such as those shown in Fig. 18.31. The data in Fig. 18.29 permit estimation of the minimum allowable stress under condition (2).

These conditions assume that the stress applied to the cladding is constant over the lifetime t_{irr}. When this is not so, the technique known as the *summation* of *life fractions* is often employed. Neglect for the moment the effect of irradiation, and suppose that the cladding is subject to stress σ_1 for time t_1, σ_2 for time t_2, etc. The sum of the time increments $t_1 + t_2 + \ldots = t_{irr}$. Corresponding to each stress level is a rupture life $t_{R1}, t_{R2}, \ldots$. The allowable combination of times and stresses is given by

$$\frac{t_1}{t_{R1}} + \frac{t_2}{t_{R2}} + \ldots = 1 \qquad (18.104)$$

where it is assumed that the temperature is constant and the stress dependence of the rupture life is known. Equation 18.104 does not include the factor of safety in condition (1).

Similarly, condition (2) is modified in the case of different stresses during cladding lifetime to

$$\frac{t_1}{t_{c1}} + \frac{t_2}{t_{c2}} + \ldots = 1 \qquad (18.105)$$

where t_{ci} is the time required to produce 1% strain at stress σ_i.

In a radiation field, the time to rupture, t_{Ri} in Eq. 18.104, and the time to achieve 1% strain, t_{ci} in Eq. 18.105, depend on the stress σ_i, the temperature T_i, and the accumulated fluence $\sum_{j=1}^{i} \phi_j t_j$ for the interval t_i that the cladding has been in the condition denoted by the subscript i. Thus, stress-rupture failure occurs when[3]

$$\sum_{i=1}^{n} \frac{t_i}{t_R(\sigma_i, T_i, \sum_{j=1}^{i} \phi_j t_j)} = 1 \qquad (18.106)$$

In-pile irradiation creep (Sec. 19.7) is not included in this analysis.

18.12 HARDENING AND EMBRITTLEMENT OF FERRITIC STEELS

The theories of radiation hardening reviewed in Secs. 18.4 through 18.7 apply equally well to bcc and fcc metals and alloys. However, there are several important differences in the ways that these two types of metals respond to radiation, all of which can be traced to the greater mobility of atoms or point defects in the more open bcc lattice compared to the close-packed fcc crystal structure.

18.12.1 Yield Drop

One of the most important differences in the mechanical properties of austenitic and ferritic steels in the unirradiated condition is the absence of a yield drop in the stress–strain behavior of austenitic steel. The existence of a sharp yield point in unirradiated ferritic steels (the upper yield point in Fig. 18.10) is attributed to the pinning of dislocation lines by impurity atoms (principally carbon) strung out along the line. Before a Frank–Read source can be operated by the applied stress, the dislocation line in the source (BC in Fig. 8.13) has to be unpinned from the impurity atoms that have become attached to it as a result of migration from the matrix. The stress field around dislocation lines can attract impurity atoms. Interstitial carbon atoms, for example, are thermodynamically more comfortable in the tensile region below the extra half-plane of atoms of an edge dislocation than they are in the perfect matrix. The stress required to release the dislocation from a row of carbon atoms can be estimated.[1] Once free from the pinning action of the solute atoms, the dislocation can move at a lower stress, which causes the drop in the yield stress from U to L in Fig. 18.10. Yield then propagates at a

nearly constant flow stress until the beginning of normal work-hardening processes arising from interaction between moving and stationary dislocations.

The carbon-dislocation locking mechanism is not important in austenitic steels because the diffusion coefficient of carbon in the close-packed fcc lattice is lower than it is in the more open bcc structure of ferritic steel. Under normal quenching procedures, the carbon atoms in austenitic steel cannot move rapidly enough to the dislocation line to provide a concentration of atoms along the line which is sufficient to strongly lock the dislocation. As indicated in Sec. 18.5, fcc metals develop a yield drop under irradiation because point defects can take the place of impurity atoms in locking dislocations.

18.12.2 Radiation Anneal Hardening

The high mobility of impurity atoms in bcc metals is manifest by the phenomenon of *radiation anneal hardening*, which is not observed in fcc materials. If, following a low-temperature irradiation, specimens of an fcc metal are annealed for several hours before testing, the radiation-produced increase in the yield stress decreases uniformly with annealing temperature. With bcc metals, on the other hand, the yield stress first increases with annealing temperature, then passes through a maximum before returning to the value observed for the unirradiated metal. The increased hardening arising from the annealing process is due to the migration of interstitial impurity atoms (oxygen, nitrogen, and carbon) to radiation-produced defect clusters, such as the depleted zones or dislocation loops.[14] Impurity–defect cluster complexes form more effective obstacles to dislocation motion than do impurities and defect clusters when they exist separately in the matrix. The high interstitial-atom diffusivities permit migration of the small impurity atoms to the defect clusters at temperatures lower than those at which the clusters are destroyed by annealing. However, at sufficiently high temperatures, both the complexes and the defect clusters are removed, and hardening diminishes with temperature as in fcc metals.

18.12.3 Creep Strength

The high diffusion rate of the intrinsic components of the bcc metals (the vacancies and matrix atoms) in the more open bcc structure is responsible for the poorer creep-rupture strength of the ferritic steels compared with austenitic steels. Creep by growth of grain-boundary cavities, for example, occurs by vacancy diffusion (Sec. 18.9), which is greater in bcc metals than in fcc metals. For this reason, austenitic steels are used in high-temperature core components rather than ferritic alloys.

18.12.4 High-Temperature Embrittlement

One of the most striking differences between bcc and fcc metals is the absence of helium embrittlement in bcc metals. That is, bcc metals and alloys are not subject to the drastic loss in ductility when irradiated at high temperature. One would expect that the higher diffusion coefficients in the bcc materials would accelerate creep rupture by the growth of intergranular voids that are stabilized by helium,

which is believed to be the principal mechanism of helium embrittlement in fcc metals. The virtual absence of helium embrittlement in bcc metals indicates that creep failure in these materials does not occur by the stress-enhanced cavity growth mechanism. Rather, it is believed that the large self-diffusion coefficients in bcc metals permit efficient reduction of stress concentrations at grain boundaries, thereby reducing the tendency for triple-point or wedge cracking.[35] The high point-defect mobility assists in the processes of recrystallization (growth of new grains) and recovery (softening of the matrix due to annealing of the dislocation network). Both processes act to reduce stress concentrations and thereby inhibit intergranular failure.

18.12.5 Brittle Fracture—The Cottrell—Petch Theory

On the basis of an earlier theory of Petch, Cottrell[36] has proposed a theory of yielding in metals exhibiting a distinct yield point which can be applied to determine the fracture stress. Knowledge of both the yield and fracture stresses permits the conditions for brittle fracture to be deduced.

The lower yield point in bcc metals or in irradiated fcc metals contains contributions due to source hardening and friction hardening (Sec. 18.5). Friction hardening is the stress experienced by dislocations moving through the metal. Source hardening represents the applied stress needed to unlock pinned dislocations and set them into motion. Cottrell assumes that dislocations in a few isolated grains have been unlocked either because the orientation of these grains relative to the load is such as to produce the maximum resolved shear stress on active slip planes or because a few sources in these grains have particularly low unpinning stresses. In either case, the dislocations produced in the prematurely yielded grains pile up against the grain boundary. The enhanced shear stress in the neighborhood of the pileup triggers the sources in the adjacent grain. Like a row of dominoes, yielding propagates across the entire specimen, or the material flows.

The shear stress exerted on the slip plane in a grain next to one that has yielded and released an avalanche of dislocations which are stopped by the grain boundary is shown in Fig. 18.43. The shear stress acting on the sources in grain 2 consists of two components, the applied shear stress σ_{xy} and the shear stress due to the proximity of the pileup in grain 1. The latter is given by Eq. 8.41 wherein σ_{xy} is reduced by σ_i to account for the frictional stress experienced by dislocations in the pileup in grain 1. Thus, the sources in grain 2 are subject to the shear stress

$$\sigma_2 = \sigma_{xy} + (\sigma_{xy} - \sigma_i)\left(\frac{d}{L'}\right)^{\frac{1}{2}} \qquad (18.107)$$

where d (the grain size) is taken to be the length of the pileup in grain 1 and L' is the distance from the grain boundary to the nearest dislocation source in grain 2. The ratio d/L' is generally much greater than unity. The stress required to operate the sources in the material is denoted by σ_d. In high-purity unirradiated metals, σ_d is the stress needed to activate Frank—Read sources (Eq. 8.16), but, in ordinary bcc metals or in irradiated fcc metals, $\sigma_d > \sigma_{FR}$
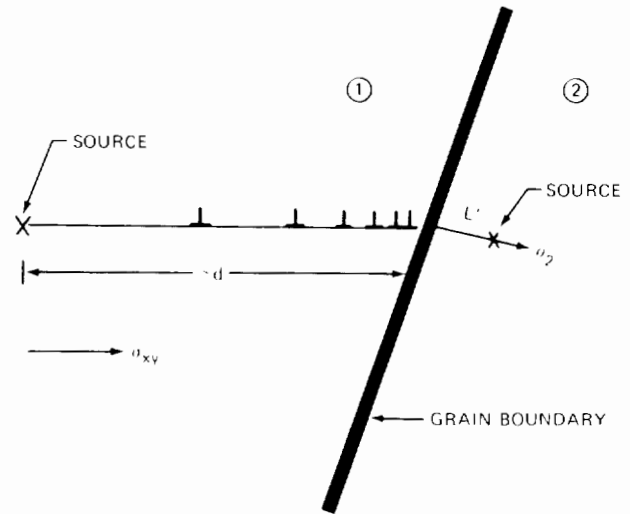

Fig. 18.43 Shear stress on source in unyielded grain due to pileup in adjacent yielded grain.

because of locking of the source dislocations by impurities or point defects produced by radiation.

At the instant yielding is triggered by the mechanism of Fig. 18.43, σ_{xy} is equal to the yield stress σ_Y and σ_2 is equal to σ_d. Making these substitutions in Eq. 18.107 gives

$$\sigma_d = \sigma_Y + (\sigma_Y - \sigma_i)\left(\frac{d}{L'}\right)^{\frac{1}{2}}$$

or, solving for the yield stress,

$$\sigma_Y = \frac{\sigma_i + \sigma_d(L'/d)^{\frac{1}{2}}}{1 + (L'/d)^{\frac{1}{2}}} \simeq \sigma_i + \sigma_d\left(\frac{L'}{d}\right)^{\frac{1}{2}} \qquad (18.108)$$

If the product $\sigma_d(L')^{\frac{1}{2}}$ is denoted by a constant k_y, the yield stress becomes

$$\sigma_Y = \sigma_i + k_y d^{-\frac{1}{2}} \qquad (18.109)$$

The second term on the right gives the source-hardening contribution to the yield stress. The two components of σ_Y can be determined experimentally by one of two means:

1. By extrapolating the work-hardening portion of the stress—strain curve in Fig. 18.10 to the elastic line. The intercept is interpreted as σ_i, and the difference between the lower yield point and the intercept is the source-hardening contribution $k_y d^{-\frac{1}{2}}$. This procedure has been employed by Makin and Minter[4] to determine the effect of neutron irradiation on the friction and source-hardening components of copper.

2. By measuring the yield stress for specimens of different grain size and plotting σ_Y vs. $d^{-\frac{1}{2}}$. The intercept of such a plot is σ_i, and the slope gives k_y.[35] Most metals obey a plot of this sort quite well.

With k_y determined from yield-stress measurements, Cottrell calculates the critical tensile stress for fracture by substituting Eq. 18.109 into Eq. 18.75. At the yield stress, σ_{xy} is identified with σ_Y, and the term in the parentheses of Eq. 18.75 is given by $k_y d^{-\frac{1}{2}}$. Thus, the fracture stress is

$$\sigma_{crit} = \sigma_F = \frac{2G\gamma}{k_y} d^{-\frac{1}{2}} \qquad (18.110)$$

The effect of grain size on the fracture stress (or ultimate tensile stress) and the yield stress of a low-carbon steel is shown in Fig. 18.44. The two lines cross at the ductile—brittle transition. To the right of this point, the material is ductile, since it yields before fracturing. The incremental ~~strain~~ $\sigma_F - \sigma_Y$ needed to cause fracture is supplied by work-hardening processes, which means that the metal must deform plastically. As shown by the lower curve in this figure, appreciable elongation occurs before fracture. To the left of the transition, yielding and fracture occur simultaneously. Fracture takes place along the yield stress line since yielding is a prerequisite to fracture. In this region the metal is totally brittle.

The Cottrell—Petch theory can be employed to explain the effect of radiation on the yield and ultimate tensile strengths of steels. The frictional component to the yield stress, σ_i, is quite sensitive to radiation owing to the defect clusters produced by fast-neutron bombardment (Sec. 18.5). The parameter k_y, on the other hand, depends on the stress to operate dislocation sources in the metal, σ_d. In fcc metals and alloys, this stress is slightly increased by radiation because the point defects assist in pinning the sources. In bcc metals, however, the sources are strongly pinned by impurity atoms in the absence of neutron-produced point defects; so radiation has a negligible effect on k_y for metals of this crystallographic structure. Conse-

quently, the theory suggests that the yield stress should increase more than the ultimate stress as a result of irradiation. This prediction is borne out by experiments. The drastic loss in ductility at low temperature results from the different sensitivities of σ_Y and σ_F to neutron damage.

Figure 18.45 shows the Cottrell—Petch theory displayed on a temperature plot for different values of the frictional stress. The increase in σ_i is assumed to be due to neutron irradiation. The ductile—brittle transition temperature (DBTT) or the nil-ductility temperature (NDT) is defined by the condition that $\sigma_F = \sigma_Y$, or from Eq. 18.110 by the formula:

$$\sigma_Y k_y = 2G\gamma d^{-\frac{1}{2}} \qquad (18.111)$$

Although this equation could in principle be solved for the transition temperature (using the temperature dependencies of σ_Y and k_y), it is most commonly employed to estimate the effect of neutron exposure on the temperature at which ferritic steels become brittle. The graphic illustration of the increase in the transition temperature shown in Fig. 18.45 can be expressed quantitatively by using Eq. 18.111 and noting that the right-hand side is essentially constant during irradiation and temperature variation. Thus,

$$d(\sigma_Y k_y) = \sigma_Y dk_y + k_y d\sigma_Y = 0$$

The changes in k_y and σ_Y due to the variables T and neutron fluence (neutron fluence is manifest by radiation hardening or an increase in the frictional stress σ_i) are

$$dk_y = \left(\frac{\partial k_y}{\partial T}\right) dT + \left(\frac{\partial k_y}{\partial \sigma_i}\right) d\sigma_i$$

$$d\sigma_Y = \left(\frac{\partial \sigma_Y}{\partial T}\right) dT + \left(\frac{\partial \sigma_Y}{\partial \sigma_i}\right) d\sigma_i$$

Combining these expressions and neglecting the effect of radiation on source hardening (i.e., $\partial k_y/\partial \sigma_i = 0$ and hence,
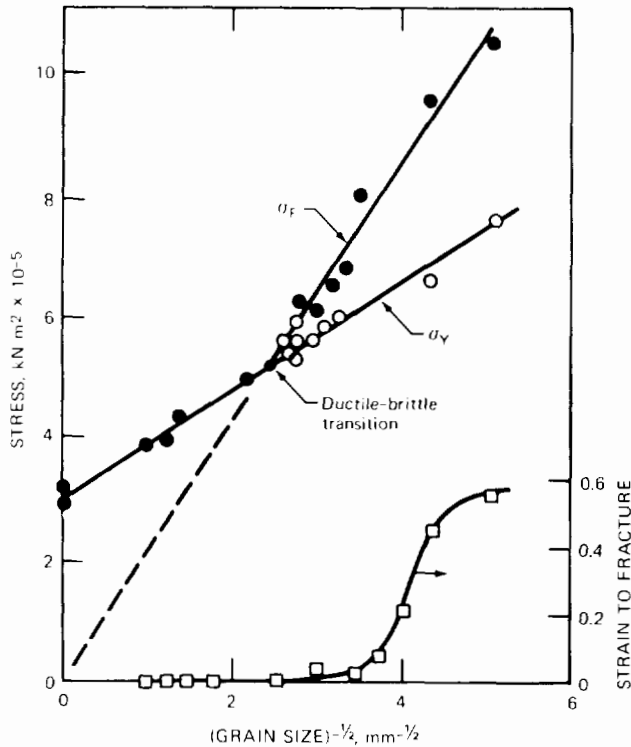

Fig. 18.44 Effect of grain size on yield and fracture stresses of a low-carbon steel tested at low temperature. ●, fracture. ○, yield. □, strain. (After Ref. 36.)
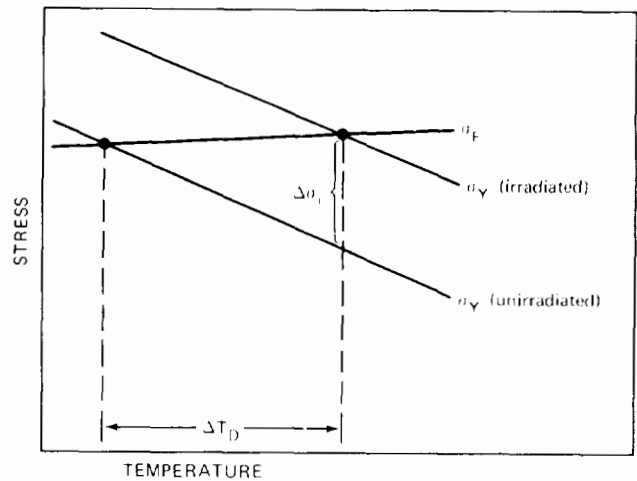

Fig. 18.45 Effect of temperature on the yield and fracture stresses of unirradiated and irradiated ferritic steel.

according to Eq. 18.109, $\partial\sigma_Y/\partial\sigma_i = 1$), we obtain the increase in the transition temperature:

$$\frac{dT}{d\sigma_i} = \frac{\Delta T_D}{\Delta\sigma_i} = -\left(\frac{\sigma_Y}{k_y}\frac{\partial k_y}{\partial T} + \frac{\partial\sigma_Y}{\partial T}\right)^{-1} \qquad (18.112)$$

The temperature dependence of k_y is slight, but, since it is multiplied by a large number in Eq. 18.112, it is retained in the analysis. The yield stress, the source-hardening coefficient, and their temperature derivatives can be obtained from out-of-pile tests. Inserting numerical values shows that

$$\frac{\Delta T_D}{\Delta\sigma_i} = 3 \text{ to } 5°C \text{ per } 10^4 \text{ kN/m}^2 \qquad (18.113)$$

for typical pressure-vessel steels. As discussed in Sec. 18.3, the DBTT or NDT can be measured by impact tests. Figure 18.13(b) shows that the DBTT of unirradiated low-carbon steel is about $0°C$. The corresponding curve for an irradiated specimen is translated to much higher temperatures than the data for unirradiated material shown in this graph. When the radiation hardening ($\Delta\sigma_i$) is measured as well, observed values of ΔT_D are in good agreement with the predictions of the Cottrell–Petch theory, expressed by Eq. 18.113.

The increase in the frictional stress $\Delta\sigma_i$ is due almost exclusively to the production of obstacles in the slip planes of moving dislocations. At the low temperatures at which pressure vessels in LWRs operate, $\Delta\sigma_i$ can be identified with the hardening due to depleted zones (Eqs. 18.38 and 18.42). Figure 18.46 summarizes data on the increase in the
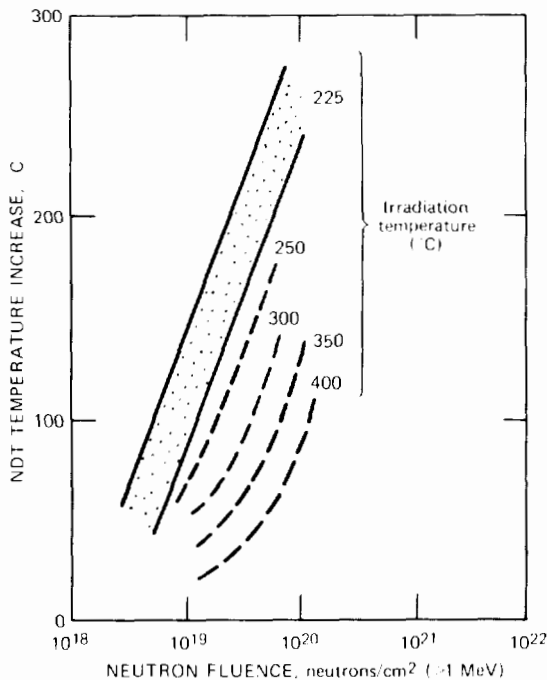

NEUTRON FLUENCE, neutrons/cm² (>1 MeV)

Fig. 18.46 Effect of fast neutron fluence on the increase in the nil-ductility temperature of low carbon steels irradiated at various temperatures. (After L. E. Steele and J. R. Hawthorne, in ASTM Special Technical Publication 380, p. 283, American Society for Testing and Materials, Philadelphia, 1965.)

nil-ductility temperature of various pressure-vessel steels with neutron fluence. If the component operates at temperatures below ~250°C for long irradiation periods, a considerable increase in the NDT is observed. As shown by the graph, the NDT can approach the operating temperature of the pressure vessel (approximately equal to the inlet coolant temperature in a PWR) after long periods of irradiation. Periodic annealing of ferritic steel components of the reactor core may be necessary to eliminate accumulated radiation damage. As part of a surveillance program, coupons of the metal can be inserted in the core and periodically withdrawn for impact testing.

Additional information on the effects of neutron exposure on ferritic steels can be found in Refs. 6, 37, and 38.

18.13 NOMENCLATURE

a_0 = lattice constant
A = cross-sectional area of a tensile test specimen; mass number
b = Burgers vector
C = point-defect concentration (particles per unit volume); crack length
d = grain size
D = point-defect diffusion coefficient; tube diameter
D_{gb} = grain-boundary self-diffusion coefficient
D_{vgb} = diffusivity of vacancies in grain boundary
DBTT = ductile-to-brittle transition temperature
E = neutron energy; activation energy for steady-state creep; Young's modulus
E_{el} = elastic-energy density
E_{th} = threshold energy for (n,α) reaction
f = fraction of grain-boundary area occupied by voids
f_x,f_y = angular functions of the force between edge dislocations in the x and y directions, respectively
F = force on a unit length of dislocation
G = shear modulus
G_v = vacancy production rate in a grain boundary
k = Boltzmann's constant
k_{iv} = vacancy–interstitial recombination rate constant
k_y = constant in the Cottrell–Petch theory, Eq. 18.109
l = gauge length of tensile test specimen; spacing of obstacles in a glide plane, Eq. 18.25
l_0 = length of dislocation segment between pinning points
L = length of dislocation pileup
L' = distance from grain boundary to nearest dislocation source
m = helium atoms per bubble
n = number of dislocations in a pileup
N = concentration of obstacles, depleted zones, loops, or bubbles
N_{gb} = number of voids or helium bubbles per unit grain-boundary area
p = gas pressure
P = load on tensile test specimen
r = radius of obstacle to dislocation motion

r_d = radius of dislocation core

R = radius of depleted zone, dislocation loop, or helium bubble

$\mathscr{R}$ = radius of unit cell surrounding a void or bubble on a grain boundary; radius of curvature of a dislocation line; radius of the stress field around a dislocation

t = time; wall thickness

t_R = rupture time

T = temperature

T_c = characteristic temperature, Eq. 18.39

T_D = ductile-to-brittle transition temperature

T_m = melting point, °K

U^* = activation energy for dislocation cutting of an obstacle

U_0 = energy increase when dislocation cuts an obstacle

v = capture volume around a depleted zone

v_d = velocity of a glide dislocation

V_c = crack volume

w = thickness of grain boundary

W = work

x = distance along glide plane

y = distance perpendicular to glide plane

Z = capture sites around a dislocation

Greek Letters

α = number of defect clusters per neutron collision

β = numerical constant, Eq. 18.62

γ = surface energy (including plastic deformation)

γ_{gb} = grain-boundary tension

γ_s = surface tension of solid (used when plastic deformation at crack tip is important)

Γ = probability per unit time that a dislocation cuts an obstacle

ϵ = strain

ϵ_F = strain at rupture

$\epsilon_1, \epsilon_2, \epsilon_3$ = principal strains

ϵ^* = equivalent strain (strain deviator), Eq. 18.17

$\dot{\epsilon}$ = strain rate

ν = Poisson's ratio; vibration frequency of dislocation against an obstacle; number of displacements per primary knock-on atom

ρ = density of mobile dislocations

ρ_d = total density of dislocations in a solid

σ = stress (positive in tension)

σ^* = equivalent stress (stress deviator), Eq. 18.15

σ_i = friction stress

$\sigma_{(n,\alpha)}$ = cross section for n,α reaction

σ_{xy} = shear stress

τ = time

$\phi(E)$ = neutron flux spectrum

Φ = total fast-neutron flux

Ω = atomic volume

Σ_s = macroscopic neutron-scattering cross section

Subscripts and Superscripts

crit = critical value

e = edge dislocation

eq = equilibrium

F = at fracture

h = hydrostatic

i = interstitial

l = dislocation loop

LR = long range

max = maximum

R = at the surface of a defect

s = short range

v = vacancy

Y = at yield point

18.14 REFERENCES

1. D. Hull, *Introduction to Dislocations*, Sec. 10.1, Pergamon Press, Inc., New York, 1965.
2. J. Friedel, *Dislocations*, p. 220, Pergamon Press, Inc., New York, 1964.
3. A. Seeger, in *Proceedings of the Second United Nations International Conference on the Peaceful Uses of Atomic Energy*, Geneva, 1958, Vol. 6, p. 250, United Nations, New York, 1958.
4. M. J. Makin and F. J. Minter, *Acta Met.*, 8: 691 (1960).
5. M. J. Makin and T. H. Blewitt, *Acta Met.*, 10: 241 (1962).
6. F. A. Nichols, *Phil. Mag.*, 14: 335 (1966).
7. C. C. Dollins, *Radiat. Eff.*, 11: 33 (1971).
8. P. Coulomb, *Acta Met.*, 7: 556 (1959).
9. R. W. Weeks et al., *Acta Met.*, 17: 1403 (1969).
10. M. J. Makin, *Phil. Mag.*, 10: 695 (1964); see also F. Kroupa, *Phil. Mag.*, 7: 783 (1962).
11. F. Kroupa and P. B. Hirsch, *Discuss. Faraday Soc.*, 38: 49 (1964).
12. A. J. E. Foreman, *Phil. Mag.*, 17: 353 (1968).
13. F. R. Smidt, Jr., Dislocation Channeling in Irradiated Metals, Report NRL-7078, Naval Research Laboratory, 1970.
14. A. N. Stroh, *Proc. Roy. Soc. (London), Ser. A*, 223: 404 (1954).
15. D. McLean, *J. Inst. Metals*, 85: 468 (1956-57).
16. C. W. Weaver, *Acta Met.*, 8: 343 (1960).
17. E. E. Bloom and J. R. Weir, Jr., in *Irradiation Effects in Structural Alloys for Thermal and Fast Reactors*, Symposium Proceedings, San Francisco, Calif., p. 261, American Society for Testing and Materials, Philadelphia, Pa., 1969.
18. J. A. Williams, *Acta Met.*, 15: 1559 (1967).
19. F. Garzarolli et al., *J. Nucl. Mater.*, 30: 242 (1969).
20. D. Hull and D. E. Rimmer, *Phil. Mag.*, 4: 673 (1959).
21. M. V. Speight and J. E. Harris, *Metal Sci. J*, 1: 83 (1967).
22. D. A. Woodford, J. P. Smith, and J. Moteff, *J. Nucl. Mater.*, 29: 103 (1969).
23. D. Kramer, H. R. Brager, C. G. Rhodes, and A. G. Pard, *J. Nucl. Mater.*, 25: 121 (1968).
24. K. H. Reiff, *J. Nucl. Mater.*, 33: 129 (1969).
25. R. S. Barnes, *Nature*, 206: 1307 (1965).
26. D. R. Harries, *J. Brit. Nucl. Energy Soc.*, 5: 74 (1966).
27. G. J. C. Carpenter and R. B. Nicholson, in *Radiation Damage in Reactor Materials-1969*, Symposium Proceedings, Vienna, June 2-6, 1969, Vol. 2, p. 383, International Atomic Energy Agency, Vienna, 1969 (STI/PUB/230).
28. J. Weitman et al., *Trans. Amer. Nucl. Soc.*, 13: 557 (1970).
29. I. R. Birss and W. E. Ellis, in *Voids Formed by Irradiation of Reactor Materials Conference*, p. 339, British Nuclear Energy Society, London, 1971.

30. A. A. Bauer and M. Kangalaski, *J. Nucl. Mater.*, 42: 91 (1972).

31. I. R. Birss, *J. Nucl. Mater.*, 34: 241 (1971).

32. E. D. Hyam and G. Sumner, in *Radiation Damage in Solids*, Symposium Proceedings, Venice, May 1962, Vol. 1, p. 323, International Atomic Energy Agency, Vienna, 1962 (STI/PUB/56).

33. A. J. Lovell and J. J. Holmes, *Trans. Amer. Nucl. Soc.*, 15: 735 (1972).

34. S. M. Ohr et al., in *Second International Conference on Strength of Metals and Alloys*, Vol. 2, Paper 9.3, p. 742, American Society for Metals, Metals Park, Ohio, 1970.

35. H. Bohm and H. Hauck, *J. Nucl. Mater.*, 29: 184 (1969).

36. A. H. Cottrell, *Trans. AIME*, 212: 192 (1958).

37. L. P. Trudeau, *Radiation Effects on Toughness of Ferritic Steels for Reactor Vessels*, American Society for Metals—U. S. Atomic Energy Commission Monograph, Rowman and Littlefield, Inc., New York, 1964.

38. N. Igata and R. R. Hasiguti, *J. Nucl. Mater.*, 30: 234 (1969).

18.15 PROBLEMS

18.1 As a result of irradiation, a specimen of metal contains voids. The specimen is annealed out of pile at temperature T. Voids grow or shrink only by vacancy capture or emission. The bulk solid contains the thermal-equilibrium vacancy concentration.

(a) How does the radius of a void with initial radius R_0 change with annealing time?

(b) If the void sizes after irradiation are distributed according to the function $N_0(R_0) \, dR_0$ = number of voids with radii between R_0 and $R_0 + dR_0$, what is the void distribution function at a time t in the anneal? Assume the vacancy-diffusion coefficient D_v, the equilibrium vacancy concentration C_v^{eq}, the surface tension of the metal γ, and the atomic volume Ω are specified. Use a calculational method like the one applied to thermal annealing of depleted zones (Sec. 18.5).

(c) Suppose the initial distribution $N(R_0)$ is Gaussian with an average void radius of 400 Å and a standard deviation of 50 Å. The initial void concentration, N_T^0, is 10^{15} cm^{-3}. During annealing, the voids of average size disappear in 3 hr. Compute and plot the void distributions at t = 0 and t = 2 hr.

18.2 The work-hardening region of the stress—strain curve can be represented by the formula $\sigma = k\epsilon^n$, where n is the work-hardening coefficient. By increasing the yield stress more than the ultimate tensile stress, irradiation effectively reduces the work-hardening coefficient. Using the criterion for plastic instability, calculate the reduction in uniform elongation due to an irradiation that decreases n by an amount Δn.

18.3 (a) Show that Eq. 18.26 is valid for a regular planar array of dislocation pinning points [e.g., the (100) plane of the fcc structure].

(b) The potential energy of a dislocation cutting through an obstacle in Seeger's treatment of radiation hardening is of the form

$$Y = 1 - \frac{1}{1 + e^\eta} - A\eta + \text{constant}$$

where

$$Y = \frac{U(x,\sigma_s)}{U_0}, \quad \eta = \frac{x}{r'}, \quad A = \frac{\sigma b l_0 r'}{U_0}$$

Demonstrate the following properties of the function $Y(\eta)$:

1. The barrier height disappears if $A = \frac{1}{4}$.

2. Expand the location of the maximum and minimum in a Taylor's series in the parameter $\epsilon = 1 - 4A$, which is presumed to be small and positive. Show that the extrema are given by

$$\eta_\pm = \pm 2\epsilon^{\frac{1}{2}}$$

3. Show that the barrier height is given by

$$Y(\eta_+) - Y(\eta_-) = 2\epsilon^{\frac{1}{2}}$$

18.4 The data for depleted-zone hardening by nickel (Fig. 18.20) suggest that two types of zones are created by irradiation. From the curves on this figure, compute the ratio of the radii and of the numbers of the zones represented by lines A and B.

18.5 Consider a dislocation line in a solid containing N bubbles of radius R per cubic centimeter. A shear stress σ_{xy} is applied to the solid which causes the dislocation to glide along its slip plane.

(a) Under what conditions will the bubbles be swept along by the dislocation line rather than be bypassed by it?

(b) Under conditions permitting bubble sweeping, what is the initial velocity of the dislocation line? Assume that the bubbles move by the surface-diffusion mechanism.

(c) As the dislocation line moves, it collects all the bubbles in its path, which reduces the bubble spacing along the line and slows it down. Neglecting coalescence of the bubbles attached to the dislocation line, find the velocity of the dislocation line after it has moved a distance x in the direction of the applied shear stress.

18.6 Consider a thin-walled cylinder of radius R and thickness t_c which is subject to internal pressure p but zero external pressure. The top and bottom of the cylinder are closed; so there is an axial stress on the cylinder wall.

(a) Use simple force balances to determine the axial stress σ_ℓ and the hoop stress σ_θ.

Use linear elasticity theory (see the Appendix) and the assumption of plane strain (i.e., ϵ_ℓ independent of r and z, but not necessarily zero) to determine the following:

(b) The differential equations and boundary conditions for the radial stress, σ_r. Without the thin wall assumption, obtain the solutions for σ_r and σ_θ as functions of radial position. Show that σ_θ reduces to the result obtained in (a) for the special case of a thin wall.

(c) The strain components ϵ_z, ϵ_r, and ϵ_θ.

(d) The differential equation (and its general solution) for the radial displacement, u_r.

(e) Show that the radial strain, ϵ_r, is related to the fractional decrease in wall thickness:

$$\epsilon_r = \frac{\Delta t_c}{t_c}$$

18.7 An irradiated metal contains a network-dislocation density of ρ_d and N_l dislocation loops per unit volume of radius R_l. The yield stress of the irradiated specimen is measured at temperatures just below and just above the temperature at which the loops unfault. What is the difference in the yield stress between these two measurements? Assume that the unfaulted loops become part of the dislocation network of the solid.

18.8 Derive the expression for the force between a straight edge dislocation line and a dislocation loop whose plane is perpendicular to the slip plane of the edge dislocation and parallel to the edge dislocation itself. Prepare a plot similar to Fig. 18.24 for this case when the distance between the slip plane of the straight edge dislocation and the center of the loop is three loop radii.

18.9 Equation 18.75 gives the critical tensile stress for stability of gas-free wedge-shaped cracks on grain-boundary triple points. Suppose, however, that the cracks form from pores on the triple points which are initially of volume V_0 and contain m helium atoms. Under the influence of an applied stress σ, the pores grow to wedge cracks of length C and width nb.

(a) The grains in the metal are modeled as tetrakaidecahedrons of size 1 (see sketch). At a particular time during irradiation, M atoms of helium have been produced per unit volume of metal. Assume that all the helium has been collected in the triple-point cracks. What is m, the number of helium atoms per crack?

TETRAKAIDECAHEDRON
36 edges (length = l)
24 corners
14 faces

Volume = $8(2)^{1/2} l^3$
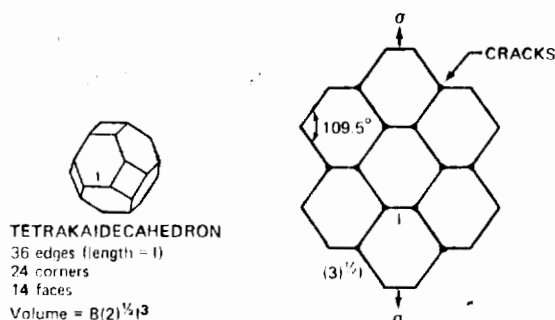
(b) What is the energy required to form the crack? The effective stress is the sum of the internal gas pressure and the tensile stress σ. In forming the crack, the contained gas does work.

(c) What is the critical stress for unstable growth of those cracks favorably oriented with respect to the applied stress? Assume low gas pressure to simplify your result.

This problem has been analyzed by K. Reiff, *J. Nucl. Mater.*, 33: 129 (1969).

18.10 The stress-induced growth of grain-boundary voids is to be analyzed by a grain-boundary vacancy-diffusion model similar to the one applied by Coble to grain-boundary diffusional creep (Sec. 16.6). Steady-state vacancy diffusion takes place in the annular region $R \leqslant r \leqslant \mathcal{R}$ of thickness w illustrated in Fig. 18.38. The present analysis is two-dimensional, with z measured from the midplane of the grain-boundary slab. Since the system is symmetric about the midplane, only the region $0 \leqslant z \leqslant w/2$ need be

considered. The radial boundary conditions on C_v are given by Eqs. 18.80 and 18.81. One of the two required z boundary conditions reflects symmetry about $z = 0$, $(\partial C_v/\partial z)_{z=0} = 0$ for all r. Following Coble's treatment, the boundary condition at the interface between the matrix and the grain-boundary zone is $C_v(r,w/2) = C_v^{eq} \exp(\sigma\Omega/kT)$; that is, the applied stress affects the equilibrium vacancy concentration only at the boundary of the diffusion zone, not, as in Speight and Harris' treatment, within this zone.

(a) Write the diffusion equation and the boundary conditions in terms of the dimensionless vacancy concentration:

$$\theta = \frac{C_v(r,z) - C_v(R,z)}{C_v(r,w/2) - C_v(R,z)}$$

(b) Obtain a solution for $\theta(r,z)$ by the method of separation of variables.

(c) What is the total rate of vacancy diffusion to the void and the growth law dR/dt?

18.11 In the Hull—Rimmer analysis that produced the grain-boundary growth law given by Eq. 18.85, the vacancy concentration midway between voids is assumed to be equal to the thermodynamic equilibrium value under the applied tensile stress. However, the stress in this analysis is determined by dividing the applied load to the specimen by the cross-sectional area. When voids form on grain boundaries perpendicular to the load direction, the load-bearing area on the grain boundaries is reduced by the presence of the voids. How should the growth law be modified to take this effect into account?

18.12 Calculate the helium content (in atomic ppm) in type 304 stainless steel (Table 18.1) irradiated for 1 year in a flux with a thermal component of 10^{13} neutrons cm^{-2} sec^{-1} and a fast component of 10^{15} neutrons cm^{-2} sec^{-1}.

18.13 Consider helium bubbles 1000 Å in radius located on a grain boundary. To what size do the bubbles grow under the influence of a tensile stress one-half the critical value for instability?

Two of the bubbles coalesce. What is the equilibrium size of the new bubble?

18.14 Equation 18.98 gives the critical stress for spherical helium bubbles on a grain boundary. However, the equilibrium shape of bubbles on grain boundaries is lenticular rather than spherical (see sketch).
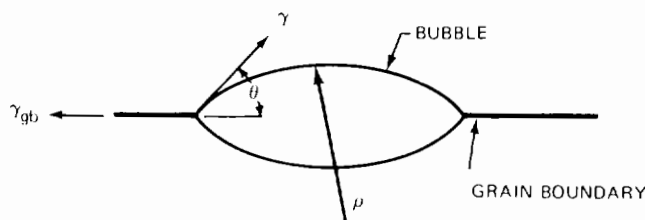
(a) If the grain-boundary tension is γ_{gb} and the surface tension of the metal is γ, what is the equilibrium geometry

(i.e., the relation between the angle θ and the radius of curvature ρ) of a lenticular bubble containing m gas atoms when the solid is unstressed?

(b) How does the result of (a) change when the solid is subjected to a hydrostatic tensile stress σ?

(c) What is the critical stress for unstable growth of the lenticular bubble? Express the answer as the ratio of the critical stress for a lenticular bubble to that for a spherical bubble containing the same number of helium atoms. If $\gamma_{gb}/\gamma = 0.4$, what is this ratio?

18.15 A specimen of irradiated austenitic stainless steel under an applied stress of 2×10^5 kN/m² fails owing to helium embrittlement at a strain of 1%. What concentration (in atomic ppm) of helium in the metal is necessary to cause fracture at this value of the strain? The grain size in the metal is $15 \, \mu m$ and the surface tension is 1500 dynes/cm. The irradiation temperature is $1000°C$.

18.16 Helium is produced in an irradiated metal at a rate of G atoms cm⁻³ sec⁻¹. All this helium is trapped in bubbles on grain boundaries as soon as it is formed. There are N_{gb} bubble sites per unit grain-boundary area, and the grain size is d.

. (a) What is the rate of helium-atom capture at each bubble site?

(b) What is the time t_c at which the growing grain-boundary bubbles become unstable with respect to an applied tensile stress σ? What is the bubble radius R_c at this time? For $t \leqslant t_c$, bubble growth rate is determined by the helium influx (i.e., the bubble is always at equilibrium).

(c) For $t > t_c$, the bubble is unstable, and its rate of expansion is controlled (and limited) by the rate at which vacancies reach it. Gas atoms are assumed to reach the bubble at the rate determined in (a). Accounting for the continued increase in the number of gas atoms in the bubble during the unstable growth period, set up the equations needed to determine the rupture time t_R.

(d) What is the elongation at rupture ϵ_F?

18.17 The life-fraction approach is to be applied to estimate the most probable service lifetime of a fuel element subject to creep rupture. Steady-state creep is assumed at all times; so the rupture life for fixed conditions is given by $t_R = \epsilon_F/\dot{\epsilon}$. Neglect irradiation creep and assume that the creep rate is not affected by fluence but depends on stress and temperature according to Eq. 8.46. Assume that the fracture strain decreases with fluence as shown in Fig. 18.30. The fission-gas pressure within the cladding increases linearly with irradiation time at a known rate. Derive the expression from which the service life could be estimated if all the constants involved were specified. The temperature is constant throughout irradiation.